Hard X-Ray polarimetry with position sensitive germanium detectors - studies of the recombination transitions into highly charged ions

Dissertation
zur Erlangung des Doktorgrades
der Naturwissenschaften

vorgelegt beim Fachbereich Physik
der Johann Wolfgang Goethe-Universität
in Frankfurt am Main

von
Stanislav Tashenov
aus Vologda

Frankfurt am Main 2005
(DF1)

vom Fachbereich Physik der Johann Wolfgang Goethe-Universität
als Dissertation angenommen.

Dekan:	Prof. Dr. W. Aßmus
Gutachter:	Prof. Dr. Th. Stöhlker
	Prof. Dr. H. Schmidt-Böcking
Datum der Disputation:	

Contents

1 Introduction **5**

2 Interaction of X-Rays with matter **9**

2.1 Photoelectric Effect 9

2.2 Compton Scattering 11

2.2.1 Thomson limit 12

2.2.2 Klein-Nishina formula 13

2.2.3 Rayleigh scattering (coherent elastic scattering) 14

2.3 Pair production 16

2.4 Photon attenuation 17

2.5 Electron stopping power 17

3 Hard X-ray polarimetry - an overview **19**

3.1 Basic polarimeter constructions 19

3.1.1 Introduction to Compton polarimetry 19

3.1.2 Detector material considerations and the "Kinematic event selection" 22

3.1.3 Polarimeter quality considerations 26

3.2 Multiple integral (segmented) detectors 29

3.2.1 Planar stripe and pixel detectors 30

3.3 Other polarimeter types 34

3.3.1 Measuring the polarization of high energy photons 35

3.3.2 Measuring the circular polarization 35

4 Theoretical description of RR and REC **37**
4.1 The Stobbe formula for K-shell REC 39
4.2 Born approximation for K-shell REC and the angular distribution 39
4.3 Angular distributions from the exact calculation 41
4.4 Photon Polarization 42
4.4.1 Theoretical Results for Photon Polarization 44

5 Status of the experimental studies of REC in comparison with the theory **49**
5.1 Total cross sections 49
5.2 Relative angular-differential cross sections 52

6 The Experimental Environment **55**
6.1 The Experimental Storage Ring ESR 55
6.2 Experiments at the internal jet-target of the ESR 59
6.3 REC studies at the Internal Target 61
6.3.1 REC line shape analysis 63

7 The measurement of the K-REC polarization **65**

8 Data analysis: Compton polarimetry in application to the pixel detector **71**
8.1 X-ray spectra 71
8.2 Compton scattering 73
8.2.1 Pixel to pixel coincidences 73
8.2.2 Compton scattering kinematics 74
8.3 Scattering intensity distribution 79
8.3.1 Pixel efficiencies 82
8.3.2 Internally normalized intensity distribution 82
8.4 Monte-Carlo simulation/fitting program 84
8.5 Model description and errors estimation 85
8.5.1 Multiple scattering 85
8.5.2 Multiple Compton scattering inside one pixel 86

8.5.3 Relativistic scattering on bound electrons and Compton profile 89
8.5.4 Rayleigh scattering (coherent elastic scattering) 92
8.5.5 Uncertainty in the detector depletion depth 92
8.5.6 Summary for the systematic effects 94

9 Results and discussion **97**

10 Outlook **105**
10.1 REC polarization studies 105
10.2 The 2D stripe detector 107

11 Summary **109**

12 Zusammenfassung **111**

Chapter 1

Introduction

Energetic ion-atom collisions of highly-charged heavy ions with neutral gases have been extensively studied during last years, both experimentally and theoretically. These studies became possible due to the experimental advances within the last decade in heavy-ion accelerator and storage ring techniques [1, 2, 3, 4, 5]. Heavy ion studies have been proved to be a unique tool in a large number of fields in modern physics, in particular *nuclear and particle physics, plasma physics* and *astrophysics* [6]. In *atomic physics* such investigations opened new perspectives with respect to studies of simple atomic systems (i.e. H- or He-like uranium) in extreme conditions, i.e. the strong electromagnetic field of nuclei and relativistic collision energies. Such conditions lead to remarkable effects both for the electronic *structure* of the few electron ions and for their collision *dynamics*. A strong electric field of heavy nuclei leads to strongly pronounced quantum electrodynamical (QED) effects [7, 8, 9], significant changes in the level structure due to strong spin-orbital interactions [10] and enhanced decay rates.

Besides structure studies for heavy ions, the *dynamics* of the *relativistic* ion-atom and ion-electron collisions has attracted a particular interest. The dominating processes in such collisions are the Radiative Electron Capture (REC) or Radiative Recombination (RR). They represent one of the most fundamental atomic processes along with the photoionization process which is a time reversal of RR [11, 12, 13, 14]. Therefore the studying of the RR and REC is equivalent to the investigation of the photoionization for highly-charged heavy ions in the relativistic regime. For photoionization such techniques are still not established

experimentally.

The RR and REC processes have been studied during last years in great details, including total and state selective cross sections, angular distributions and alignment studies. It was shown that relativistic effects play an important role in the REC process, for instance an unambiguous signature of the spin-flip effect, mediated by magnetic interactions, was obtained in angular differential cross section measurements [15, 16]. A detailed look into dynamics of the REC process is also provided by *alignment* studies, i.e. studies of the magnetic subshell population produced by the REC into a bound state of an ion, for example the $2p_{3/2}$ state. A strong alignment has been observed for $U \rightarrow N_2$ collisions for energies above 200 MeV/u [17].

Theoretical studies of the REC have been confirmed by a large amount of the recent experimental observations. Recently a topic of the polarization of REC photons has attracted a particular interest. It was theoretically predicted that the radiation following the REC into highly charged ions should be strongly polarized [18, 19, 20]. Nevertheless up to now no experimental investigations were carried out for this subject, although the predicted effects have high magnitudes and should be measurable with a high precision. Moreover, very recent investigations show that the study of the REC polarization can give an access to spin polarization of an ion beam [21]. This can lead to a possible application of this technique as a nondestructive tool for the diagnostics of spin polarized ion beams. Note that up to now all existing methods of the ion beam diagnostics require an extraction of the beam out of a storage ring.

Another important aspect of the REC polarization studies is that in its time reversal it gives an access to high energy photoionization polarization effects like the *cross over* effect, theoretically predicted already in 1931 [22, 23].

Efficient studies of X-ray polarization became possible nowadays due to the progress in the development of position and energy sensitive solid state detectors. During last years such detectors find more and more applications in atomic physics research [24]. Two-dimensionally segmented Ge detectors can be used as Compton polarimeters. The Compton technique in X-ray polarimetry is known since 50^s [25] and it was widely used in nuclear science for many decades. Nevertheless it was not applied in atomic physics due to the low energy limit for this

method at $\approx$ 60 KeV, which was much to high for usual atomic spectroscopy purposes. Nowadays atomic physics with highly charged ions requires to perform a spectroscopy in hard X-ray regime, up to several hundreds of KeV. The high purity Ge detectors have significantly improved energy resolution and timing. Segmented Ge detectors, used as polarimeters can provide an increased sensitivity to the hard X-ray polarization and an efficiency by orders of magnitude higher than the conventional polarimeter schemes used in 70's in nuclear physics.

In spite of larger difficulties in handling of such detectors and higher complexity of the data analysis, the future of atomic physics research depends in an important extend on this kind of detectors. Besides polarimetry purposes these detectors due to the fine segmentation and position sensitivity found an application in precision spectroscopy in combination with crystal spectrometers [26]. The use of a DSP (Digital Signal Processing) based readout system can increase position sensitivity of a 2D stripe detector by a factor of $2 \div 4$ and provide a 3D position sensitivity which will allow to use such a detector as a *Compton Camera* (*Compton Telescope*).

This work concentrates on two major tasks. First: an application of the prototype 4x4 Pixel Detector as a hard X-ray polarimeter, describing the method of the Compton polarimetry and it's concrete realization using a position sensitive Ge detector. Second: first experimental study of the polarization of K-REC photons at the GSI ESR storage ring, an experiment was conducted for bare uranium ions.

The thesis is structured in the following way. The chapter 2 contains a description of the main processes of the photon-matter interaction for the hard X-Ray regime, required to understand the physics of solid state detectors and their realization as polarimeters. The chapter 3 contains an introduction into the subject of the Compton polarimetry including the basic concept, major formulas, all different schemes of the polarimeters and the aspects of an optimization. The chapter 4 is the theoretical introduction in the RR and REC processes, the current understanding of the physics of the relativistic ion-atom collisions. In the chapter 5 we compare major experimental findings in REC with the theoretical results. The chapter 6 describes the employed experimental techniques in the RR and REC studies. The chapter 7 describes the first experiment on

the REC polarization, proof of the method and an unambiguous signature of the strong polarization of the REC radiation. In the chapter 8 details of the data analysis are discussed. First one describes the developed method of the Compton polarimetry in application with the Pixel Detector, then discusses the error bars and systematic effects. The chapter 9 shows the obtained results in comparison with the theory. In the chapter 10 an outlook for these investigations is given and in the chapter 11 the performed work is summarized.

Chapter 2

Interaction of X-Rays with matter

In the following the major photon-matter interaction processes, required for a basic understanding of the physics of photon detectors and their application for photon polarimetry, are discussed.

The basic interaction of hard X-Rays with matter consists mainly out of following processes:

1. Photoelectric Effect
2. Compton Scattering (including Thompson scattering)
3. Coherent (Rayleigh) scattering
4. Pair Production

Figure 2.1 shows the cross sections for the above listed interactions for the case of germanium atoms.

2.1 Photoelectric Effect

Photoelectric effect results in a total absorption of a photon $\hbar\omega$ and an emission of a bound electron. The energy of the emitted electron is then:

$$E = \hbar\omega - E_{bind} \tag{2.1}$$

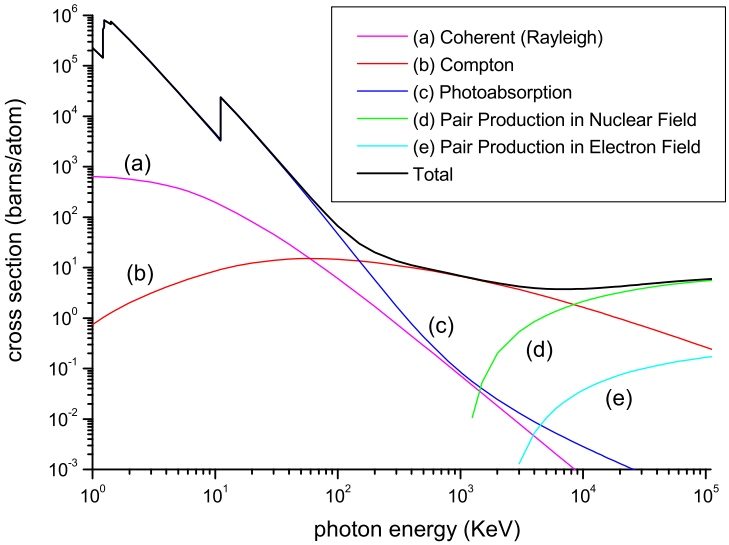

Figure 2.1: Cross sections for the main interaction processes of hard X-Rays with matter for germanium atoms [27, 28, 29, 30].

where E_{bind} is the binding energy of the electron in the initial state. The probability of the photoelectric effect per atom can be described by the following relationship:

$$\sigma \sim Z^n/(\hbar\omega)^{\frac{7}{2}} \tag{2.2}$$

where Z is the atomic number and n is a varying exponent between 4 and 5 across $\hbar\omega$. Photoelectric effect is predominant for low energies and increases with increasing atomic number. This factor is important to consider when choosing a material for a X-ray detector. For germanium it dominates up to energies of $\approx 100\ KeV$, see figure 2.1 for comparison. The Equation 2.2 is valid for photon energies which are not close to the electron binding energies. The cross section rapidly increases while the photon energy is approaching the K-shell binding energy. Just after that point, the cross section drops drastically since K-electrons are no longer available because of energy conservation 2.1. This point is usually called *K-Shell absorption edge*. The same behavior occurs near $L-$, $M-$ and the other absorption edges.

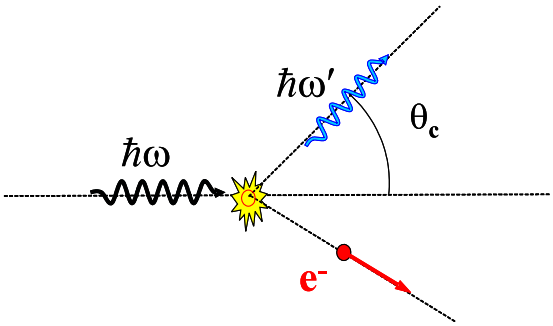

Figure 2.2: Kinematics of Compton scattering: $\hbar\omega$ denotes the initial photon, $\hbar\omega'$ the Compton scattered photon and e^- the Compton recoil electron, respectively. Θ_c is the Compton scattering angle.

2.2 Compton Scattering

Compton effect is a scattering of photons on free or quasi-free electrons, see figure 2.2. The kinematics of the Compton process is described by an equation below which reflects the energy and the momentum conservation:

$$\hbar\omega^{'} = \frac{\hbar\omega}{1 + \frac{\hbar\omega}{m_e c^2}(1 - \cos\theta)} \ . \tag{2.3}$$

Here θ is the Compton scattering angle and $\hbar\omega$ and $\hbar\omega^{'}$ are the energies of the incident and the scattered photons, respectively.

From the Equation 2.3 and the requirement of energy conservation $\hbar\omega = \Delta E + \hbar\omega^{'}$, one can deduce the recoil energy of the electron ΔE:

$$\Delta E = \hbar\omega \frac{\frac{\hbar\omega}{mc^2}(1 - \cos\theta)}{1 + \frac{\hbar\omega}{mc^2}(1 - \cos\theta)} \ . \tag{2.4}$$

These general relations of the Compton kinematics are shown in figure 2.3 for two different energies of the incoming photons, 100 KeV and 300 KeV. One can see that for relatively low photon energies ($\hbar\omega < mc^2/2$) the scattered photon energy is always larger than the energy of the scattered electron. But for incident photon energies above $mc^2/2$ this is no longer true and the photon energy is larger only at forward angles.

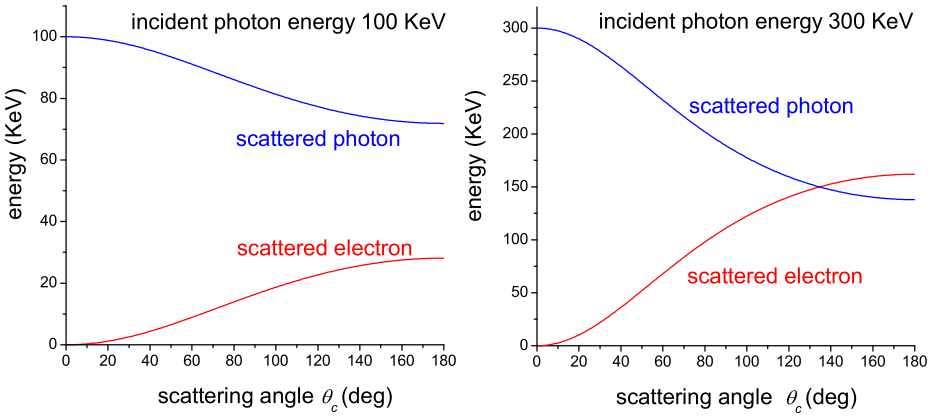

Figure 2.3: Kinematical relations in Compton scattering. Dependance of the scattered photon and electron energies on the scattering angle θ for different energies of the incident photon.

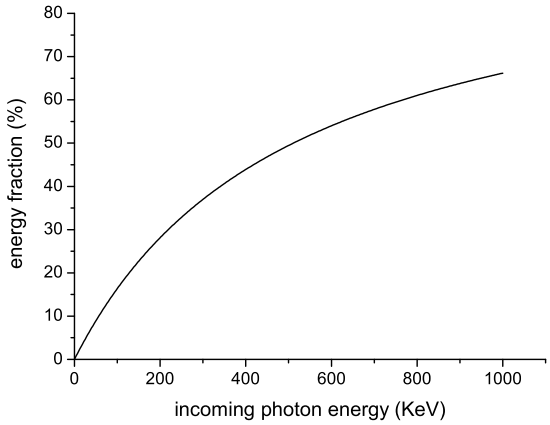

Figure 2.4: Mean energy transfer to the recoil electron in % of the incident photon energy.

2.2.1 Thomson limit

With decreasing energy of the incident photon, the energy transferred to the recoil electron also decreases. Already at an incident photon energy of 1 KeV, only up to 0.4% of the energy can be transferred to the recoil electron, see figure 2.4 for comparison. The classical limit when no energy is transferred to the electron is called *Thomson scattering*.

The classical Thomson scattering cross section is equal to:

$$\sigma = \frac{8\pi}{3} r_e^2 = 6.6524 \times 10^{-25}\ cm^2 \tag{2.5}$$

where $r_e = \frac{e^2}{m_e c^2} = 2.8 \times 10^{-13}\ cm$ is the classical electron radius (it is the radius of a spherical shell of total charge whose electrostatic energy equals the rest mass energy of the electron). Note that the cross section of the Thomson scattering is independent of the frequency (this result is strictly true only in the limit $\hbar\omega << mc^2$).

The differential cross section for this process is given by:

$$\frac{d\sigma}{d\Omega} = r_e^2 (\varepsilon \cdot \varepsilon')^2 \tag{2.6}$$

where ε and ε' are the incident and scattered radiation electric polarization vectors. This expression can be derived from Larmor's formula for the radiation of an accelerated charge [31].

2.2.2 Klein-Nishina formula

The cross section for Compton scattering was first calculated by Klein and Nishina using the theory of quantum electrodynamics. Nowadays in standard text books [31, 32, 33, 34, 35] one can find the following equation for the differential cross section of the photons Compton-scattered into solid angle element $d\Omega$:

$$\frac{d\sigma}{d\Omega} = \frac{r_0^2}{2} \frac{\hbar\omega'^2}{\hbar\omega^2} \left(\frac{\hbar\omega'}{\hbar\omega} + \frac{\hbar\omega}{\hbar\omega'} - 2\sin^2\theta \cos^2\varphi \right) \tag{2.7}$$

where φ is the azimuthal scattering angle, the angle between the plane of Compton scattering and the polarization plane, see figure 2.5 for comparison.

The sensitivity to the polarization is a feature of the Compton process which is explored in Compton polarimetry. An angular φ-distribution for a vertically aligned photon polarization $\vec{E}$ is displayed in figure 2.6. Measuring this distribution is a method to study the polarization of the photon beam.

Another important characteristic of the Compton process which is of particular relevance for solid-state detector discussions is the energy distribution of the

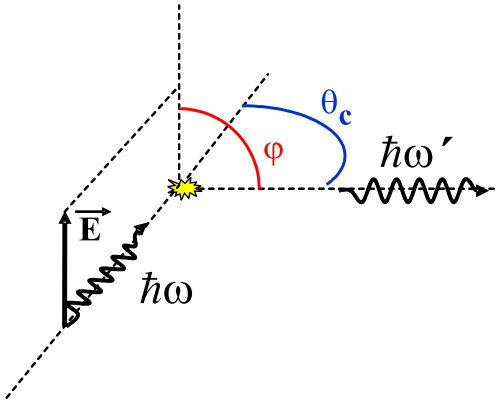

Figure 2.5: Geometry of the Compton scattering process. The angle φ is an angle between the propagation direction of the scattered photon and the polarization vector of the incoming photon.

Compton-recoil electrons, see figure 2.7. This introduces a background to the measured X-ray spectrum. The maximum electron energy allowed by kinematics is:

$$\Delta E = \hbar\omega \frac{2\frac{\hbar\omega}{mc^2}}{1+2\frac{\hbar\omega}{mc^2}} \ . \tag{2.8}$$

Finally one may note that the Compton process plays a significant role among photon interaction processes with matter in the energy range of $\approx$ 100 KeV $\div$ 10 MeV, see figure 2.1 for comparison.

2.2.3 Rayleigh scattering (coherent elastic scattering)

Rayleigh scattering is essentially Thomson scattering on electrons bound in an atomic potential, including the effects of resonances and phase coherence between multiple electrons [36]. For the case when the energy of the photon is much higher than the binding energy of the electrons, is:

$$\frac{d\sigma}{d\Omega} = Z^2 r_e^2 (\varepsilon \cdot \varepsilon')^2 \tag{2.9}$$

which is the same as Thomson scattering cross section but augmented by Z^2, where Z is the total number of electrons in the atom. The cross section is

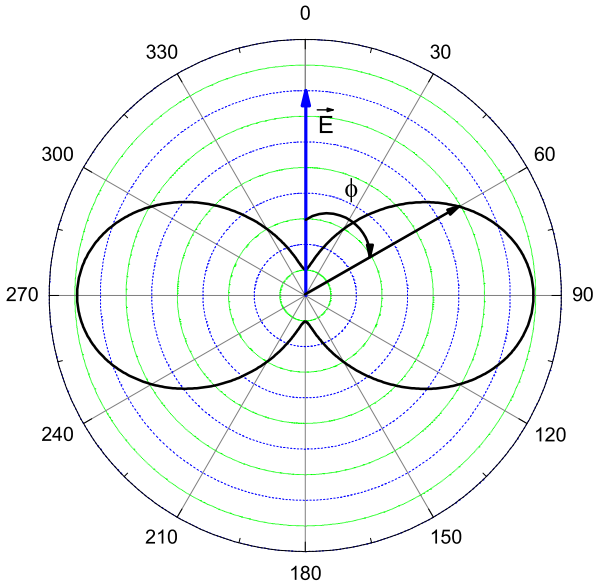

Figure 2.6: The differential cross section for the Compton scattering. Here the ϕ-distribution for a vertically aligned photon polarization $\vec{E}$ is displayed (see figure 2.5).

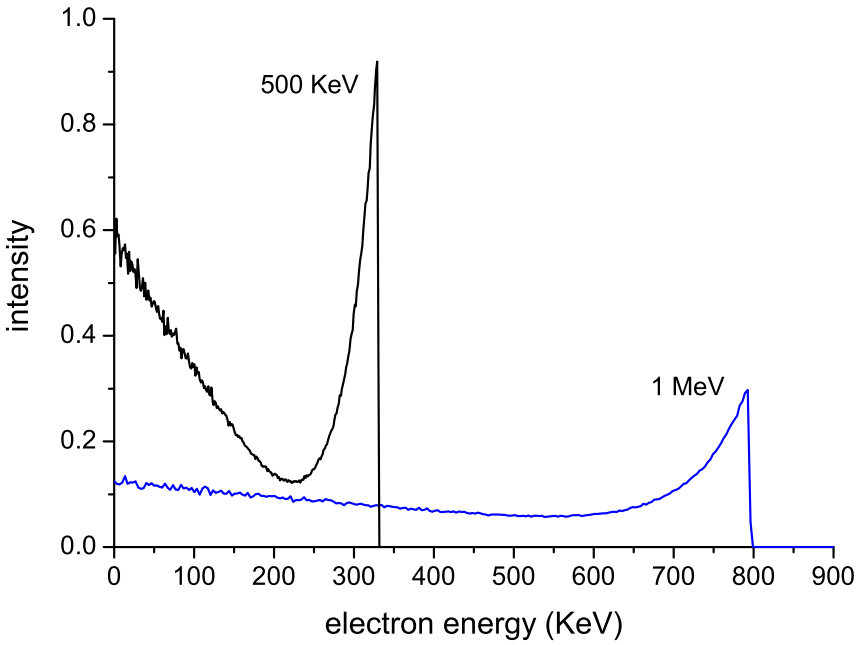

Figure 2.7: Energy distribution of the recoil electrons, produced in Compton scattering of photons with the initial energy of 500 KeV and 1 MeV respectively.

proportional to the square of the electron number because of the scattering phases correlation (coherence).

The Equation 2.9 is valid only for the low energy limit <2 KeV. For higher energies Rayleigh scattering becomes strongly forwarded with a corresponding cross section [28]:

$$\sigma_{\mathrm{coh,Rayleigh}} = \pi r_{\mathrm{e}}^2 \int_{-1}^{1} (1 + \cos^2\theta) f^2(\theta) \mathrm{d}(\cos\theta) \tag{2.10}$$

where $f(\theta)$ is an atomic scattering *form factor* which for higher energies falls off rapidly with the scattering angle, see figure 2.8.

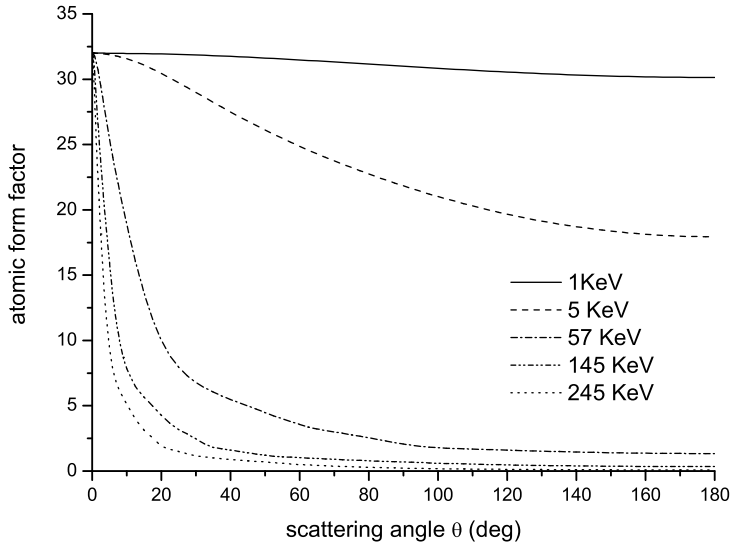

Figure 2.8: Atomic form factor $f(\theta)$ in Rayleigh scattering for germanium given for different photon energies [36].

2.3 Pair production

For completeness one should also mention the Pair production effect, although the properties of it are not explored in the present work.

For the photon energies larger than $2m_e c^2 = 1.022$ MeV a transformation of the photon into an electron-positron pair can occur. A third body is required to

conserve the momentum. Pair creation in presence of nuclei or electrons is shown separately on figure 2.1.

2.4 Photon attenuation

A peculiarity of the photon interaction with matter is that the beam of photons does not degrade in energy as it passes through the matter, but is only attenuated in intensity. It is due to the fact, that the listed above processes remove a photon from the beam entirely, either by absorption or scattering. The intensity attenuation is exponential along the propagation distance [37]:

$$I(x) = I_0 \cdot exp(-\sigma_{total}\rho x) \tag{2.11}$$

where I_0 is initial intensity of the beam, σ_{total} is a total cross section of the photon interaction with matter for a given energy, which is a sum of the cross sections of all processes, ρ is the particle density of the matter $\frac{N}{cm^3}$ and x is a thickness of the absorber.

$$\sigma_{total} \;=\; \sigma_{photoelectric} \;+\; Z\sigma_{compton} \;+\; \sigma_{pair\ production} \tag{2.12}$$

Here the factor Z at the Compton cross section is introduced due to the fact that each atom has Z electrons. The total absorption coefficient is the inverse mean path of the photon in the matter.

$$\begin{aligned} &I(x) = I_0 \cdot exp(-\mu x)\ , \\ &where \qquad \mu = \sigma_{total}\rho\ . \end{aligned} \tag{2.13}$$

2.5 Electron stopping power

The electrons produced by photoionization, Compton scattering or pair production are stopped in the matter. Electrons loose energy due to Coulomb collisions that result in the ionization and excitation of atoms and due to emission of bremsstrahlung quanta. Collision process dominates the energy loss process

for electron energies up to 10 MeV. Figure 2.9 show an average path length of electrons in germanium crystal.

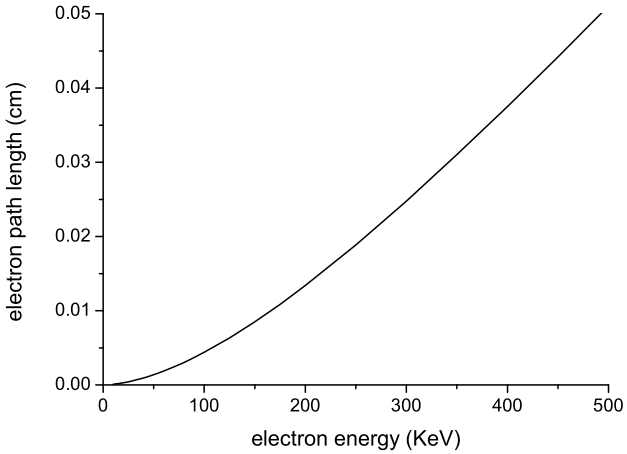

Figure 2.9: Mean path length of electrons in a germanium crystal as function of the electron energy.

Chapter 3

Hard X-ray polarimetry - an overview

For soft X-rays in the energy region from $\sim$ 1 KeV to several tens of KeV, few types of polarimeters employing Bragg reflection, photo-absorption and Thomson scattering have been developed [38, 39, 40, 41, 42]. For the high energy range (GeV), polarimeters employing an electron-positron pair production are used [43]. In order to investigate the polarization for the energy range from $\approx$ 60 KeV up to several MeV, a Compton scattering effect, which is known to be sensitive to linear photon polarization, is usually employed. Compton scattering polarimetry is known since 50^s [25]. There, in order to investigate the polarization of hard X-rays, a target for Compton scattering together with an X-ray detector was used.

3.1 Basic polarimeter constructions

3.1.1 Introduction to Compton polarimetry

Various polarimeter types exist, representing different combinations of detector materials, coincidence efficiencies, sensitivities, energy resolution, and technical constructions [44]. The conventional method uses two or more X-ray detectors, one as a scatterer and the other one as an absorber(s), see figure 3.1. The latter detects the scattered photon typically at the angles of $\varphi = 0^0$ and $\varphi = 90^0$ with

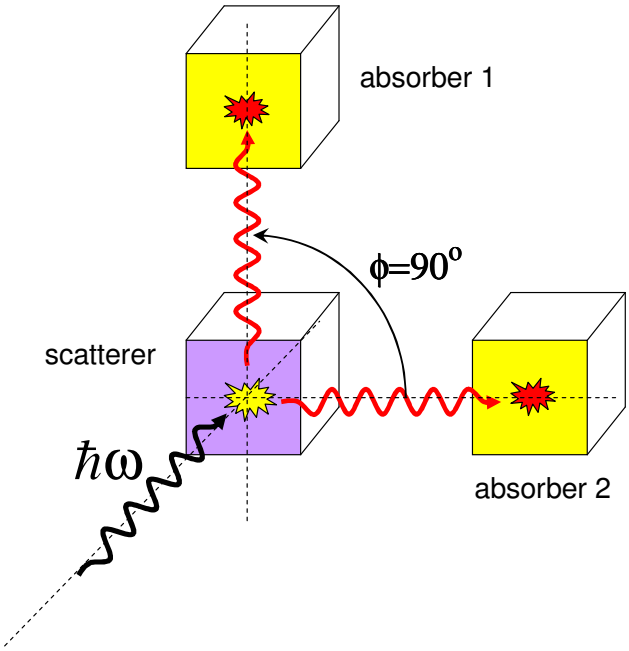

Figure 3.1: Basic scheme of a Compton scattering polarimetry experiment. One detector serves as a scatterer and one or more as absorbers. The angular distribution of the scattered photons delivers the information about the incident photon polarization.

respect to the plane defined by the incident photon propagational direction and its polarization orientation. The degree of the linear polarization can be extracted from measuring the angular distribution of the scattered photons.

The sensitivity of Compton scattering to linear polarization is described by the Klein-Nishina formula 2.7, i.e. a differential cross section for photons Compton scattered into an element of solid angle $d\Omega$, see figure 2.5.

The scattering of linear polarized radiation results in an azimuthal modulation of the counts, see figure 2.6. The *modulation fraction* is defined by [44]:

$$M(\varphi) = \frac{N(\varphi + 90^0) - N(\varphi)}{N(\varphi + 90^0) + N(\varphi)} = \frac{\sigma_\perp - \sigma_{\shortparallel}}{\sigma_\perp + \sigma_{\shortparallel}} \; . \tag{3.1}$$

Usually the later is used to find the maximum scatter direction. For comparison with the scattering cross sections the modulation fraction is expressed in normalized units. M reaches its maximum when φ is in the direction of the initial polarization vector, and its minimum appears perpendicular to it.

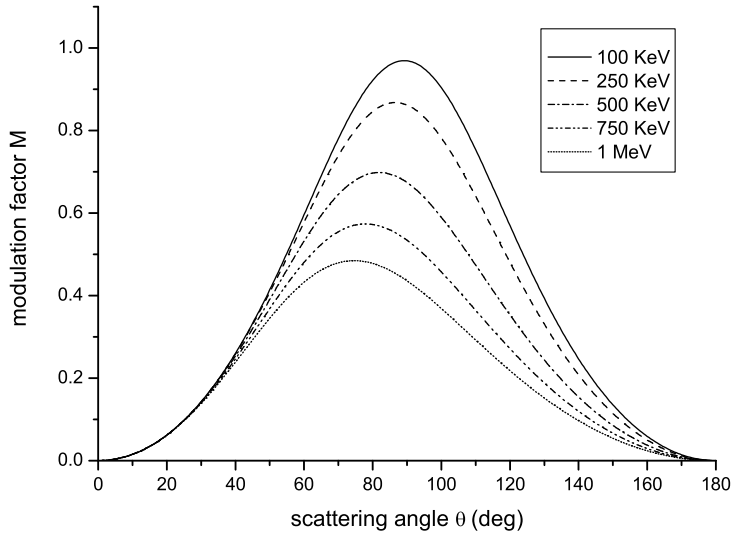

Figure 3.2: Energy and scattering angle θ dependance of the modulation factor M for various photon energies (see Eq. 3.1).

The modulation fraction as a function of Compton scattering angle θ is shown in figure 3.2. Lower energies have a higher modulation fraction. The maximum modulation fraction is above 90% for energies below 200 KeV, and occurs for events where the Compton photon scatters by $\approx 90^0$. With increasing energy the peak of the curve moves slightly to smaller forward angles which might be a useful fact in designing detectors that are optimized for energies above ≈ 1 MeV. The modulation fraction diminishes to zero for small scattering angles and in the case of back scattering. Thus the most useful events are those which scatter into the limited regime of angles around 90^0.

Dependence of the differential cross section on the Compton scattering angle θ for different incident photon energies is shown on figure 3.3. One can see that for highly relativistic energies ($E > mc^2$), Compton scattering peaks mainly in the forward hemisphere and reaches its minimum intensity always at 90^0. In order to optimize the polarimeter for the parameter $M * \sigma$, detector systems should be slightly forwarded (see figure 3.3). In contrast, in the Thomson limit ($E << mc^2 = 511$ KeV), an ideal polarimeter would be optimized for the scattering

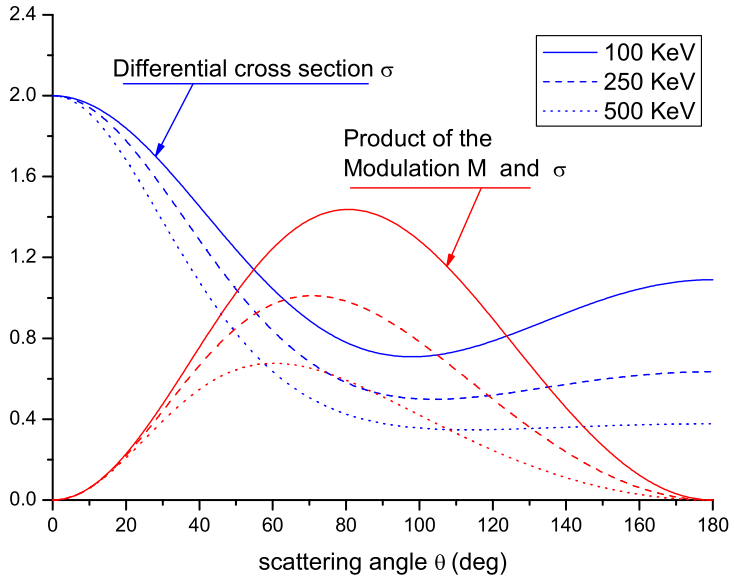

Figure 3.3: Differential cross section of Compton scattering and the product of the differential cross section times the modulation factor for 100% linearly polarized photons at different energies (Eq. 2.7 and Eq. 3.1).

angle of 90^o. Furthermore, because the information about the initial photon polarization is generally lost after the second scattering, the detector system should be optimized to detect single Compton events. The method discussed usually requires a possibility to rotate the polarimeter around the center axis of the scatterer in order to measure a complete angular distribution for the Compton scattered photons.

3.1.2 Detector material considerations and the "Kinematic event selection"

Efficiency of Compton scattering and photoabsorption is the key for the construction of an efficient polarimeter. Therefore both Compton scattering and photoabsorption processes should have large cross sections for a given detector material.

Figure 3.4 compares the total absorption efficiencies for Ge and Si. One can

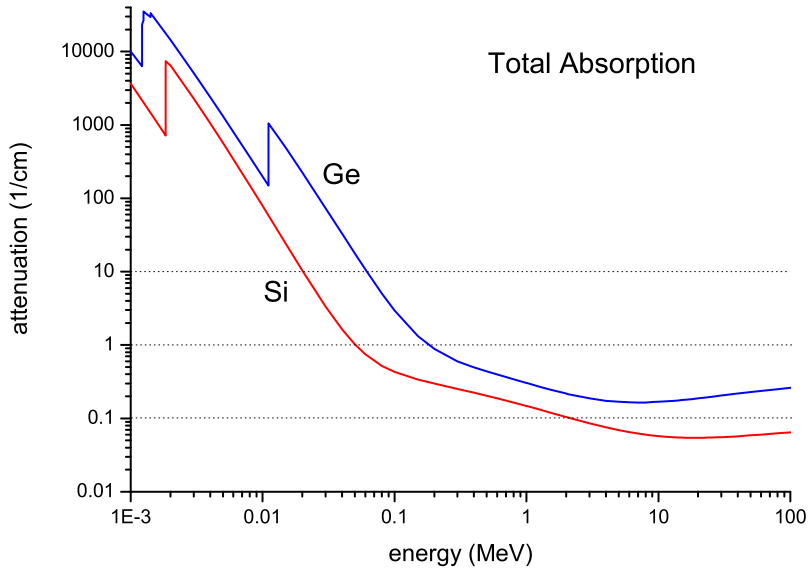

Figure 3.4: Total absorption efficiencies for Ge and Si crystals. The absorption efficiency is given in terms of the attenuation coefficient (see Eq. 2.13) [27, 28, 29, 30].

see, that Ge is in general more efficient as a photon absorber. Therefore it is more preferable to use it for polarimetry purposes. It will be shown later, that a Si detector has certain advantages for the polarimeters, optimized for the lower energy range.

The material selected for the active target should have large Compton scattering cross sections and should be relatively transparent for the scattered photons. In contrast the Compton photons should be detected with a detector having a large photo-absorption cross section.

Figure 3.6 shows a numerically simulated probability for multiple scattering inside an infinite Ge crystal. It was assumed that the multiple Compton scatterings are followed by a complete photoabsorption. With increasing photon energy Compton scattering becomes more important (see figure 3.5) and the probability for multiple Compton events increases drastically (see figure 3.6). Note, these calculations where done for an infinite crystal size. In order to select only single scattering events one must either reduce the size of the crystal or one should restrict the experiments to the low energy region (less than ≈ 200 KeV).

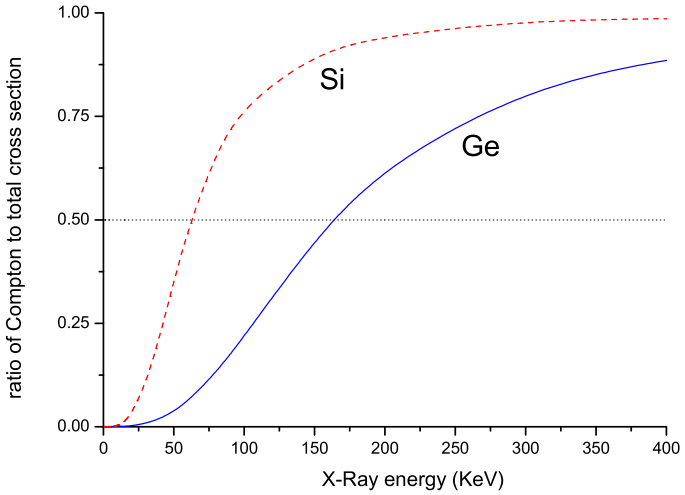

Figure 3.5: Contribution of the Compton scattering cross section to the total cross section of Ge and Si as function of photon energy. The level 0.5, where the Compton cross section is equal to the photo-absorption cross section indicates the energy region where the optimum performance of the detector system can be achieved.

Detector systems are usually based on scintillators and/or crystal Si/Ge material. Plastic or fibre scintillators are used as a target, providing reasonably good energy resolution and timing. Solid state Si [45] or Ge detectors [46, 47, 48, 49, 50], providing a much better energy resolution than scintillators, can also be used. Compared to Ge detectors, a Si detector has the advantage of having larger Compton scattering efficiency relative to photoabsorption, see figure 3.5. Heavy absorbers based on NaI(Tl), CsI(Na) scintillators [51, 52] can be used, having a large full energy peak efficiency.

Solid state detectors can be used where the energy resolution typical for Ge or Si detectors is required. It was demonstrated, that for the case of Ge, the sum spectrum decomposed from the Compton photon and the recoil electron energies has the Compton tail suppressed by a factor up to 10 [53].

As it was mentioned already the Compton scattering efficiency for Si is larger than for Ge which possess a higher photoabsorption efficiency. Therefore a detector combination, where Si detector is used as a scatterer and Ge as an absorber, can be considered as one of the best solution [54].

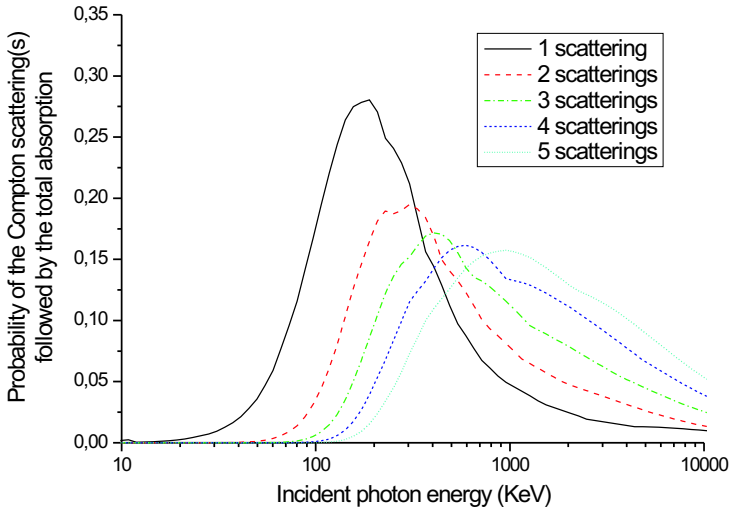

Figure 3.6: Numerically simulated multiple Compton scattering probability for Ge crystal: 1-5 Compton events, followed by total photoabsorption as function of incident photon energy. Also pair production was considered.

A good timing and a coincidence technique is required in all cases for an efficient background suppression. Besides this, a method called *kinematic event selection* is usually applied for the further background reduction (see for instance [50, 53, 55]): The electron energy deposition in the scatterer can be calculated using the equation 2.4 which requires a precise knowledge of the geometry of the detector system, i.e the angle θ. Having this knowledge, one can select only the events that obey this equation. For this the scatterer should be capable of detecting events of such energies. For the energy range less than $\approx$ 100 KeV the electron energy deposition can be very small, depending on the Compton scattering angle, and be in the same order as the electronic threshold (detector and electronic noise). For the incident photon energy of 200 KeV, the scattered electron energy deposition is equal to 56.3 KeV, for 60 KeV - 6.3 KeV, which is already near to the electronic threshold. An analysis of the dependence of the polarimeter efficiency on the low energy threshold was done in [55]. Larger polarimeter efficiencies can be achieved by lowering the energy threshold for the scatterer. Low energy threshold problem together with the dropping of the Compton efficiency at low photon energies constitutes the low energy limit for the Compton scattering polarimetry at the energy of $\approx$ 60 KeV.

3.1.3 Polarimeter quality considerations

There are several parameters widely used in order to compare efficiencies of different polarimeters. Among them is a Minimal Detectable Polarization (MDP), a sensitivity calibration Q, and different Figures of Merit F.

1. The most typical parameter to compare qualities of different polarimeters for astrophysical applications is the *Minimal Detectable Polarization* (MDP). The MDP is given by [55, 56]:

$$MDP(99\%) = \frac{1}{\varepsilon M}\frac{4.29}{S}\frac{\sqrt{\varepsilon S + B}}{AT} \tag{3.2}$$

which is defined for a conidence level of 99%, where S is the source photon flux, ε is the full-energy detection efficiency of the polarimeter for unpolarized photons, M is the modulation factor, A is the collecting area, and B is the background counting rate per unit surface, in a net observing time T. For the derivation of Eq. 3.2 was assumed that the counting rates of the source as well as for the background follow Poisson statistics. In the most common case where the observation is dominated by the background count rate ($B >> \varepsilon S$), an important parameter is the factor of merit, $R = \varepsilon M/\sqrt{B}$, which is typical for a given technology or configuration.

2. The *Sensitivity Calibration* Q of a polarimeter measures its response to linear polarization. The response of the ideal polarimeter, constructed from point-like detectors, is given by an analytical formula [25]:

$$Q_0 = \frac{1+\alpha}{1+\alpha+\alpha^2} \tag{3.3}$$

where $\alpha = E/m_0c^2$.

Polarization sensitivity of a nonideal polarimeter is a fraction of this value because of the finite size of detectors. These deviations from an ideal case make reliable calculations of the polarimeter sensitivity rather difficult. The sensitivity Q can be also determined experimentally. It is equal to the Modulation fraction M (see Eq. 3.1) for the 100% polarized radiation.

3. A method for comparing different type of polarimeters using a *Figure of Merit* was suggested by Logan et al. [57, 58]. They proposed to use as a quantitative description of a polarimeter quality a value:

$$F = \varepsilon Q^2 \tag{3.4}$$

The concept of merit allows to compare different polarimeters by answering the question: how long does one have to measure with a given polarimeter to obtain a certain asymmetry with a given accuracy?

But the resolving power of a polarimeter depends inversely on the peak resolution W, the ability of the detector to resolve individual peaks in a spectrum. The modified, more appropriate definition of the Figure of Merit would be [59, 60]:

$$F = \varepsilon Q^2 / W \tag{3.5}$$

For another possible definition of the Figure of Merit one can refer for instance to [61].

Issues to be considered for basic polarimeter construction

There are usually a few weak points in the basic polarimeter construction. Low detection efficiency due to incomplete coverage of the scatter material by the absorbers. Small active geometrical area; the scatter element must not be too large, because the scattered photon should have a high probability to escape after one interaction event. (After two ore more Compton scattering interactions, the polarization information is generally lost.) The necessity to avoid a significant smearing of the modulation, due to the photons scattered with different azimuthal angles or different angle θ_c, introduces the requirement of a large empty space between the target and the detectors [55]. This leads to rather small ratio of the effective area to the total geometrical area of the whole device, which can be extremely inconvenient for use in space limited experimental environments. These disadvantages and also the necessity to rotate the device, which provides additional difficulties, increase the minimal time of observation and make it difficult to measure time varying processes. In each of the preceding configurations the probability for the scattered photon to escape the target (scatterer) is strongly dependent on the point where the interaction occurs. This fact, besides reducing the modulation factor, can introduce systematic effects if the positioning, the spatial anisotropy and the time variability of the background and/or of the source counting rate are not completely kept under control, even if the whole system is allowed to rotate. All these disadvantages lead to a very limited spectrum of applications of the above listed devices. But as an advantage one can mention,

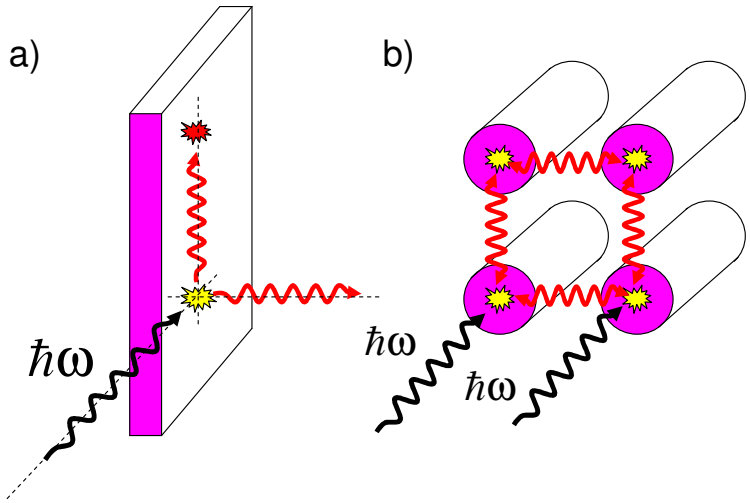

Figure 3.7: a) Single planar detector scheme; b) A possible geometry for the symmetric design.

that such polarimeters can be built using conventional X-ray detectors and in many cases do not require a special custom design. Due to the last factor such systems are still in use [50, 62].

Single detector scheme

Employing the rotational principle one can even build a polarimeter using one single very thin planar Ge detector, see figure 3.7a. In this case the scattering and absorbing take place in the same detector and the total energy deposition is detected [63, 64, 65]. A different event rate is observed for different crystal orientations, according to the Klein-Nishina formula. But such detectors usually have relatively low polarimeter efficiency in comparison for instance to double Ge polarimeters and a large background [66].

Symmetric scheme

In order to improve the efficiency of the polarimeter one can use a symmetric geometry, where each detector serves both as a scatterer and an absorber, see

figure 3.7b [46, 67, 68, 69, 70, 71]. For this geometry there is no need in collimating the scatterer, which reduces the efficiency of the polarimeter. The idea of a symmetric design is utilized in many modern polarimeter schemes based on *multiple integral (segmented) detectors.*

3.2 Multiple integral (segmented) detectors

Another scheme for an X-ray polarimeter utilizes segmented detectors and detector arrays. The typical material for the detectors is Ge. Very recently segmented Si(li) detectors have also become available. Such detectors exhibit a high energy resolution, good timing properties and two or tree-dimensional position sensitivity. The *kinematic data selection* is also allowed and used to suppress a possible background. As far as the same material for both the scatter and the absorber is used, the best performance can be achieved at energies where the Compton cross section of the incident photon and photo-absorption cross section for the scattered photon are of the same order. For Ge this energy is about 160 KeV, for CdZnTe, this is 260 KeV, for Si is 60 KeV respectively, see figure 3.5 [72]. For the CdZnTe the Photoelectric absorption limits its use to energies below 200 KeV. Therefore the best candidate for the polarimeter in an energy range of 100 – 350 KeV is Ge. The upper limit here is not principal. It arises from the fact, that in order to perform the *kinematic data selection* it is important to be able to determine the pixel of the first interaction in order to compute the scattering angle θ for each event. Fortunately due to the kinematics of the Compton process, below few 100 KeV the recoil electron energy deposition is always smaller than the consequent Compton photon energy deposition. The upper limit for the segmented polarimeters is determined by increasing efficiency of the Compton process with respect to the photo-absorption and correspondingly increasing the percentage of the multiple Compton scattering events, which introduce difficulties in the analysis, see figure 3.6. The application of the Compton scattering polarimetry can be extended up to energies of about a few MeV. The polarization sensitivity for a four-fold segmented large volume germanium detector was measured in [73] up to photon energies of 10 MeV.

The first approach to build an integrated polarimeter was to use a segmented

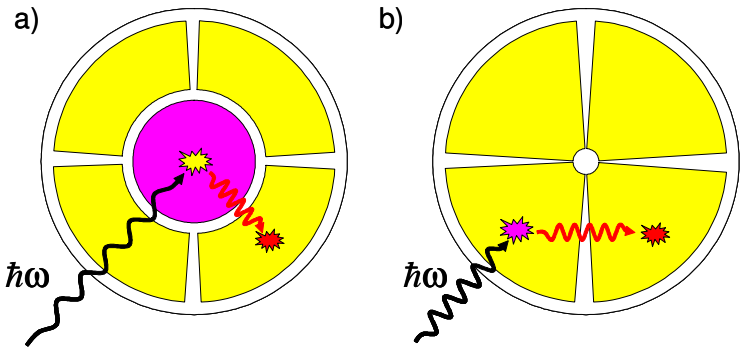

Figure 3.8: a) Segmented planar Ge(li) polarimeter with a central segment served as the scatterer; b) Radially symmetrical coaxial segmented polarimeter.

planar Ge(Li) detector symmetrically segmented around a central axis, see figure 3.8a. A central collimated ring shaped segment was used as a scatterer and 8 radial segments were used as absorbers. This provides a full coverage for the azimuthal angle and a large solid angle for detecting scattered photons [74]. A similar polarimeter was built using 4 radial segments instead of 8, providing a bit less modulation factor but easier maintaince [75].

A slightly different approach was to use coaxial Ge(Li) detectors radially segmented into 8 [76] or 4 [59] parts, see figure 3.8b. It these cases each segment serves both as a scatterer and an absorber, significantly increasing the effective scattering area.

3.2.1 Planar stripe and pixel detectors

In recent years the Compton polarimetry techniques have followed the progress in the development of solid state segmented detectors. Here in particular germanium segmented detectors (GSD) must be mentioned. The unique properties of such detectors are millimeter to sub-millimeter spatial resolution as well as a good time and energy resolution (e.g. 1.6 KeV at 60 KeV) [77]. Double sided stripe detectors and true pixel detectors can be used for polarimetry purposes, providing 2 dimensional spatial resolution with a fine segmentation, where each segment serves both as a scatterer and an absorber. The 2D position resolution provides a

good possibility to use the *kinematic data selection* for background suppression. Moreover, it was shown that solid state detectors even allow for the 3 dimensional determination of the photon interaction point [78]. This feature can further improve the polarimeter sensitivity.

The most typical problem of the segmented detectors is that events in adjacent pixels have serious systematic biases. This results from a combination of effects from charge sharing between strips (pixels), lateral diffusion of the charge cloud, different properties of the strips on the opposite faces of the detector, and gross geometry factor between adjacent pixels. Rather than to investigate these effects, it is easier to demand that there is at least one strip with no signal between the strips. This ensures a modest separation between two events, and reduces systematic effects to very low levels. This also reduces the detector efficiency due to an attenuation of the scattered radiation inside the detector. If the strips are very wide, this efficiency loss becomes significant. Thus in order to increase the polarimeter efficiency, the detector must have a fine segmentation. Nowadays, technically, it is possible to make the segmentation down to 0.2 mm width strips [77]. But in order to have relatively high efficiency for the detection of the scattered photon, the total detector thickness must be at least of the order of the absorption distance. For Ge, in the interesting energy range, it is around 10 mm, see figure 3.4. For example for 300 KeV it is 17 mm, for 50 KeV it is 0.6 mm. One must consider these values in order to choose the right detector segmentation. A detector with a large amount of stripes is difficult to operate and an efficiency of each stripe will be small in order to collect statistically enough counts. In order to optimize the stripe size, first one must consider that the probability of multiple events within one pixel should not be large. This limits the maximum size of the pixel. On the other hand, the Compton scattered photons must be efficiently absorbed within a distance of a few pixels. Note that the neighboring pixels can not participate in statistics because of the charge splitting events, which have no contrast to real Compton events. These conditions make the following empiric rule. The optimum segmentation size is 1/4 of the absorption distance for a given energy. Therefore it is practically better to build a polarimeter with the pixel size of about 0.5 to 2 mm for Ge type detectors [72]. The optimum pixel size can be different for different materials (Ge or Si) and different energy range (i.e. low

Incident Photon Energy, KeV	Scattered Electron Energy, KeV	Scattered Photon Energy, KeV	Attenuation Coefficient, 1/cm	Absorption Distance, mm	Desirable Segmentation, mm
30	1.7	28.3	13	0.7	0.2
40	2.9	37.1	6.2	1.6	0.4
60	6.3	53.7	3.3	3.0	0.7
100	16	84	1.0	10.5	2.6
200	56	144	0.25	40	10
400	176	224	0.17	60	15
800	488	311	0.11	88	22

Table 3.1: Germanium Detector segmentation, optimized for different photon energies. Compton Scattering at 90° assumed for the planar detector geometry.

energies $\lesssim$ 100 KeV or high energies up to 1 MeV). For Ge, one can see in table 3.1 that for the polarimetry purposes it is has no sense to make a segmentation of a Ge detector smaller than 0.5 mm. On the other hand, note that the *optimum* values for the energy region of 50 - 400 KeV vary by a factor of about 35, whereas for the case of Si the same values vary by a factor of about 5, compare table 3.2. For Si, the best segmentation would be 2 mm, optimized for lower energies, where Si has above mentioned advantages compared to Ge.

For further improvement of the detector position resolution, a pulse shape analysis of the real and mirror signals in the neighboring stripes can be exploited as well as a charge sharing effect in the adjacent stripes [79].

To summarize the advantages of the segmented planar detectors one should underline the following aspects:

1. A submillimeter (3D) position resolution together with the good energy resolution provide a perfect condition for the *kinematic data selection* and the efficient background suppression.

2. With the help of the *kinematic data selection*, the *Modulation factors* which can be achieved are significantly higher than reported for the scintillator polarimeters in the similar energy range [80].

Incident Photon Energy, KeV	Scattered Electron Energy, KeV	Scattered Photon Energy, KeV	Attenuation Coefficient, 1/cm	Absorption Distance, mm	Desirable Segmentation, mm
30	1.7	28.3	1.4	6.9	1.7
40	2.9	37.1	0.70	14.3	3.6
60	6.3	53.7	0.44	22.8	5.7
100	16	84	0.22	44.8	11
200	56	144	0.15	69	17
400	176	224	0.13	78	20
800	488	311	0.11	93	23

Table 3.2: Silicon Detector segmentation, optimized for different photon energies. Compton Scattering at 90° assumed for the planar detector geometry.

3. The fine segmentation and the symmetric design allow to achieve higher detection efficiencies compared to other schemes [50, 60, 80].

4. A full 360° coverage of the azimuthal scattering area does not require any rotation of the device. This can be essential in studying of the time varying processes.

Differences in the stripes efficiencies introduce a small unavoidable intrinsic anisotropy of the detector. The main cause of this anisotropy is probably due to the differences in the gap between the strips on the boron and lithium sides. This leads to an effect that an unpolarized beam can appear to have a small polarization if this anisotropy is not corrected. In any individual GSD, the magnitude of the anisotropy is equivalent to a polarization of less than 10%. This anisotropy can be calibrated and corrected with an unpolarized beam [80].

Scintillator technologies also provide a possibility to build finely subdivided detectors for the polarimetry purposes. The group of E. Costa [55] analyzed two different schemes of polarymeters based on scintillator fibres. Besides the above discussed one-phase model, the model where each pixel serves both as a scatterer and an analyzer, another possible configuration, which uses so called two-phase model was discussed. This is a model where the role of a scatterer and a detector

are committed to fibre detectors made from different kind of scintillators, more specialized for each function. It was shown, that using such configuration it is possible to increase significantly the efficiency of the polarimeter. It was also shown that in order to achieve a slightly better performance one can use a hexagonal shape of the sections instead of a square one. Such detector scheme, based on plastic/CsI fibre would be specialized for the energy range of 25÷250 KeV. Unfortunately it is difficult to apply such technology to Ge/Si crystal segmented detectors and detector arrays.

3.3 Other polarimeter types

It is also possible to improve the basic polarimeter scheme, based on a separate scatterer and a detector. In [51, 52] a polarimeter based on plastic scintillator, serving as a scatterer, surrounded by CsI(Na) and NaI(Tl) Scintillator absorbers, is presented. Such a system provides a full coverage of the azimuthal scattering angle by absorbers, relatively large effective scattering area and more specialized detectors for the scattering and absorbing function and for different scattering angles.

For the polarimetry purposes big detector clusters can be utilized. In principle every detector system which analyzes multiple scatterings inside the detector and has a position resolution, can be used as a polarimeter. The example of the EUROBALL cluster was evaluated in [61] and the "Clover" detector for the EUROGAM array was evaluated in [81].

The polarimeters, based on fine-segmented detectors and detector arrays can also be integrated into imaging devices. For instance a *Coded Aperture* in front of a doubly segmented detector can provide a scheme for a telescope which is an improvement of a simple pin-hole camera [80]. In addition, the 3D detectors can serve as Compton camera (see for instance [82]), providing aperture-free imaging possibilities. Such combinations can find many applications for instance in astrophysics and nuclear medicine.

3.3.1 Measuring the polarization of high energy photons

For the high energy domain a polarimeter based on electron-positron pair production effect can be built. Detection of γ-ray linear polarization by pair production was suggested by Yang [83], Berlin and Madansky [84] and Wick [85]. They studied the azimuthal distribution of coplanar pairs with respect to the photon polarization plane. A full QED analysis of polarization effects in pair production was done by Olse and Maximon [86].

Several polarimeters employing the pair production effect in GeV energy range were built since 1960 [87, 88]. Electrons and positrons after creation are separated in a magnetic field and detected by solid state detectors. Recently a proposal for a polarimeter scheme for several GeV energy, based on silicon micro-strip detector was reported [43]. For this case the use of a magnetic field in not needed because of the high position resolution of a PSD.

3.3.2 Measuring the circular polarization

For completeness one should also address the topic of a circular polarization, although this subject will not be discussed within the context of this work.

A circular polarization can be measured by means of the Compton scattering on polarized electrons available in magnetized iron [89]. A theoretical description of polarization relations in Compton scattering was presented in [90]. A correlation between electron spin polarization and circular polarization of photons was discussed. Also physics of production and detection of circularly polarized γ quanta by a Compton scattering with polarized electrons was described. The scattering cross section depends on the relative direction of the scattered photon and electron spin. Reversing the spins of the scattering electrons results in a change of the scattered intensity if the X-ray radiation is circularly polarized:

$$\frac{d\sigma}{d\Omega} = \frac{r_0^2}{2}\frac{E'^2}{E^2}(\Phi_0 + P_1\Phi_1 + P_c \cdot f\Phi_c) \tag{3.6}$$

where

P_1 - degree of linear polarization,

P_c - degree of circular polarization of the photons. It is positive if the radiation

is right circularly polarized,
f - fraction of oriented electrons.

Φ_0 is Klein-Nishina unpolarized type of expression, whereas Φ_1 and Φ_c are the polarization dependent parts of the cross section:

$$\begin{aligned} \Phi_0 &= 1 + \cos^2\theta + (k_0 - k)(1 - \cos\theta) \\ \Phi_1 &= \sin^2\theta \\ \Phi_c &= -(1 - \cos\theta)\left((k_0 + k)\cos\theta\cos\psi + k\sin\theta\sin\psi\sin\phi\right) \end{aligned} \tag{3.7}$$

where ψ is the angle between the direction of the incident photon $\vec{k_0}$ and the electron spin $\vec{s}$. From the expression 3.7 one can see that there are two possibilities of measuring the circular polarization. The most obvious way is to reverse the spin direction changing ψ into $\psi + \pi$ thus reversing the sign of Φ_c. Alternatively one can change the counter position from ϕ to $\phi + \pi$ keeping the spin direction fixed.

Most favorable geometry, where the ratio Φ_c/Φ_0 has a maximum is forward or backward. The ratio is bigger for the backward direction but the intensity for this case is smaller, therefore the forwarded geometry is usually preferred [91]. This method works also for high photon energies up to ≈ 60 MeV [92].

Chapter 4

Theoretical description of RR and REC

The *Radiative Recombination* (RR) and the *Radiative Electron Capture* (REC) are the dominating processes in ion-electron and ion-atom collisions respectively. One must mention that for high-Z projectiles and low-Z targets, where a target electron having a velocity $v_T = (\alpha Z_T/n_T)c$ (much smaller than the ion velocity, where α is a fine structure constant, Z_T is an ion charge and n_T is a principle quantum number), is considered as quasifree, the REC process is almost identical to the RR, which in turn, is the time-inverse of the photoelectric effect, see figure 4.1. Therefore, the measurements of the radiative electron capture by heavy ions allow us to study the strong field effects in the photoionization which is one of the most fundamental interaction processes between light and matter [93]. In this chapter we will concentrate on some details of the RR process. It will be shown that total and angular differential cross sections are dominated by large cancellation effects between retardation and relativistic transformation. In contrast no such effects seem to be present for the linear polarization of RR photons. Therefore relativistic effects with respect to the wave function and the motion of the electron show up in a particular clean manner.

By definition, RR is the process, in which a free electron with kinetic energy T_e is captured into a bound atomic state n (binding energy $|\epsilon_n|$) with the simultaneous emission of a photon of energy $\hbar\omega$. Energy conservation requires that $T_e = \hbar\omega - |\epsilon_n|$. We choose the direction of the incoming electron as the z direction,

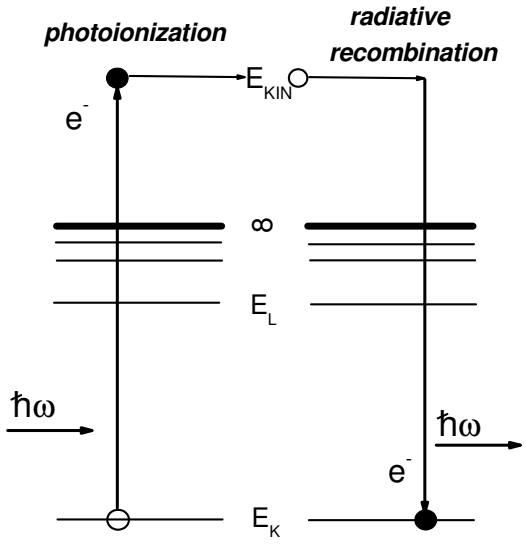

Figure 4.1: Schematic sketch of the time reversed processes: the photoionization and the radiative recombination.

so that $\theta^{'}$ is the emission angle of the photon. Since the radiative recombination takes place in a moving system, we distinguish its quantities (energy, frequency and angles) by a prime from the unprimed laboratory quantities.

Mathematical formulation of the time reversal analogy between Radiative Recombination and Photoionization is expressed in terms of the *principle of detailed ballance* [94]. The RR cross section $\sigma_{RR}(E^{'},\theta^{'})$ is strictly related to the corresponding photoionization cross section $\sigma_{ph}(E^{'},\theta^{'})$:

$$\begin{aligned}
\frac{d^2\sigma_{RR}(E',\theta')}{dE'd\Omega'} &= \frac{(\omega'/c)^2}{p'^2}\,\frac{d^2\sigma_{ph}(E',\theta')}{dE'd\Omega'} \\
&= \left(\frac{\hbar\omega'}{m_ec^2}\right)^2\,\frac{1}{\beta^2\gamma^2}\,\frac{d^2\sigma_{ph}(E',\theta')}{dE'd\Omega'} \\
&= \frac{(\gamma-1+|\epsilon_b|/m_ec^2)^2}{\gamma^2-1}\,\frac{d^2\sigma_{ph}(E',\theta')}{dE'd\Omega'}. \qquad (4.1)
\end{aligned}$$

This equation is valid for one magnetic substate. If the total photoelectric cross section is an average over a subshell, one has to multiply the right-hand of Equation 4.1 by a factor $(2J_n+1)$ in order to compensate for this averaging procedure.

4.1 The Stobbe formula for K-shell REC

In the non-relativistic dipole approximation the process of Radiative Recombination has been theoretically treated by Stobbe [95]. Using the exact Coulomb continuum wavefunction he derived for the K-shell RR the following expression:

$$\sigma_{\mathrm{RR}}^{\mathrm{Stobbe}} = \frac{2^8\pi^2\alpha}{3}\lambda_c^2\left(\frac{\nu^3}{1+\nu^2}\right)^2 \frac{e^{-4\nu\arctan(1/\nu)}}{1-e^{-2\pi\nu}}, \tag{4.2}$$

where $\lambda_c = \hbar/m_e c$ is the Compton wavelength of the electron and $\nu = Ze^2/\hbar v$ is the Sommerfeld parameter. The constants in front of the ν-dependent terms make up a factor of 9164.7 barn.

The Stobbe formula proves to be quite useful to estimate the total cross section of the REC into the K-shell up to projectile energies of few hundred MeV/u, corresponding to electron kinetic energies $(\gamma-1)m_e c^2$ well below the electron rest energy [13].

Note that the effects of retardation are not included in the dipole approximation ($e^{i\mathbf{kr}} \rightarrow 1$) and the angular differential cross section shows $\frac{d\sigma^{dipole}}{d\Omega} \propto sin^2\theta'$ distribution in the *emitter* frame (here θ' denotes the emission angle in the emitter frame).

4.2 Born approximation for K-shell REC and the angular distribution

The Born approximation treats completely the effect of the retardation which was neglected in the Stobbe formula, but in it assumes a plane electron wavefunction.

The result for the $\sigma_{RR}(E', \theta')$ is obtained from the corresponding photoionization cross section [96] by applying the principle of the detailed ballance, Equation 4.1:

$$\frac{d\sigma_{RR}(\theta')}{d\Omega'} \propto \frac{sin^2\theta'}{(1+\beta\cos\theta')^4} \tag{4.3}$$

where the maximum is shifted towards backward angles. After applying the Lorentz transformations:

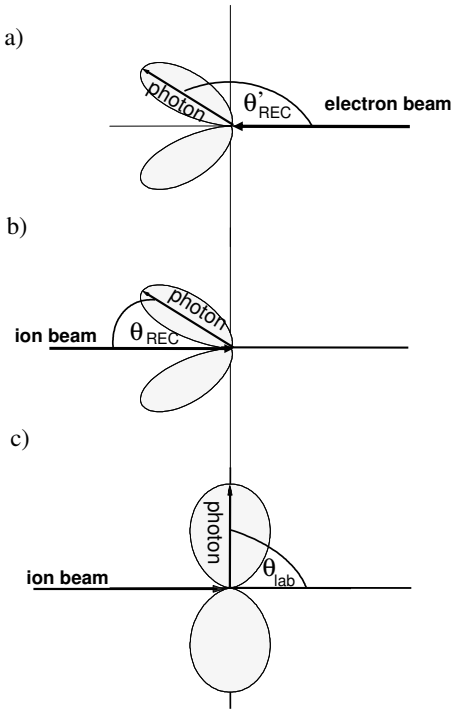

Figure 4.2: Schematic illustration of angular distributions in polar diagrams: (a) radiative recombination in the projectile frame, (b) radiative electron capture in the projectile frame, (c) Radiative electron capture in the target (laboratory) frame.

$$\begin{aligned} \cos\theta' &= \frac{\cos\theta - \beta}{1 - \beta\cos\theta} \\ \frac{d\Omega'}{d\Omega} &= \frac{1}{\gamma^2(1-\beta\cos\theta)^2} \\ E' &= \frac{E}{\gamma(1+\beta\cos\theta)} \end{aligned} \tag{4.4}$$

we obtain:

$$\frac{d\sigma_{RR}}{d\Omega} \propto sin^2\theta \tag{4.5}$$

This pure $sin^2\theta$ distribution is a result of the complete cancellation between the effects of the retardation, i.e. of higher multipoles (leading to a deviation from a $sin^2\theta$ distribution) and the Lorentz transformation to the laboratory system, see figure 4.2. This effect has been first observed by Spindler [97, 98].

4.3 Angular distributions from the exact calculation

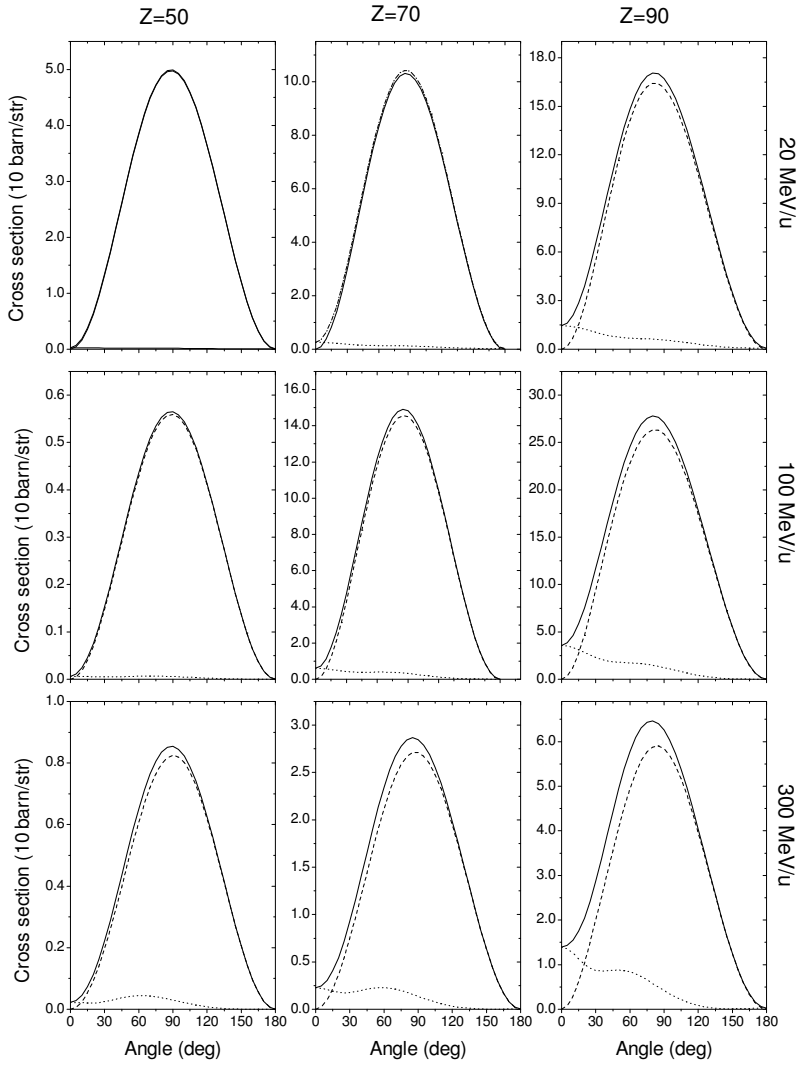

Figure 4.3: Angle-differential REC cross sections for capture into the K shell of projectiles with charge numbers $Z = 50$, 70, and 90 for projectile energies of 20, 100, and 300 MeV/u. Spin-flip (dotted lines) and non-spin-flip contributions (dashed lines) are shown separately. From [12], modified according to [99].

Figure 4.3 shows results of the exact relativistic numerical calculations of the angle-differential K-REC cross sections. Quite generally, the differential cross

section for radiative recombination into $l = 0$ states of a spinless electron vanishes in the forward and in the backward direction because initial and final electronic states have $m_l = 0$, so that the emission of a transverse photon with angular momentum ± 1 in its direction of motion is forbidden by angular momentum conservation. This means that RR and REC into $l = 0$ states at forward or backward angles can occur only by spin-flip processes mediated by magnetic interactions aa relativistic velocities [12, 100, 101, 102, 103]. Therefore deviations from the pure $sin^2\theta$ distribution at 0^o and 180^o angles gives a signature of the spin-flip processes, which can be measured experimentally. On the figure 4.3 one can see that with increasing energy and the projectile charge, the spin-flip contributions become more prominent.

4.4 Photon Polarization

The study of the linear and the circular photon polarization is one possible way to obtain more detailed information about dynamics of the RR or REC processes. A measurement of the linear polarization is sensitive to an interferences between right-hand and left-hand circular polarization (helicity) of the photons. In this chapter we follow closely papers of J. Eichler et al. and A. Surzhykov at al. [18, 20, 19, 21]. The polarization vector $\mathbf{u}$ is defined:

$$\mathbf{u}(\chi) = \frac{1}{\sqrt{2}} \left(e^{-i\chi}\ \mathbf{u}_{+1} + e^{i\chi}\ \mathbf{u}_{-1} \right) , \tag{4.6}$$

where $\mathbf{u}_{\pm}$ are the *circular-polarization* vectors, and χ is the angle between $\mathbf{u}(\chi)$ and a scattering plane, the plane defined by the ion beam momentum and the photon momentum $\mathbf{k}$, see figure 4.4a.

The polarization of a photon beam in a mixed state is described in terms of the spin-density matrix. Since the photon (with spin $S = 1$) has only two allowed spin (or helicity) states $|\mathbf{k}\lambda\rangle$, $\lambda = \pm 1$, the spin–density matrix of the photon is a 2×2 matrix and, hence, can be parameterized by the three (real) *Stokes* parameters [104, 105]:

$$\left\langle \mathbf{k}\lambda \,|\, \hat{\rho}_\gamma \,|\, \mathbf{k}\lambda' \right\rangle = \frac{1}{2} \begin{pmatrix} 1 + P_3 & P_1 - iP_2 \\ P_1 + iP_2 & 1 - P_3 \end{pmatrix} . \tag{4.7}$$

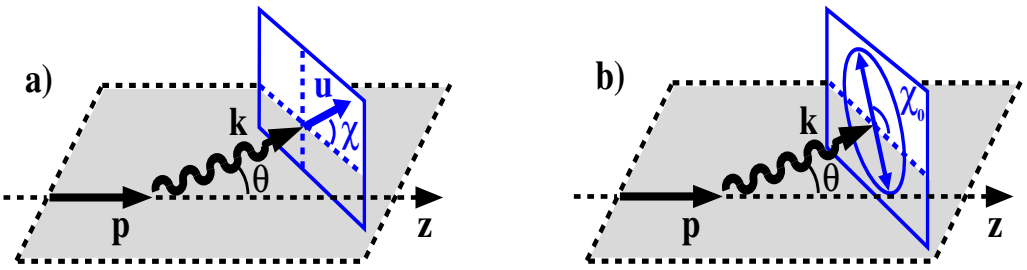

Figure 4.4: a) The unit vector $\mathbf{u}(\chi)$ of the linear polarization is defined in the plane, which is perpendicular to the photon momentum $\mathbf{k}$, and is characterized by an angle χ with respect to the scattering plane. b) Definition of the polarization ellipse; its principal axis is characterized by χ_0, the angle with respect to the scattering plane in the given measurement (right plot).

Stokes parameter P_3 reflects the degree of *circular* polarization, the two parameters P_1 and P_2 together denote the (degree and direction of the) *linear* polarization of the light in the plane perpendicular to the photon momentum $\mathbf{k}$. Experimentally, these Stokes parameters are determined simply by measuring the intensities of the light I_χ, linearly polarized under the different angles χ with respect to the scattering plane. For instance, the parameter P_1 is given by the intensity ratio:

$$P_1 = \frac{I_0 - I_{90}}{I_0 + I_{90}}, \tag{4.8}$$

while the parameter P_2 is obtained from a very similar ratio at angles $\chi = 45$ and $\chi = 135$ degrees, respectively (see figure 4.4b):

$$P_2 = \frac{I_{45} - I_{135}}{I_{45} + I_{135}}\,. \tag{4.9}$$

Instead of the Stokes parameters, however, in experimental studies it is more convenient to represent the polarization state of the photon beam in terms of a polarization ellipse which is defined in the plane perpendicular to $\mathbf{k}$. In such a representation, the degree of linear polarization:

$$P_L \;=\; \sqrt{{P_1}^2 + {P_2}^2} \tag{4.10}$$

is characterized by the relative length of the principal axis (of the ellipse) and the direction by its angle χ_0 with respect to the scattering plane. Figure 4.4b shows the *concept* of the polarization ellipse and how χ_0 is defined; when expressed in terms of the Stokes parameters, this angle is given by the two ratios [104]:

$$\cos 2\chi_0 \;=\; \frac{P_1}{P_L}, \qquad \sin 2\chi_0 \;=\; \frac{P_2}{P_L} \tag{4.11}$$

The density matrix 4.7 is obtained from the final–state density matrix by taking the trace over all quantum numbers of the residual ion [105]:

$$\begin{aligned} \left\langle \mathbf{k}\lambda \mid \hat{\rho}_\gamma \mid \mathbf{k}\lambda^{'} \right\rangle &= Tr_{\,F\,M_F}\,(\hat{\rho}_f) \\ &= \sum_{F\,M_F} \left\langle F\,M_F,\,\mathbf{k}\lambda \mid \hat{\rho}_f \mid F\,M_F,\,\mathbf{k}\lambda^{'} \right\rangle . \end{aligned} \tag{4.12}$$

In this general form, the photon matrix 4.12 still applies for any arbitrary spin of the nucleus. As indicated by its labels λ and λ', moreover, this matrix refers to the helicity representation of the photon states. Assuming a zero nuclear spin ($I_0 = M_0 = 0$), it simplifies to [20]:

$$\begin{aligned} \left\langle \mathbf{k}\lambda \mid \hat{\rho}_\gamma \mid \mathbf{k}\lambda^{'} \right\rangle &= \sum_{\mu_b} \sum_{m_s m_s^{'}} M^{RR}_{b,\,\mathbf{p}}(m_s,\lambda,\mu_b)\; M^{RR*}_{b,\,\mathbf{p}}(m_s^{'},\lambda^{'},\mu_b) \\ &\times \left\langle \mathbf{p}\,m_s \mid \hat{\rho}_e \mid \mathbf{p}\,m_s^{'} \right\rangle . \end{aligned} \tag{4.13}$$

while the elements of the transition matrix $M^{RR}_{b,\,\mathbf{p}}$, which describe the interaction of the ion with the radiation field, take the standard form [20]:

$$\begin{aligned} M^{RR}_{b,\,\mathbf{p}}(m_s,\lambda,\mu_b) &= \left\langle j_b\mu_b,\,\mathbf{k}\lambda \,\middle|\, \hat{R} \,\middle|\, \mathbf{p}m_s \right\rangle \\ &= C \int d^3r\; \psi^{+}_{j_b\mu_b}(\mathbf{r})\,\alpha\,\hat{\mathbf{u}}^{*}_{\lambda}\,e^{-i\mathbf{kr}}\,\psi_{\mathbf{p},m_s}(\mathbf{r}) . \end{aligned} \tag{4.14}$$

In recent years, this *relativistic* form of the transition matrix has been widely used for studying the radiative recombination of high–Z ions at intermediate and high collision energies [106]. For capture into bare ions, $\psi_{j_b\mu_b}(\mathbf{r})$ and $\psi_{\mathbf{p},m_s}(\mathbf{r})$ are the known solutions of the Dirac Hamiltonian for a bound or continuum electron, respectively. Moreover, the unit vector $\hat{u}_\lambda$ denotes the polarization of the photons. For the numerical calculation of the matrix element 4.14, the computer code DIRAC [107] was used.

4.4.1 Theoretical Results for Photon Polarization

Figure 4.5 shows the degree of linear photon polarization P_1 as a function of the emission angle θ for various projectile energies for the capture into bare uranium ions. One obtains a very high degree of polarization for almost all emission angles. Eventually, in the nonrelativistic limit, the linear polarization in the scattering

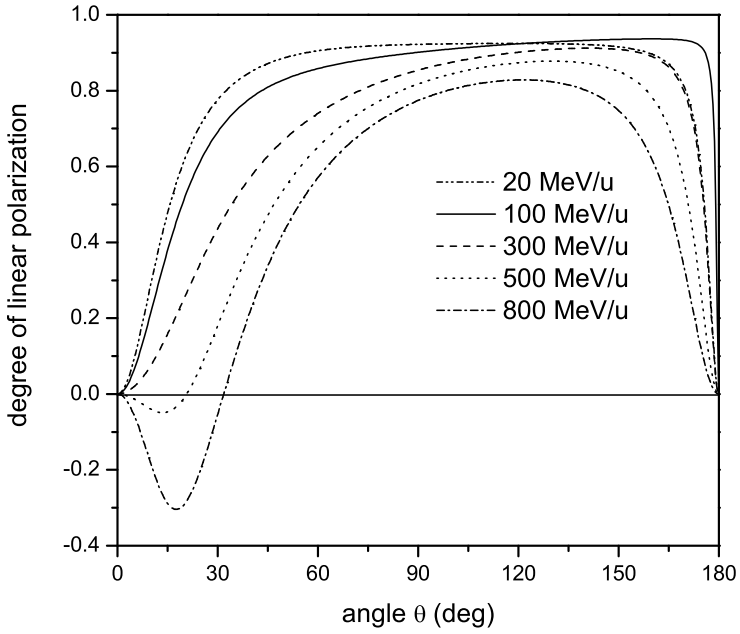

Figure 4.5: Energy dependence of the linear photon polarization as a function of the emission angle θ for K-REC into bare uranium ions (Z=92) [18, 19].

plane $P_{\parallel}^{lin} = 1$, is independent of Z [95, 108]. The strong depolarization effect in the relativistic case is mediated by magnetic interactions and a strong spin-orbital coupling in presence of the heavy nucleus.

It is interesting to note that one obtains a "cross-over" at about 500 MeV/u, beyond which the linear polarization becomes increasingly negative at forward angles. This means that preferable photon polarization is then perpendicular to the scattering plane. This corresponds to the "cross-over" observed in the photoeffect [108, 109, 110, 111], taking into account a replacement $\theta \rightarrow \pi - \theta$ and the Lorentz transformation to the atomic rest frame, which compresses the angular distribution at forward angles, see chapter 4.2. For the time-reversed photoeffect analog, at relativistic photon energies, the Dirac theory predicts maximum electron emission in the direction of the magnetic field.

The polarization angular dependance for capture into bare argon ions (Z=18)

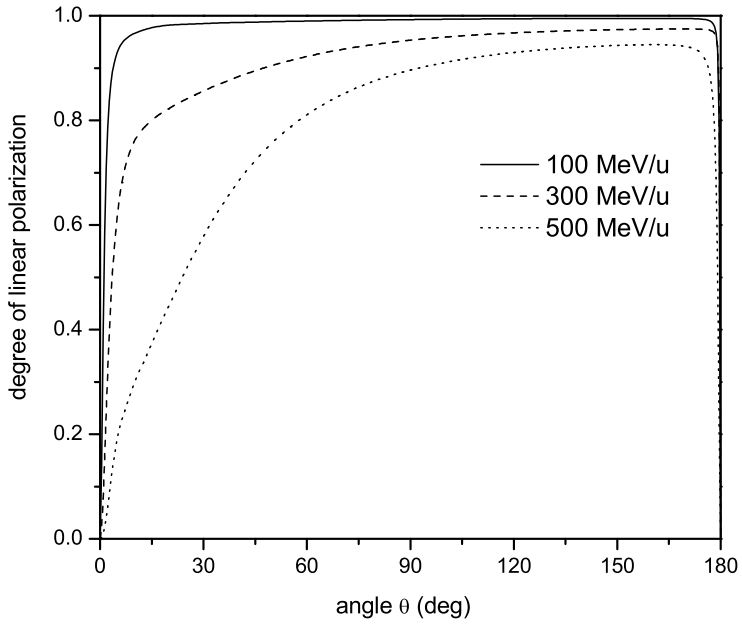

Figure 4.6: Energy dependence of the linear photon polarization as a function of the emission angle θ for K-REC into bare argon ions (Z=18) [18, 19].

is shown in figure 4.6. One can see that the depolarization effect is much smaller for low Z ions, what can be partially explained by an importance of the spin-orbital interaction which is much stronger in high-Z regime.

The degree of circular polarization is displayed in Fig. 4.7, assuming that the incoming electron has the spin projection $m_s = \frac{1}{2}$. At forward angles, a transition can occur only if the photon carries away the angular momentum $\lambda = 1$ (with respect to the electron direction) leaving the electron with the spin projection $-\frac{1}{2}$. At backward angles, the transition is achieved by $\lambda = -1$. Corresponding results have been obtained for the photoelectric effect [108].

To gain even more detailed insight into the dynamics of the REC/RR process, one can consider possible spin polarization of the particles, participating in the process. For capture of unpolarized electrons, only the Stokes parameter P_1 is non-zero, while P_2 is identically zero, meaning that the polarization of the

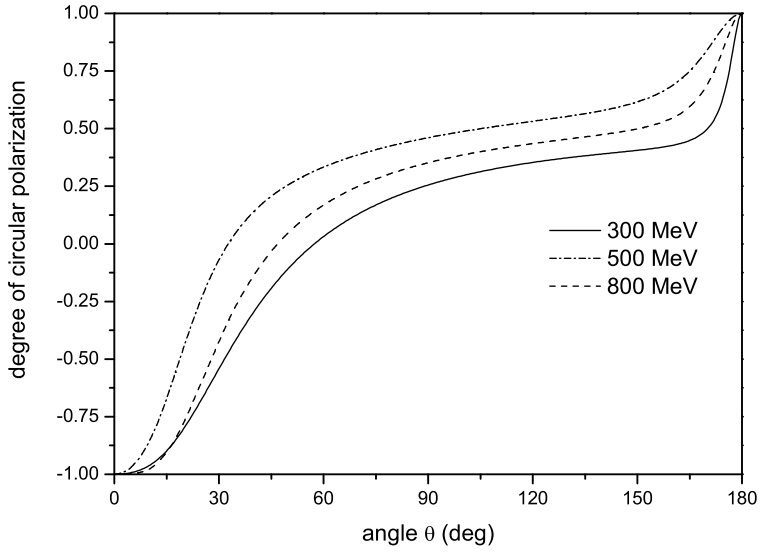

Figure 4.7: Energy dependence of the circular photon polarization (assuming $m_s = \frac{1}{2}$) as a function of the observation angle θ of the photon for K-RR at a projectile energies of 300 MeV, 500 MeV and 800 MeV for bare uranium [20].

RR/REC radiation is always within the scattering plane. For capture of the longitudinally spin polarized electrons, the Stokes parameter P_2 becomes non-zero, while P_1 does not change, see figure 4.8. This leads to an overall rotation of the linear polarization of the RR/REC photons out of the scattering plane, see Eq. 4.11. Due to a symmetry of the process with respect to the electron and the ion, a similar effect must occur for capture of an electron by a spin polarized ion beam [19]. This effect is limited to the case of I $> \frac{1}{2}$, where I is a nuclear spin.

The described effect can lead to an application is an ion beam spin polarization diagnostics. Note that for energetic ion-atom collisions the REC process is dominant and the K-REC photon polarization measurement should be an efficient tool for controlling of the ion beam spin polarization.

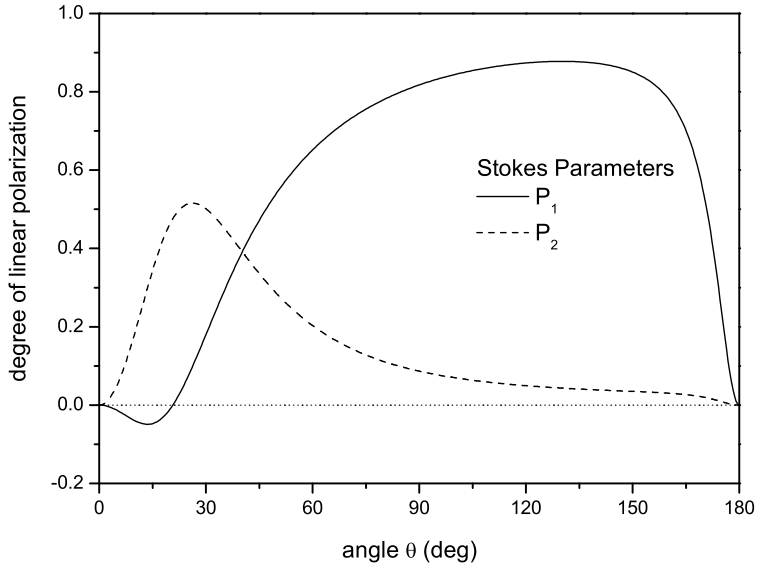

Figure 4.8: The Stokes parameters P_1 and P_2 of recombination/REC photons for capture of 100% polarized electrons into the K–shell of the bare uranium ions at an energy of 500 MeV/u [19].

Chapter 5

Status of the experimental studies of REC in comparison with the theory

5.1 Total cross sections

An absolute measurement of total cross sections requires a detailed knowledge of the beam and target geometry as well as the gas density and beam intensity. The uncertainties introduced by these factors usually amount to about 30% [13].

Figures 5.1a and 5.1b show a comparison of all available experimental results for total cross section of REC with theoretical predictions. Adiabaticity parameter η is defined here:

$$\eta = 1/\nu^2 \simeq 40.31 \times \frac{E_{\mathrm{kin}}(\mathrm{MeV/u})}{Z^2}. \tag{5.1}$$

The data were collected at the BEVALAC (compare [114]) and at the FRS/ESR facilities. For a comparison with theory, two competing processes at relatively low energies $\approx 100MeV$ were taken into account, i.e. the REC and the non-radiative electron capture NRC. See figure 5.2 for comparison of the experimental data with the theory. For NRC, the relativistic eikonal approximation was applied [115, 116, 117], which yields estimates for cross sections that are accurate within a factor of two [114, 118]. For REC, the Stobbe theory [95] was

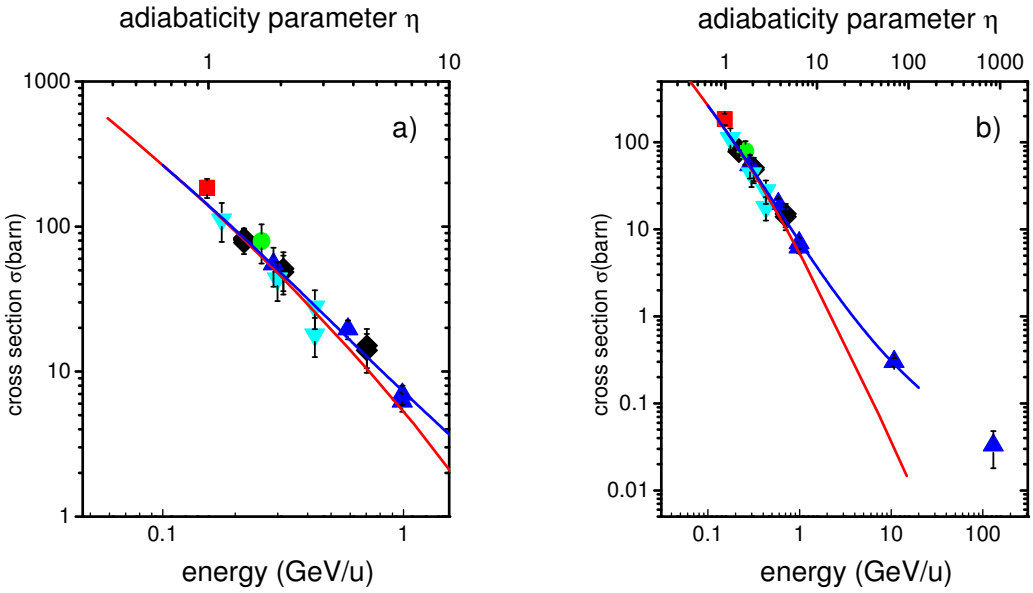

Figure 5.1: a:) Total electron-capture cross-sections per target electron measured for heavy bare ions ($Z \geq 54$) in collisions with light target atoms (molecules). The results are plotted as a function of the η-Parameter and are compared with the result of a relativistic exact calculation for $Z = 80$ as well as with the prediction of the non-relativistic dipole-approximation. b:) Same as a) but extended to high relativistic energies. The data points at 12 GeV/u and 168 GeV/u, are taken from [112] and [113] respectively.

used. One can see that for the light targets NRC process can be neglected for the case of U^{92+} projectiles at 295 MeV/u. Figures 5.1a and 5.1b show a good agreement between the experimental data and the theoretical predictions. The experimental data confirm the strong cancellation effects between various higher order multipoles and relativistic effects.

The method applied at the ESR is a relative measurement of total cross section to the K-shell cross section. Here, the total electron pick-up processes are normalized to the number of K-REC events registered by an x-ray detector. The electron-capture cross section, σ, is given then by the expression:

$$\sigma = \frac{N^{U^{91+}}}{N^{K-REC}} \cdot \epsilon \cdot \int \frac{d\sigma_K^{REC}}{d\Omega} d\Omega \tag{5.2}$$

where $N^{U^{91+}}$ is the number of down-charged U^{91+} ions registered by the particle detector, $d\sigma_K^{REC}(\theta) \,/\, d\Omega$ is the theoretical differential cross section for K-REC at

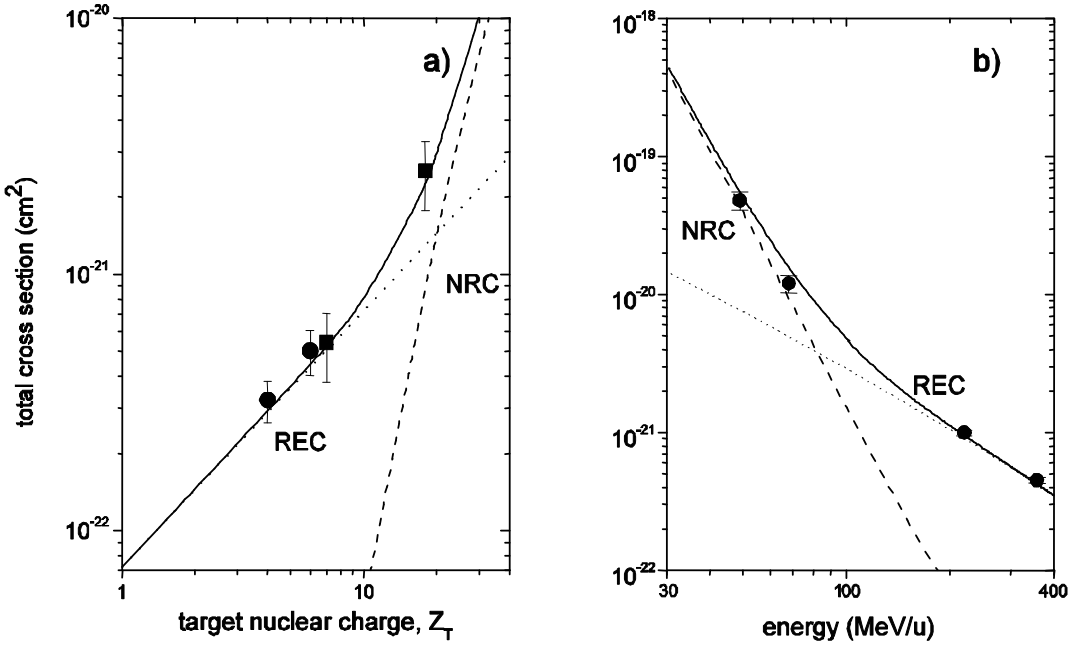

Figure 5.2: a): Total electron-capture cross sections for U^{92+} on a N_2 target versus projectile energy. The dotted line represents the result of the eikonal approach for the NRC process [117]. The dashed line gives the prediction obtained for REC within the dipole approximation. The solid line refers to the sum of both predictions. b):Total electron-capture cross-sections for bare U^{92+} at 295 MeV/u colliding with gaseous targets ($U^{92+} \rightarrow N_2$, Ar) and with solid targets ($U^{92+} \rightarrow$Be, C). For N_2 the cross section per atom is given. The results are compared with the theoretical cross-section predictions for the NRC and the REC processes (dashed and dotted lines). The resulting total electron-capture cross-sections are given by the full line.

the angle of observation θ, N^{K-REC} is the number of K-REC photons registered by the x-ray detector, ε is the photon detection efficiency and $d\Omega$ is the solid angle spanned by the x-ray detector. The latter two factors define the overall x-ray detection efficiency, and a precise knowledge of their absolute values determines the final experimental accuracy. The detector efficiencies are measured with absolutely calibrated X-Ray sources. The estimated uncertainty amounts to 5 %.

5.2 Relative angular-differential cross sections

In comparison with total cross section measurements at the ESR, the angular differential cross section studies do not require any theoretical value for the normalization. Instead of this, measured Ly-α_2+ M1 transitions are used for normalization purposes. Since the Ly-α_2 and the M1 transitions arise from a decay of the $2p_{1/2}$ and the $2s_{1/2}$ levels, the corresponding line intensity is isotropic in the emitter frame (see e.g. [106]). In addition all solid angle uncertainties are cancelled out by this normalization procedure and overall precision depends mainly on detector efficiency calibration.

As it was shown in the previous section, the total REC cross sections are insensitive to the relativistic contributions at intermediate energies. In contrast to

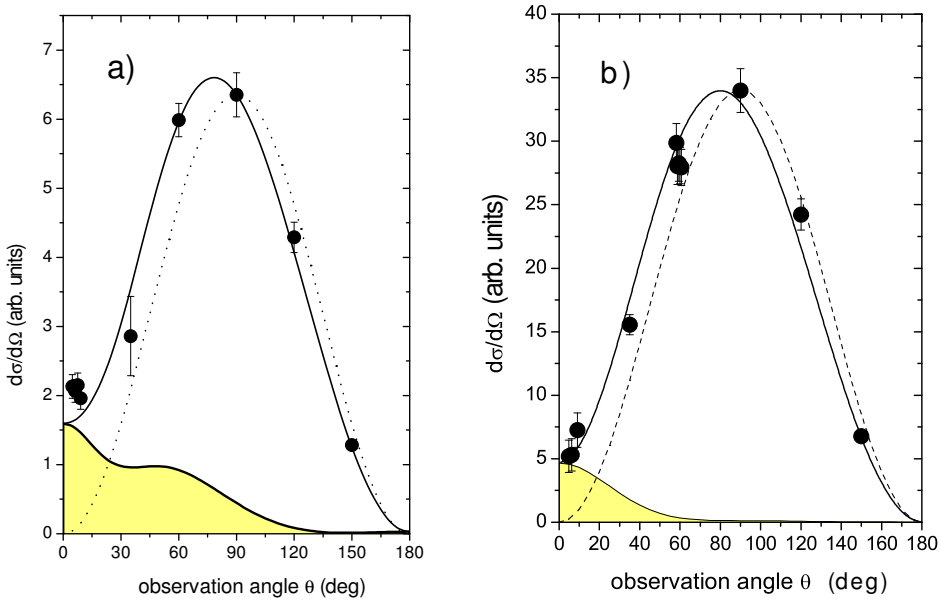

Figure 5.3: a:) Angular distribution for REC into the K shell of bare uranium (solid circles) as a function of the observation angle θ (309.7 MeV/u U^{92+} $\rightarrow N_2$) [15]. The solid line refers to the complete relativistic calculations and the shaded area to the spin-flip contributions [101, 12]. The $\sin^2\theta$ shape of the nonrelativistic theory is given by the dashed line. The experimental data and the nonrelativistic theory are normalized to the result of the complete calculations at 90°. b):Angular distributions for K-REC at 88 MeV/u U^{92+} $\rightarrow N_2$ collisions [16]. Solid circles: experimental result; solid line: relativistic calculations; shaded area: spin-flip contributions; dotted line: $\sin^2\theta$ distribution.

this, the differential cross section and in particular angular distributions show significant deviations from the non-relativistic dipole-approximation predictions. This theory predicts the $\sin^2\theta$ distribution, which is a result of the complete cancellation between the retardation and the Lorentz transformation [119]. However, at the projectile energies of 300MeV/u and for $Z = 92$ a significant cross section at forward angles has been predicted for REC into the K shell [11, 12, 101] and has been shown to be a unique signature of spin-flip transitions and confirmed experimentally.

Figures 5.3a and 5.3b show experimental results for the angular distribution studies [15, 16]. The data were normalized to the theoretical prediction at 90°. One can clearly see a good agreement between the experimental results and the full-relativistic theory which significantly deviates from the symmetrical $\sin^2\theta$ shape. This is an unambiguous identification of spin-flip transitions occurring in relativistic ion-atom collisions.

Chapter 6

The Experimental Environment

The RR and REC experiments recently carried out at GSI became possible due to the latest achievements in producing and storing of highly-charged heavy ions at GSI SchwerIonen Synchrotron SIS and the Experimental Storage Ring ESR, respectively. Accelerating and storing of the highly charged ions with a brilliant beam condition constitutes an important step towards precise REC studies.

The GSI accelerator facility consists of the UNILAC linear accelerator, where low-charge ions get pre-accelerated to an energy of 11.4 MeV/u and stripped to a charge state of 73+ by means of a thick carbon stripper foil. This charge state is magnetically separated and directed towards the heavy-ion synchrotron SIS. In the SIS, the ions are subject to a further acceleration of up to 1 GeV/u. To produce bare uranium ions which have $\approx$ 130 KeV K-shell binding energy, a beam energy at least 300 MeV/u is required. The production of the bare species is finally accomplished via extraction of the ions out of the SIS and an injection into the transfer line towards the experimental installations. In the transfer line the ions pass through a thick Cu stripper foils. From the emerging charge state distributions, the fraction of bare ions is magnetically separated.

6.1 The Experimental Storage Ring ESR

A unique part of GSI accelerator facility is the ESR storage ring [121], see figure 6.2. The circumference of the ESR amounts to 108 m and its magnetic rigidity to 10 Tm, respectively. The injected hot ion beam with a typical emit-

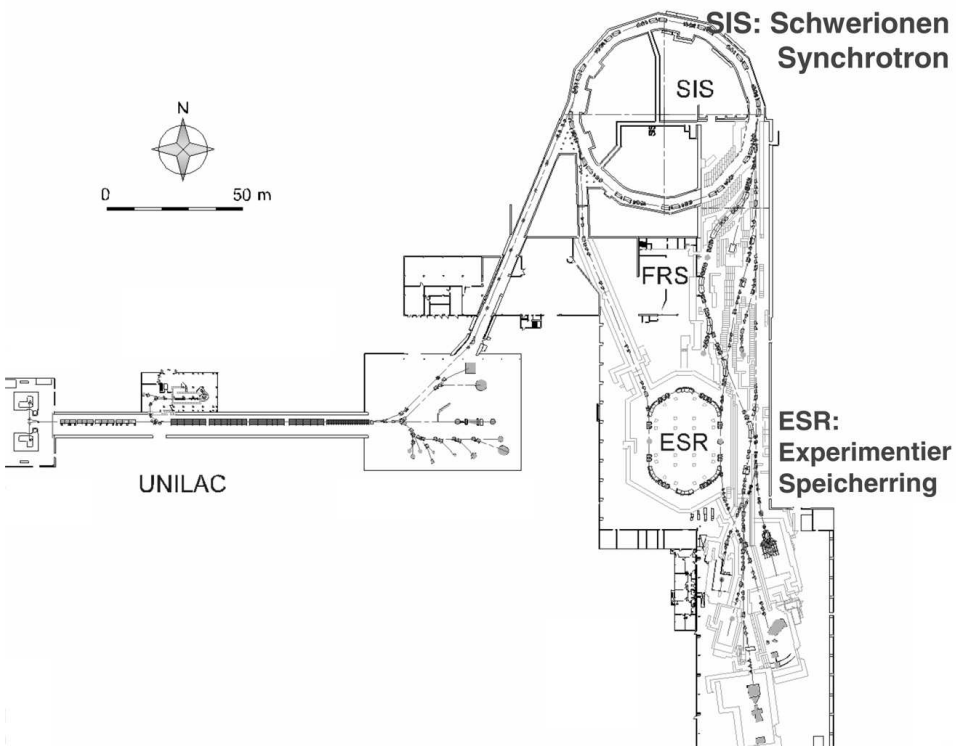

Figure 6.1: Layout of the accelerator facility at GSI, the linear accelerator UNILAC, the heavy-ion synchrotron SIS18, and the experimental storage ring ESR.

tance of about 5 π mm mrad is very efficiently cooled by Coulomb interaction in the electron cooler, see figure 6.3. For efficient cooling of higher energy beams, a stochastic cooling is also applied at the ESR [122]. The cooling of the beam reduces the emittance to 0.1 π mm mrad or less and provides beam diameters of less than 5 mm. This factor is in particular important for precise measurements at the jet target, where a control over geometrical factors and possible Doppler corrections is required. The relative longitudinal momentum spread of the injected ion beam after cooling is reduced from $\Delta p/p \approx 10^{-3}$ to about 10^{-5}. For a detailed discussion of the electron cooling technique see [120]. In particular, electron cooling guarantees for a well defined constant beam velocity which is generally of the order of $\Delta\beta/\beta \approx 10^{-4}$. A typical Schottky frequency spectrum of uncooled ion beam in comparison with the cooled one is shown in figure 6.4.

Another important parameter of the ESR is a maximum number of the stored particles. For uranium up to 10^8 ions can be stored routinely. This number is

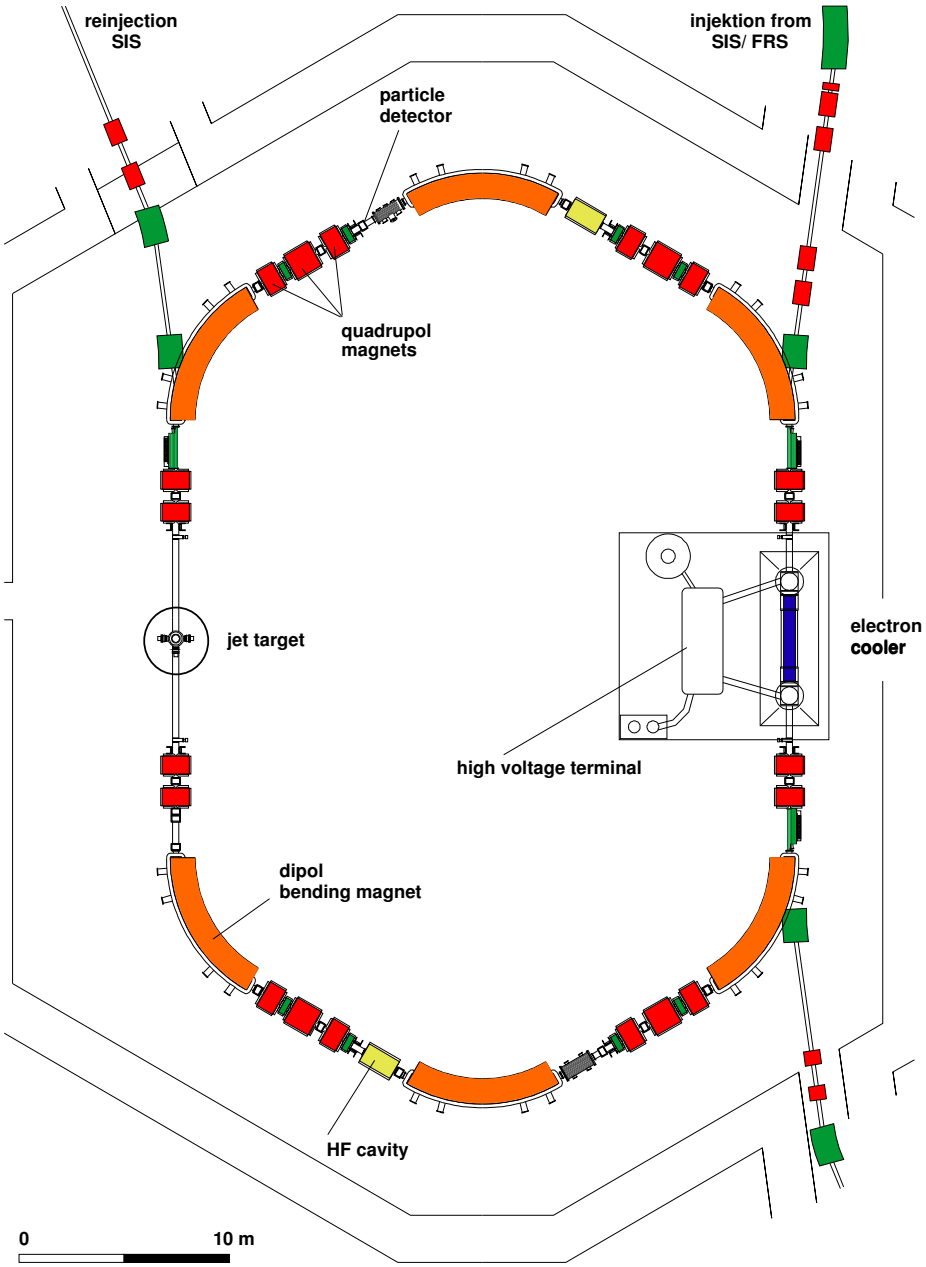

Figure 6.2: Schematic presentation of the storage and cooler ring ESR at GSI-Darmstadt. The layout depicts the beam guiding system (dipole bending magnets, quadrupoles and hexapoles) as well as the most important installations for beam handling and diagnostics (kicker, rf cavities, Schottky noise pick up, electron cooler). The position of the internal jet-target is marked in addition.

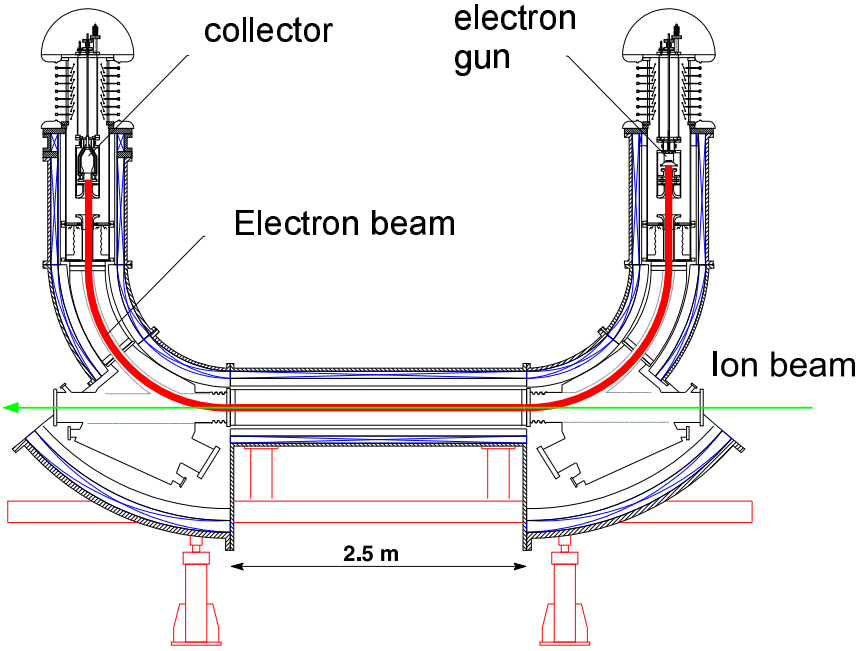

Figure 6.3: Layout of the electron cooler device used at the storage and cooler ring ESR. Electrons produced in the electron gun at a cathode temperature of ≈ 1300 K are guided by a ≈0.1 T magnetic field co-propagating over a distance of 2 m with the stored ion beam [120].

still below the upper limit of particles which can be stored in principle. These limits are due to the space charge potential of the stored ion beams and restrict the number of stored ions e.g. for the case of bare uranium at 556 MeV/u to 9.3×10^9 and at 50 MeV/u to 4.4×10^8, respectively [123, 1].

In order to investigate REC in a low energy domain, another unique feature of the ESR namely the deceleration capability can be used [5]. For this purpose, the electron cooler is switched off the coasting beam is rebunched and decelerated while simultaneously ramping down the magnetic fields. At the final stage of beam handling, the electron cooler is switched on again. For the case of bare uranium ions the lowest beam energy achieved by this procedure is close to 10 MeV/u, [124].

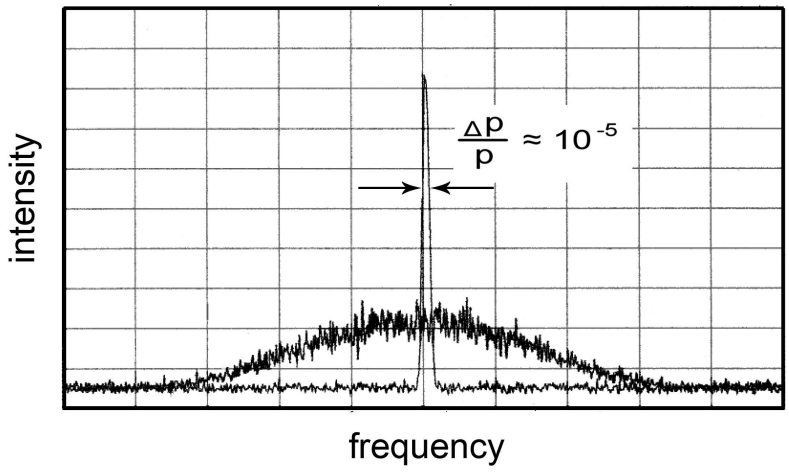

Figure 6.4: Schottky frequency spectrum for a circulating beam of U^{92+} ions at 295 MeV/u. The broad distribution refers to the non-cooled beam, measured directly after injection into the ESR. The narrow distribution reflects the momentum profile of a continuously cooled ion beam [125].

6.2 Experiments at the internal jet-target of the ESR

The basic principle of charge exchange experiments at the ESR gas-jet target is shown on figure 6.5, where ions after an electron capture or an ionization are deflected by a ring dipole magnet to particle detectors. For this purpose Multi-Wire Proportional Counters (MWPC) are available which allow one to measure accurately the position of the up- or down-charged ions on the detector [126] with a detection efficiency of close to 100%.

In fig. 6.6 a schematic graph of the gasjet is shown [127]. The jet is produced by expanding a gas through a Laval nozzle of 0.1 mm in diameter. To meet the ultrahigh vacuum (UHV) requirements of the ESR ($\approx 10^{-11}$ mbar), the actual set-up consists of an injection and a dump part, both separated by skimmers in four stages of a differential pumping system. The present target concept can be described as *the creation of a supersonic jet with a large number of well defined small clusters* [127]. For a detailed description of the target set-up and design we refer to [127] and [128].

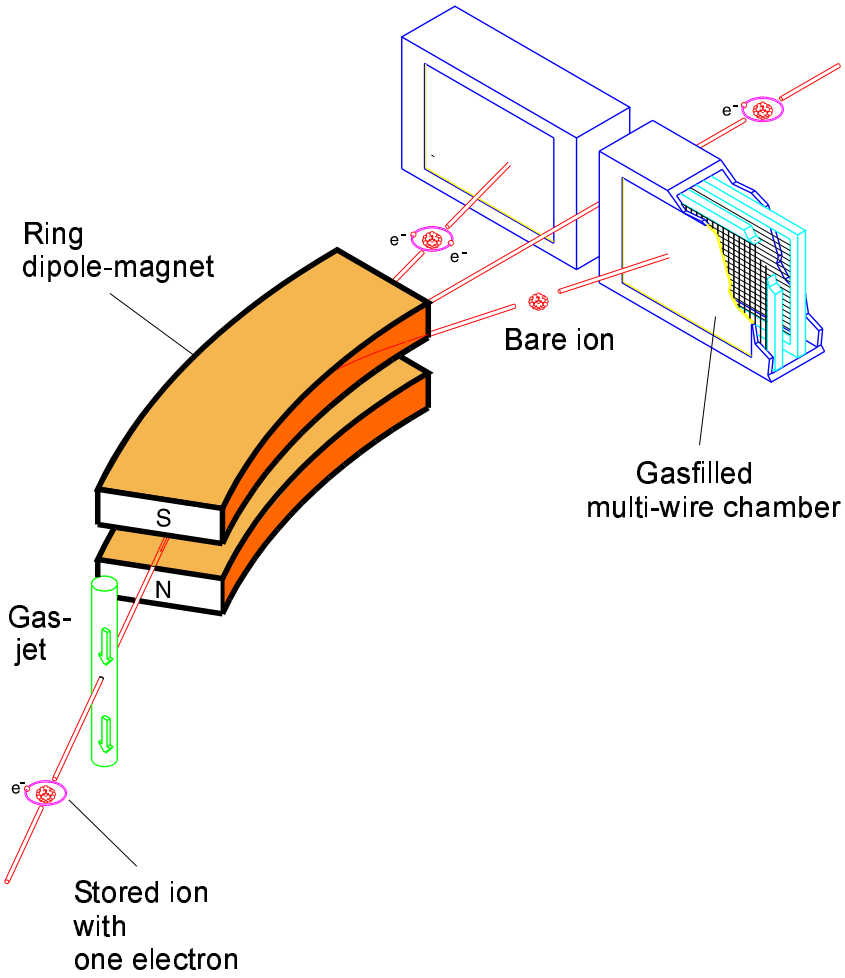

Figure 6.5: Principle of charge-exchange experiments at the internal jet target of the ESR storage ring illustrated for the case of stored H-like ions. The primary beam of stored ions at charge-state Q crosses a perpendicularly oriented molecular or atomic supersonic gas beam. The ring dipole magnet serves as a magnetic spectrometer for changes of the magnetic regidity, here electron capture (Q-1) and ionization Q.

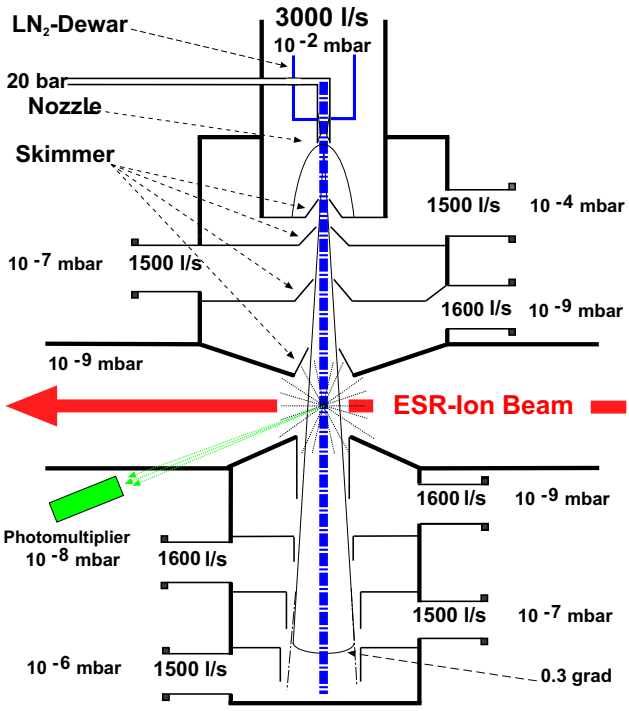

Figure 6.6: Schematic graph of the ESR internal target [127].

The typical gasjet target density amounts to about 10^{12} particle/cm^2 [127]. Target gases currently available are: H_2, N_2, CH_4, Ar, Kr and Xe. For the expensive noble gases such as krypton or xenon, a recycling system is used. The diameter of the target was measured experimentally by scanning the jet profile via low intense ion beams (small ion beam diameter), and is about 5 mm.

6.3 REC studies at the Internal Target

The gas jet experimental chamber is essentially designed to study X-Ray emissions at different observation angles. The accessible angles are ≈4°, 35°, 60°, 90°, 120°, and 150°, [15], see figure 6.7 for comparison [129]. All detectors are separated from the UHV system of the ESR either by 50 μm thick stainless steal (≈4°, 60°, and 120°) or by 100 μm thick Be windows.

For the particular case of stored bare uranium ions, a sample x-ray spectrum associated with electron capture is displayed in Fig. 6.8 [129]. This spectrum was

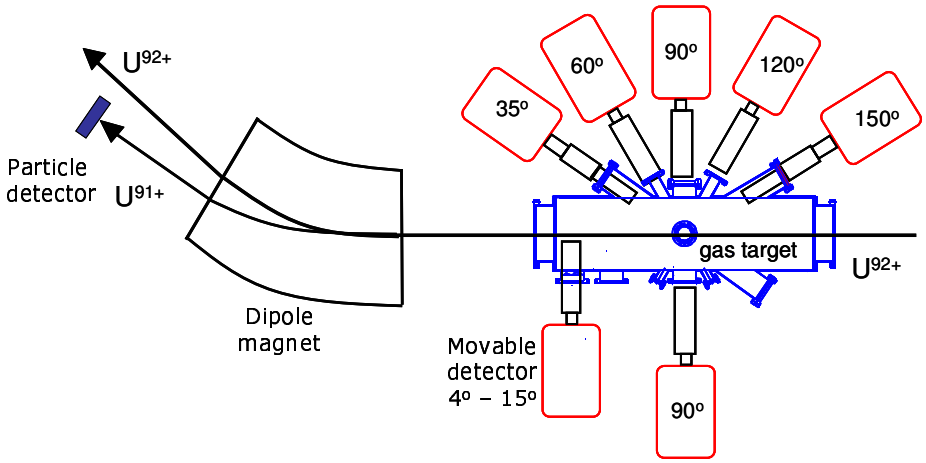

Figure 6.7: Layout of the experimental arrangement at the internal jet-target. X-ray detectors view the target interaction zone at observation angles of ≈4°, 35°, 60°, 90°, 120°, and 150°. All detectors are separated from the UHV system of the storage ring either by 50 μm thick stainless steal (≈4°, 60°, and 120°) or by 100 μm thick Be windows. Photon emission is observed in coincidence with the down-charged ions, detected in the particle counter located behind the dipole magnet. The photon detector close to 0° is mounted on a movable support.

obtained at an observation angle of 150° for 310 MeV/u $U^{92+}\rightarrow N_2$ collisions. Beside the Lyman ground-state transitions (Lyα_1: $2p_{3/2}\rightarrow 1s_{1/2}$, Ly$\alpha_2$: $2p_{1/2}\rightarrow 1s_{1/2}$, M1: $2s_{1/2}\rightarrow 1s_{1/2}$) the most prominent features observed in the spectrum are due to radiative electron capture into the ground and excited projectile states. The width of these lines reflects the Compton profile of the bound target electrons (see e.g. [130]).

The possibility to study photon emission close to 0° is an important feature of the current scattering chamber at the ESR jet target. For this purpose an intrinsic germanium detector is mounted on a movable support, 510 mm down-stream from the projectile-target interaction region. Periodically, after the injection of the ions from the SIS into the ESR and having achieved a cold ion beam, the photon as well as the particle detectors can be placed at their measurement positions. For the photon detector, the latter corresponds to a distance of only 1 cm from the circulating beam. This angle was used to identify magnetic spin-flip transitions for the K-REC process as it is discussed in the chapter 5.2.

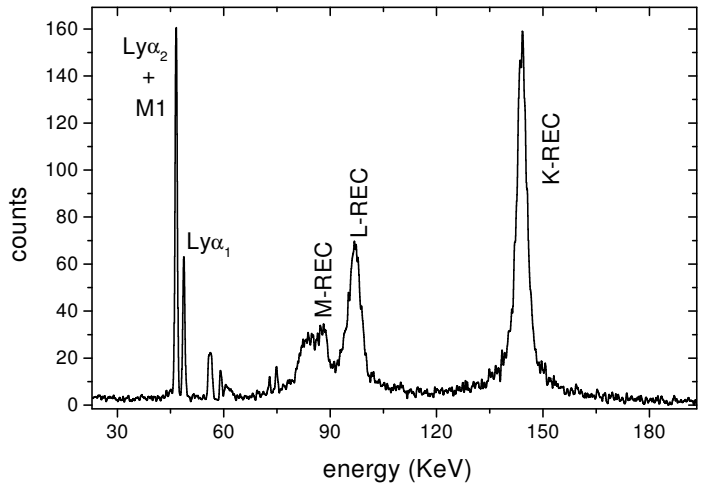

Figure 6.8: X-ray spectrum observed at nearly 150° for $U^{92+} \rightarrow N_2$ collisions at 310 MeV/u [15]. The data were taken in coincidence with down-charged U^{91+} ions.

6.3.1 REC line shape analysis

Figure 6.9 shows a fit of the theoretically calculated REC energy distribution to the experimental data. The theoretical double differential cross sections are derived from exact cross sections for radiative recombination by adopting the impulse approximation and the momentum distribution of the target electrons (Compton profile). The momentum distributions are obtained by Fourier transforming appropriate Roothaan-Hartree-Fock wave functions [101, 131]. On the figure one can see a good agreement between the theoretical and the experimental results.

Whereas the findings given above confirm the theoretical doubly-differential REC cross-sections we like to emphasize that, for practical reasons, it is appropriate to neglect the transverse electron momentum for the description of the Compton profile since the corrections introduced are rather small. For example, to obtain the differential cross-section values for REC into the K-shell and into the excited states, the following fit formula was applied for the line-shape analysis of the measured REC spectral distributions [13]:

$$\frac{d^2\sigma}{d\Omega' d\hbar\omega'} = \sum_j c_j \left[\frac{1}{\gamma\beta c} \sum_i \int dq_z J_i(q_z) \frac{d\sigma_j}{d\Omega'} \delta_j \right], \tag{6.1}$$

where the primed variables denote the projectile frame and the unprimed ones the

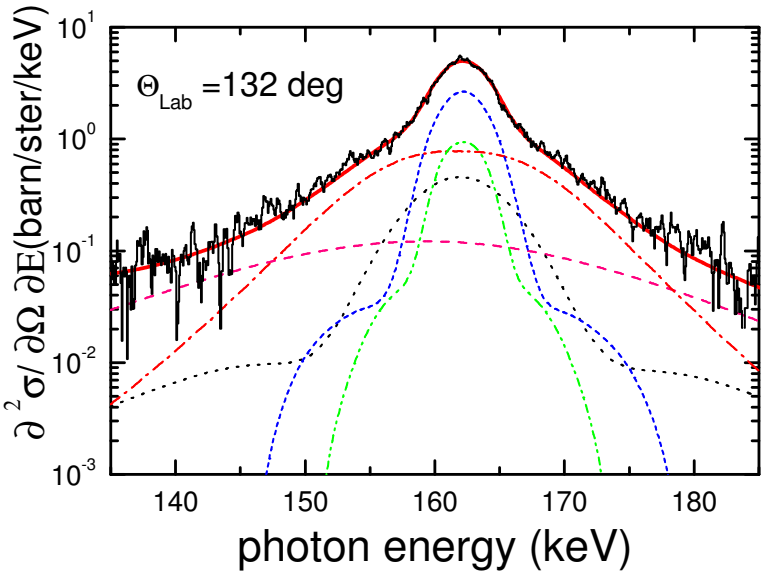

Figure 6.9: Theoretical doubly differential REC photon cross sections (solid line) for 358 MeV/u U^{92+} → Ar collisions in comparison with the experimental data. Individual contributions of the Compton profiles of the various shells of the Ar target are given separately 1s: (— — —); 2s: (· · ·); 2p: (· — ·); 3s: (— · · —); 3p:(· - ·). From [130].

target frame. Furthermore, J_i is the Compton profile of the electron in the initial target orbital i, while q_z is the projection of the electron momentum onto the beam axis, and the quantities c_j are fitting parameters. Following the description of Kleber et al. [132], the quantity in the square brackets of Eq. 6.1 represents the double differential cross section for REC into a specific projectile substate j. For the differential cross section $d\sigma_j^{\mathrm{REC}}/d\Omega'$ one may apply the prescription of the dipole approximation [95], which is known to reproduce the energy dependence of REC. In addition, for the Compton profiles, the tabulated values of Biggs et al. [133] were used. Finally, the results must be transformed to the laboratory frame. Using a χ^2 minimizing routine, this method turned out to be well suited for determining differential REC cross-section from measured x-ray spectra, i.e. doubly differential cross-section data [13].

Chapter 7

The measurement of the K-REC polarization

The first experimental linear polarization study for the radiation of the Radiative Electron Capture was performed in October 2002 at the Gas-jet target of the ESR storage ring at GSI Darmstadt. For the experiment a bare uranium ion beam was used.

For the experiment bare uranium ions extracted out of the SIS were injected into the ESR at an energy of 400 MeV/u. Directly after the injection from the SIS the ions were cooled at the high energy. The cooler current and voltage applied were about 100 mA and 213.5 kV respectively. As it was already mentioned above, electron cooling guarantees a well defined constant beam velocity, generally of the order of $\Delta\beta/\beta \approx 10^{-5}$ as well as a reduction of the beam emittance. The accumulated ion currents in the ESR were about 1-2 mA, corresponding to about 1 to $3 \cdot 10^8$ stored ions. In order to exclude the data which might have been influenced by the complicated beam-handling procedures during injection and deceleration, no x-ray spectra were recorded during the beam accumulation periods. Only after the completion of a whole cycle, the gas-jet was switched on and the measurement was started. The N_2 gas was used as a target at an areal density of $\rho \approx 1 \div 3 \times 10^{12}\ \frac{particle}{cm^2}$. The measuring time per cycle was limited by the capture rate in the gas-jet target to typically few minutes.

The Pixel Detector was mounted in series at observation angles of 90° and 60° angles relative to the ion beam, see figure 6.7. The measurement was conducted

for different ion energies. For this a deceleration capability of the ESR was used. In this case directly after the injection from the SIS (before the deceleration) the ions were first cooled at the high energy, then electron cooling was switched off, the coasting beam was bunched and the deceleration mode was applied. At the low energy the electron cooling was repeated. Table 7.1 summarizes the main ESR adjustments for each decelerated ion beam energy. For each energy and detector position the measurement took approximately 2 days.

Ion Beam Energy, MeV/u	Electron Cooler Voltage, KeV/u	Electron Cooler current mA	Pixel Detector Position
400.0	213.5	100	90°, 60°
98.4	54.0	100	60°
132.2	72.5	50	60°
190.0	103.8	50	60°

Table 7.1: The ESR adjustments for each energy of the ion beam.

X-rays emitted via Radiative Electron Capture in the gas-jet target were detected by a segmented planar germanium *Pixel Detector* consisting out of 16 individual pixels, arranged in a 4x4 pixel matrix. The X-rays were recorded in coincidence with down-charged uranium ions, as produced by capture of one electron from the gas-jet target. The down-charged ions were registered in a gas-filled multiwire proportional counter (MWPC) which was installed in a pocket behind the first dipole magnet downstream of the gas-jet target (compare the principle of the charge exchange experiments at the ESR as displayed in Figure 6.5 and the experimental arrangement at the gas-jet target as shown in Figure 6.7). During the periods of beam accumulation, the detector was pulled out of the beam pipe for the beam injection. Before the start of the measurement, the detector was moved to such a position that down-charged particles could be detected without disturbing the orbit of bare projectiles.

The Pixel Detector was fabricated in Forschung Zentrum Jülich by D. Protic and co-workers, it is shown on Picture 7.1. The high purity Ge crystal has a planar geometry and it is segmented with 4x4 pixel matrix on a front side. Each pixel has 7x7 mm size, see Figure 7.2a. The back side of the detector has a single

Figure 7.1: The Pixel Detector. The detector was fabricated in Forschung Zentrum Jülich by D. Protic.

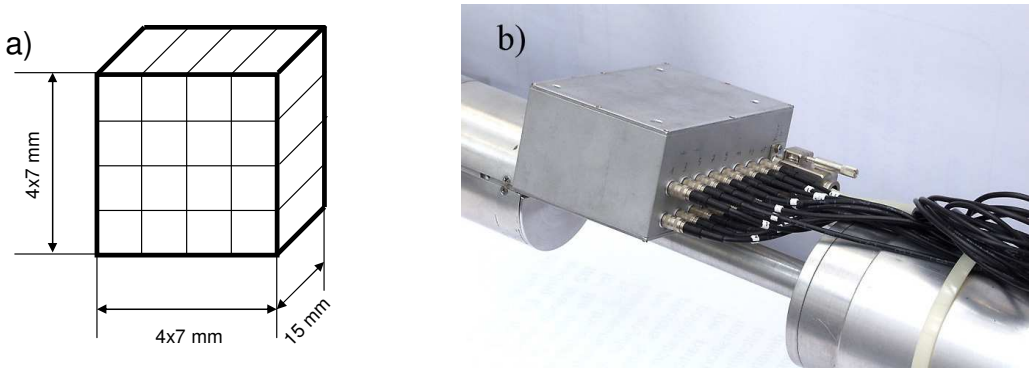

Figure 7.2: a) Schematic view of the detector crystal segmentation. b) View of the 16-channel preamplifier box. Each channel of the preamplifier is connected to a single pixel.

21x21 mm anode. The anode output is equipped with an internal precooled preamplifier. The pixel signals are preamplified in an external preamplifier box, connected directly to the detector housing in order to reduce a possible noise, see Figure 7.2b. The front side of the detector is equipped with an aluminum window of a thickness of ≈ 1 mm.

At the angle of 90° the detector was mounted at the distance of 256 mm from the gas-jet target behind a 100 μm thick Be window. At the angle of 60° the distance from the gas-jet target was 340 mm and a 50 μm thick stainless steel window was used.

The time resolution of the detector with the planar geometry can be as good as 20 ns. But in the particular experimental case the resolution depends strongly on the preamplifier used together with the detector, the adjustments of the *constant fraction discriminators* and the fast *timing filter amplifiers*. Moreover, the timing value were measured relative to the particle detector. The obtained resolution of the detector timing, relative to the particle detector signal, was 50 ns.

The limitation for the energy resolution was the resolution of preamplifiers. The used FET's are not precooled. The energy resolution in experimental environments depends also on the noise conditions of the power supplies, background, and other devices, working in the neighboring area. The obtained energy resolution for the Pixel Detector was of the order of 2 KeV, close to the specification values.

Figure 7.3 shows the principle of the polarization studies at the ESR jet-target. The Pixel Detector observes the K-REC X-rays emitted at the gas target. Compton coincident events inside the detector were analyzed in order to extract the information about the X-ray polarization. Figure 7.4 shows a coincident Compton scattering spectrum observed with the Pixel Detector in comparison with a single pixel spectrum. The measured intensity of the Compton scattering in the vertical direction exceeds the intensity in the horizontal direction, which is an unambiguous signature of the strong polarization of the REC radiation.

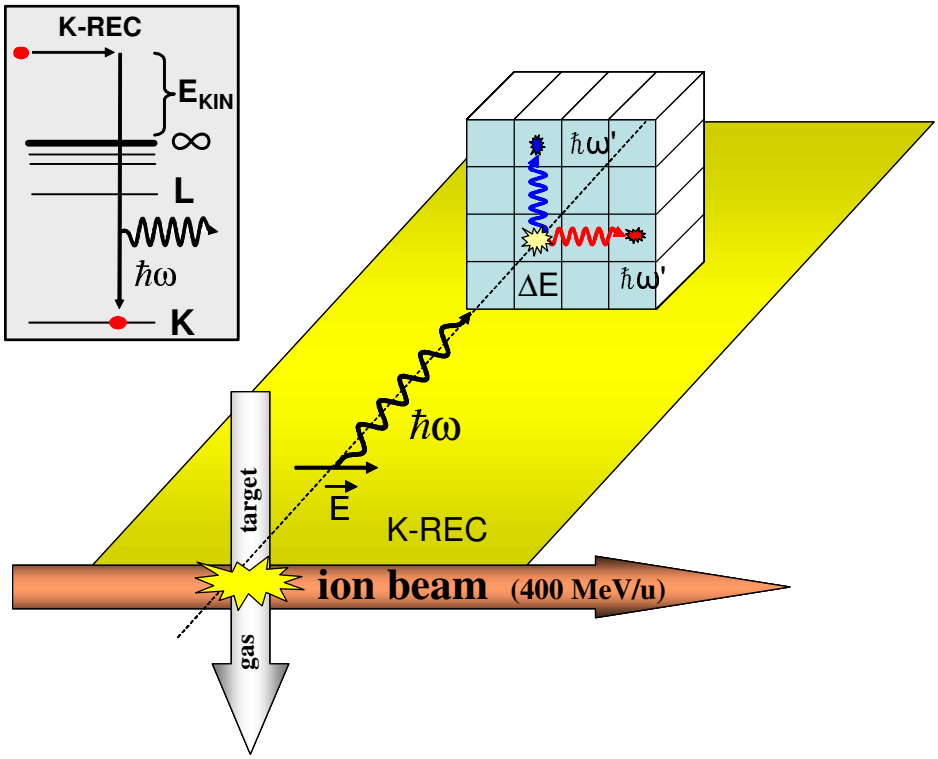

Figure 7.3: Principle of the REC polarization study with the Pixel Detector at the ESR jet-target: analysis of the Compton scattering intensities in different directions inside the detector.

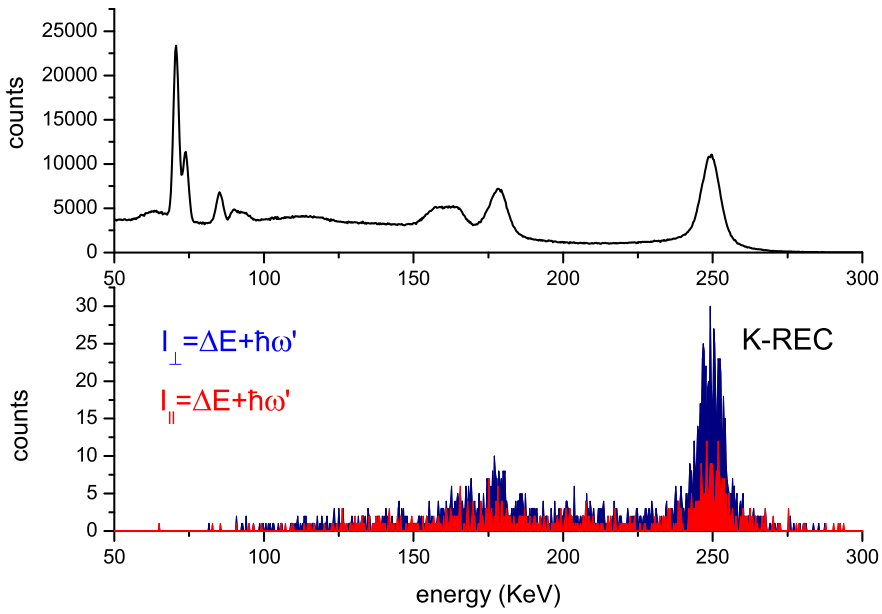

Figure 7.4: The typical spectrum of one pixel observed in the experiment (upper plot). The plot of the coincident Compton spectra (electron recoil energy + scattered photon energy) for the scattering in vertical and horizontal directions (lower plot).

Chapter 8

Data analysis: Compton polarimetry in application to the pixel detector

8.1 X-ray spectra

In figure 8.1 a typical calibrated single pixel X-ray spectrum obtained from the Pixel detector is displayed. This particular spectrum was measured at an observation angle of 90° at the gas jet target section of the ESR storage ring. N_2 gas was used as a target. The bare uranium ions where stored and cooled at energy of 400 Mev/u. The spectrum was recorded in coincidence with down-charged ions. See figure 8.2 for the X-ray - particle coincidences time spectrum. The filled curve in figure 8.1 represents the background spectrum. One can see that in the energy region of the K-REC line the background is almost zero. The coincidence technique allows for an efficient suppression of background arising from different sources: e.g. bremsstrahlung and cosmic radiation.

The spectrum structure represents two major processes occurring in ion-atom collisions: Radiative Electron Capture (REC) and bound to bound transitions in H-like uranium. The K-REC (K shell REC), L-REC and M- and higher shells REC are resolved in the spectrum. The large widths of these lines are due to the fact that the electron is captured from a bound states of N_2 with different momenta (Compton Profile) and therefore different relative velocities to the bare

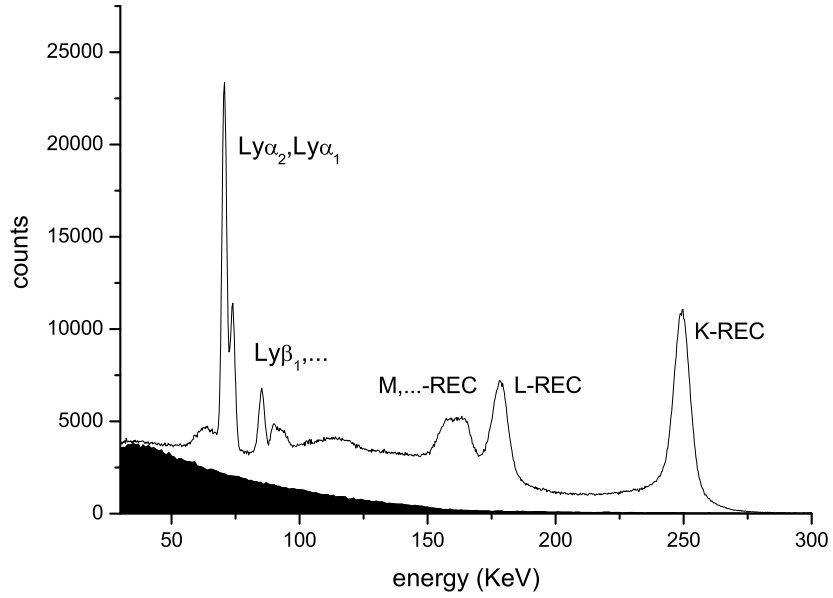

Figure 8.1: X-ray spectrum for H-like uranium, stored at 400Mev/u energy as observed by Pixel detector, mounted on 90° at supersonic gas jet target of the storage ring ERS. The spectrum was measured in coincidence with down-charged uranium ions. The filled curve represents measured random events, rising from the bremsstrahlung and used for the background substraction.

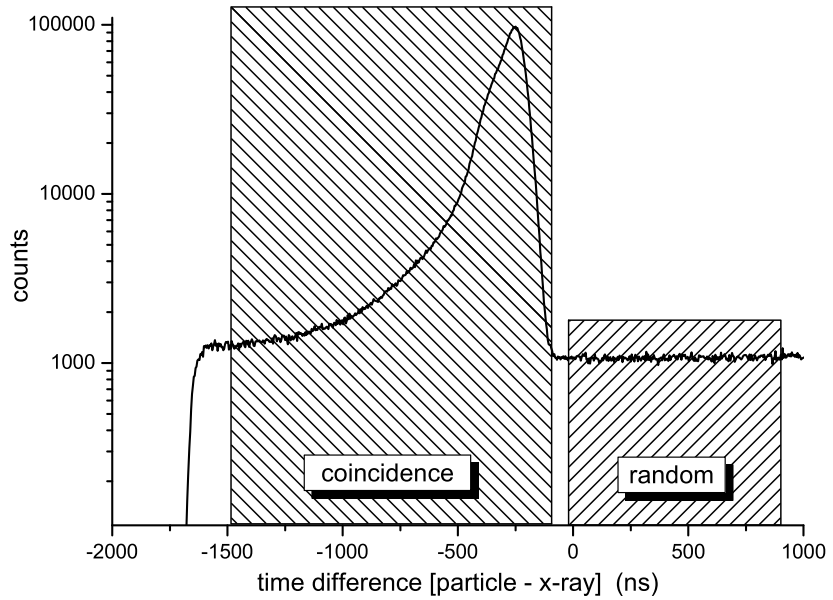

Figure 8.2: Coincidence time spectrum between a multichannel plate particle detector, mounted at the position to detect down-charged ions and Pixel detector.

uranium ions, see chapter 6.3.1.

The capture into the L and higher shells is followed by ground state transitions for instance the most prominent $Ly\alpha_1$ ($2p_{3/2} \rightarrow 1s_{1/2}$) and $Ly\alpha_2$ ($2s_{1/2} \rightarrow 1s_{1/2}$ and $2p_{1/2} \rightarrow 1s_{1/2}$) radiation. The detector energy resolution is sufficient to separate these two lines.

A bump in the spectrum at an energy of ≈63 KeV near the $Ly\alpha_2$ is due to the Compton scattering of the $Ly\alpha_2$ and $Ly\alpha_1$ photons inside the aluminium window in front of the Germanium crystal. The scattered photons with forwarded scattering directions are absorbed in the detector. The forwarded scattering direction leads to a small energy deposition inside the aluminium window as scattered electrons.

A bump at an energy of ≈115 KeV is the Compton edge of the K-REC line. This feature has a wide energy distribution due to the wide angular distribution of the scattered photons and the large width of the K-REC line, see figure 2.7.

As far as the detector was mounted at the distance of 256 mm from the gas target and has a 21 mm width, each pixel of the detector has an individual observation angle θ which leads to an individual Doppler shift. See figure 8.3 for comparison. A possibility of the Doppler shift correction is a very important feature of the segmented detectors. It can play a significant role in a precision spectroscopy where a big detection efficiency is also required, which can be provided only by increasing the crystal size [24].

8.2 Compton scattering

8.2.1 Pixel to pixel coincidences

Compton events inside the detector where the recoil electron and the Compton photon deposit energies in different pixels can be detected using a coincidence technique. The Compton recoil electron deposits the energy in the same pixel where Compton scattering occurs, see figure 2.9. For electron energies less than 200 KeV the mean electron path length inside the germanium crystal is below 0.15 mm. For a particular X-ray line the sum energy of the scattered electron ($\hbar\omega'$) an outgoing scattered photon (ΔE) is constant and refers to the energy of

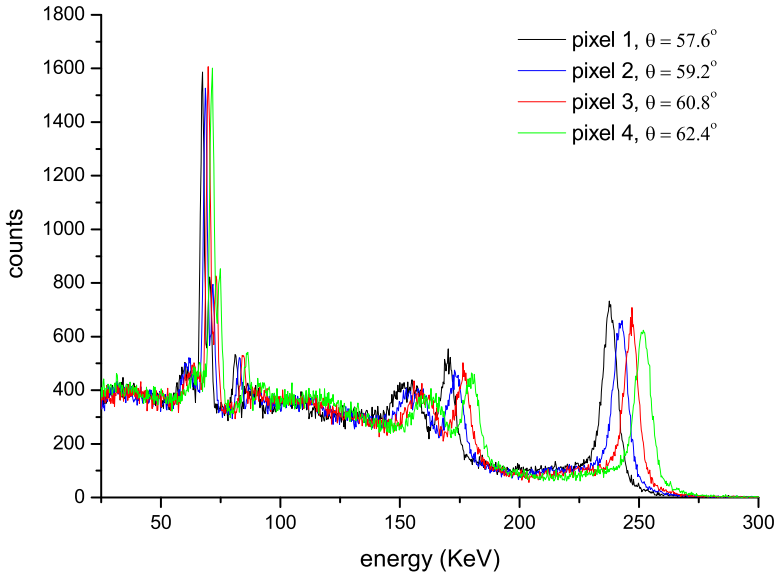

Figure 8.3: X-ray spectra of the individual pixels feature the Doppler shift depending on the observation angle θ of each pixel, see Eq. 4.4.

the incoming photon ($E = \Delta E + \hbar\omega'$).

8.2.2 Compton scattering kinematics

In figure 8.4 one can see a scattering plot of the coincident energy deposition in one pixel versus the energy deposition in another one with a condition that only 2 pixels have triggered at the same time. The broad diagonal lines represent events where the sum energy is constant. For the energies of the incoming photons less than $mc^2/2 \approx 256\ KeV$, the electron energy deposition (2.4) is always smaller than the photon energy deposition, see chapter 2.2. Therefore by applying the energy condition of $\Delta E < \hbar\omega'$ one can identify the pixel where Compton scattering took place (a pixel where the reloil electron was stopped and deposited its energy). In this case the upper part of the line in the figure 8.4a represents scattering from pixel 1 to pixel 2, and the lower part represents scattering from pixel 2 to pixel 1. In contrast, in figure 8.4b, a scatter plot is displayed recorded at 60° for $U^{92+} \rightarrow N_2$ collisions. In this case the condition $E_{K-REC} < mc^2/2$ is

no longer valid and as a consequence, the energies of the Compton photon and the recoil electron can no longer be separated unambiguously.

It is important to note, that for smaller incoming photon energies the separation between electron end photon energy depositions is unambiguous. See lower energy parts (L-REC, M-REC lines) on figure 8.4 for comparison. For energie of the incoming photons $\approx$ 60 KeV, the maximum electron energy which depends on the scattering angle is equal to $\approx$ 6.3 KeV, which is near to the electronic threshold used in the experiment. The electronic threshold limits the ability to detect Compton scattering events and therefore it decreases the efficiency of the detector as a polarimeter (see chapter 3.1.2).

Knowing the Compton photon and the recoil electron energies one can deduce the scattering angle θ, see Equation 8.1. For real Compton scattering events with correctly measured electron and photon energies $\cos\theta$ must be consistent with the scattering geometry. Each scattering direction, which is represented by a pair of pixels, has different limits for the angle θ:

$$\cos\theta = 1 - mc^2\left(\frac{1}{\hbar\omega'} - \frac{1}{\Delta E + \hbar\omega'}\right) . \tag{8.1}$$

Figure 8.5 shows boundaries for the Kinematic Event Selection (see chapter 3.1.2). The area between the lines $\cos\theta = -1$ and $\cos\theta = 1$ represents the general condition for the Kinematic Event Selection. Events outside this boundaries do not represent Compton scattering. They are due to a background arising from different sources. The upper boundary curve arises from the fact that the electron energy deposition has a minimum threshold, which for this case is equal to 20 KeV. This is a software threshold required to cut a low energy noise. The lower boundary curve represents the accumulation condition that the lower energy deposition corresponds to the recoil electron and the higher to the Compton photon. It is always true for the energy of the incoming photons less than $mc^2/2 \approx$ 256 KeV.

For the incoming photon energies higher than $mc^2/2$ the energy condition $E_{photon} > \Delta E$ in true only for forwarded scattering angles, see figure 2.3. An additional curve in the figure 8.5, starting from the energy $mc^2/2$ represents a lower boundary for the region, where the Compton photon and the recoil electron can be separated unambiguously and therefore the direction of the Compton

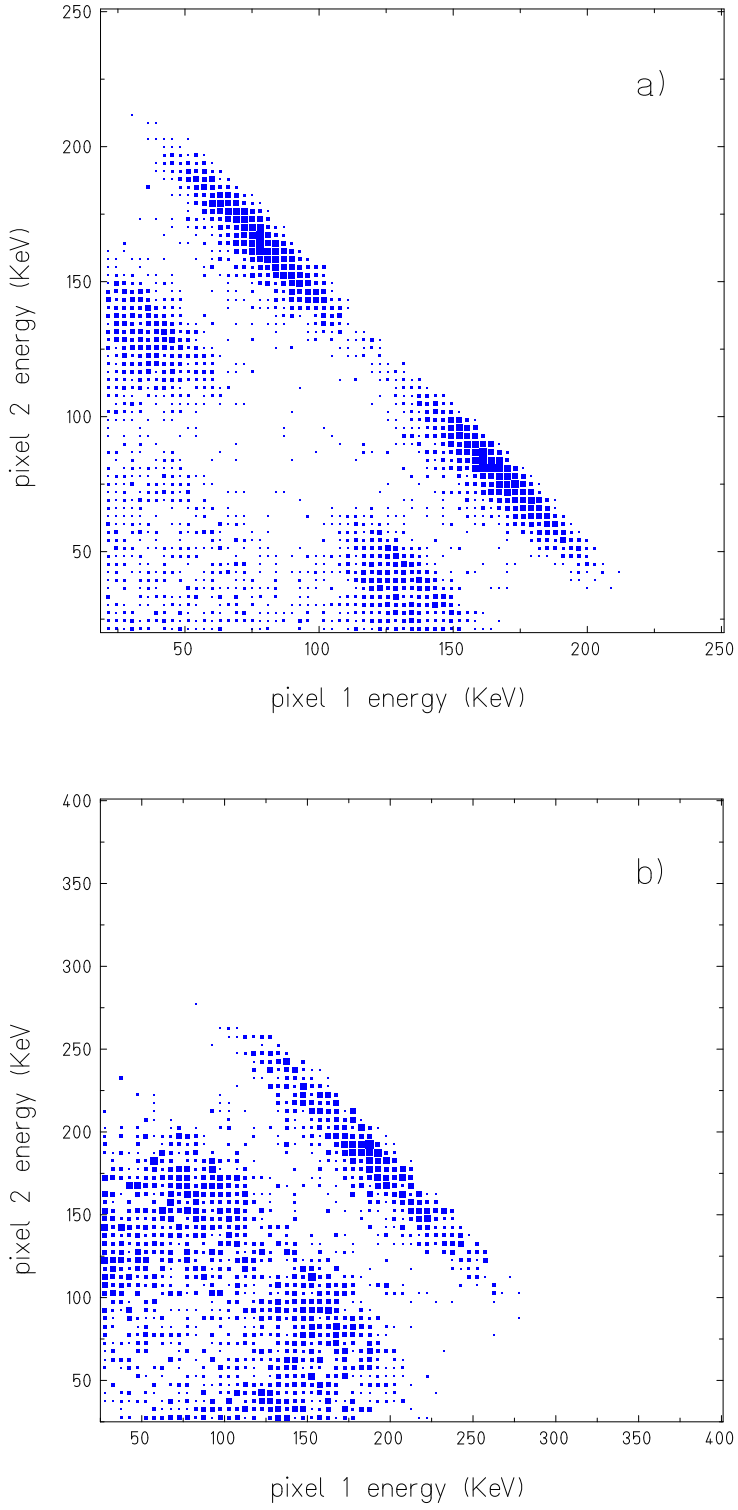

Figure 8.4: Compton scattering plot, an energy deposition in one pixel versus an energy deposition in another pixel for the photons emitted from the ion beam at an energy of 400 MeV. a) 90° observation angle in the laboratory frame, 248 KeV K-REC energy; b) 60° observation angle and 368 KeV K-REC energy.

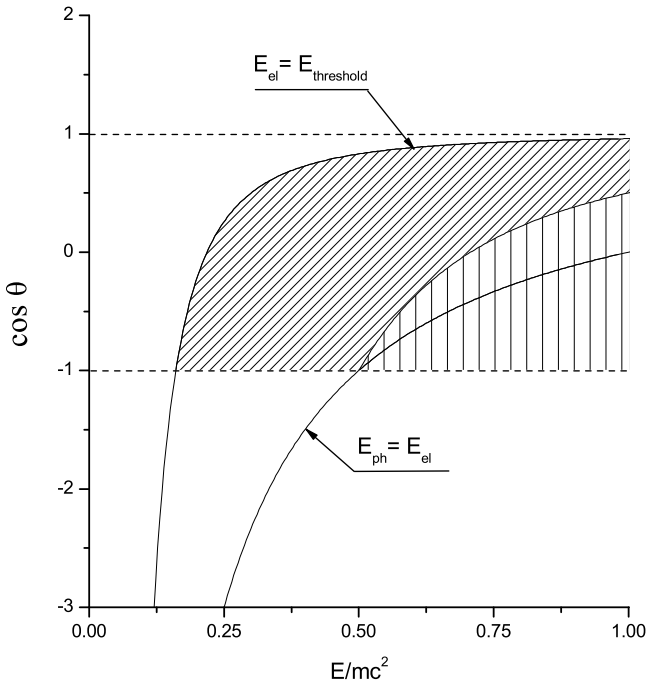

Figure 8.5: Boundaries for the Kinematic Event Selection in the case of 2D detector, where $\cos\theta$ is not measured directly. The dense filled area shows a region where only the energy condition $E_{ph} > E_{el}$ is required to separate scattered photons and electrons. The sparse filled area shows the region where scattered electrons and photons are not separated by the energy condition.

scattering can be determined.

Note, that a mistake in determining of the scattering direction leads to a mistake in the angle ϕ by 180° which is not crucial for the polarimetry purpose because of 180° symmetry of the scattering cross section described by the Klein-Nishina formula.

Typical, experimentally measured, energy distributions of $\cos\theta$, deduced by Eq. 8.1 are shown in figure 8.6. It is clearly seen that for the upper plot (400 MeV/u projectile energy, 90° observation angle) all events belonging to K-REC line are in the "safe" region, where the separation between electrons and photons is done by the energy condition. This also can be seen in figure 8.4.

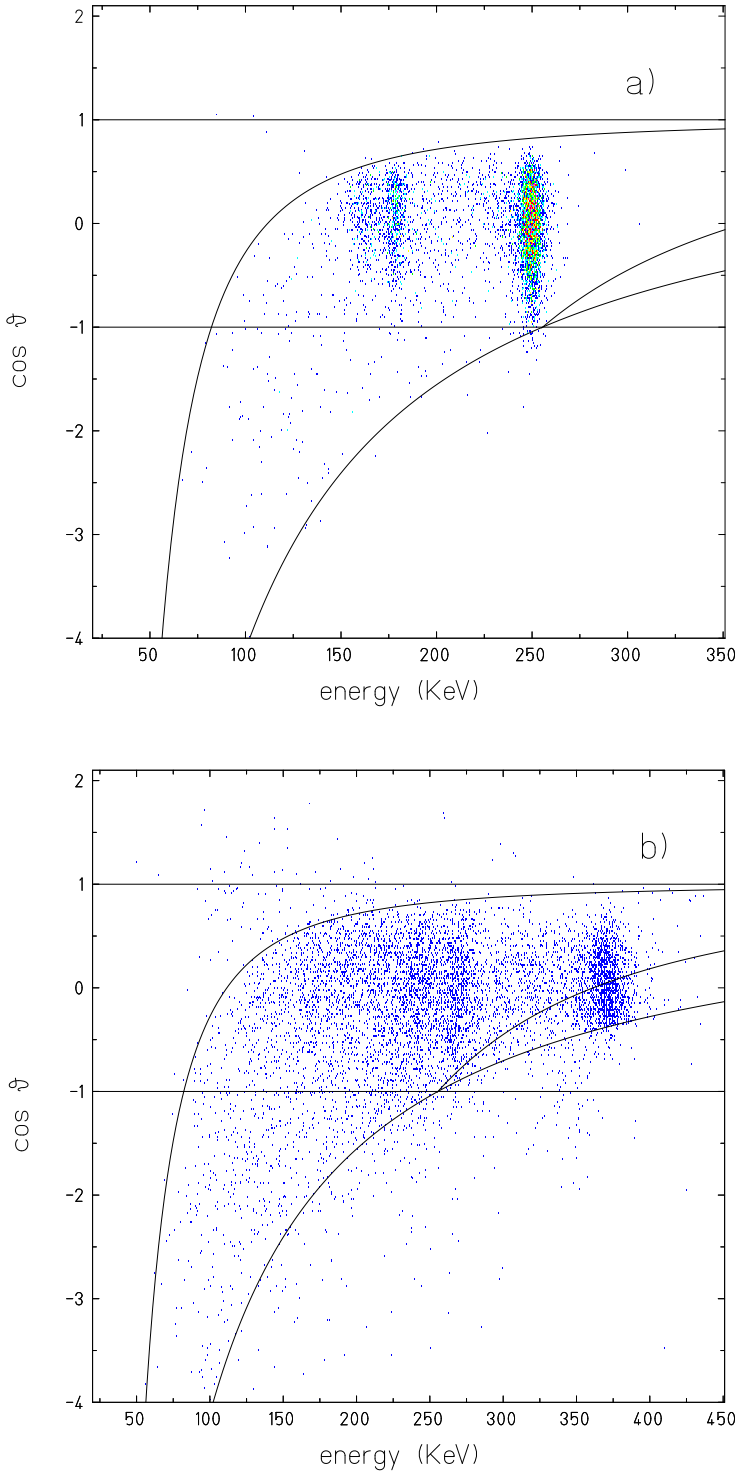

Figure 8.6: $\cos\theta$, deduced from the measured scattered electron and photon energies by the formula 8.1, plotted versus incoming photon energies. The spectrum was accumulated with a condition of $\Delta E < \hbar\omega^{'}$. Photons were emitted from the projectile at an energy of 400 MeV/u. a) 90° observation angle in the laboratory frame, 248 KeV K-REC energy; b) 60° observation angle and 368 KeV K-REC energy.

This is not true for the lower plot (400 MeV projectile energy, 60° observation angle) where the energy of the K-REC line is large enough and approximately half of the events are outside of the "safe" region and therefore the photons and the electrons are not identified by the energy condition. But as was said before it is not a problem for the polarimetry task, because of the 180° symmetry of the differential scattering cross section. The only inconvenience is that the Doppler correction is no longer possible for those events because of the unknown point of interaction. This results in an increased width of the K-REC line but does not affect the angular intensity distribution.

In figure 8.7b is a coincident sum spectrum for two pixels is displayed, accumulated with a condition of non-zero (above the threshold) energy deposition. Note that the events, contributing to the statistics of the coincident spectrum, contribute to background of the single pixel spectrum, see the chapter 8.1 and figures 2.7, 8.1. The presented method uses segmented detectors to utilize these events and to reconstruct the incoming photon energy.

As one can see in figure 8.7, the Compton coincident technique is insensitive to low energy photons E $<$ 60 KeV. This is due to the fact that the Compton cross section decreases with decreasing of energy.

The K-REC line is well resolved in the Compton coincident spectrum. The angular distribution of the Compton-scattered K-REC photons is analyzed in order to calculate the degree of linear polarization.

All possible scattering directions inside the 4x4 pixel detector are represented in a 7x7 scattering pattern, see figure 8.8. The scattering pattern represents a virtual 7x7 segmented polarimeter, where the central segment (3,3) serves as a Compton scatterer and other segments as photon absorbers. The statistics of all pairs of pixels representing the same relative geometry inside the Pixel Detector are combined in one pixel of the scattering pattern.

8.3 Scattering intensity distribution

Figure 8.9a shows a typical intensity distribution for the Compton scattering of the K-REC photons, obtained from the pixel detector. For same scattering angles, the statistics was summed up. The scattering intensity from one particular pixel

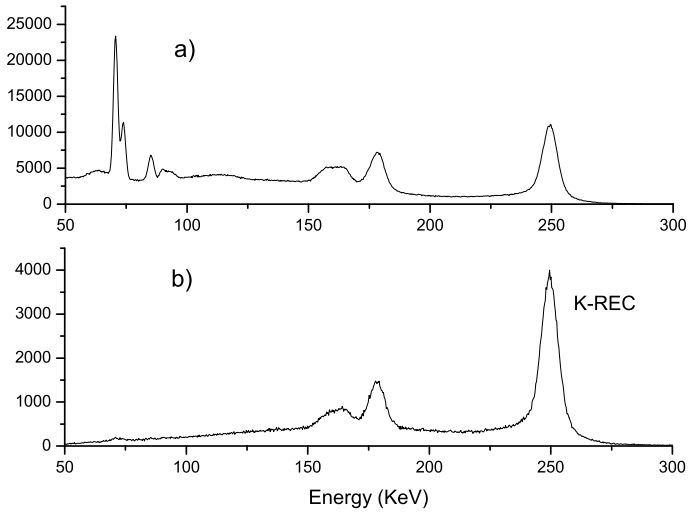

Figure 8.7: Lower plot represents a coincident pixel sum spectrum accumulated with a condition that only two pixels have triggered at the same time. On the upper plot a typical single pixel spectrum is shown for a comparison.

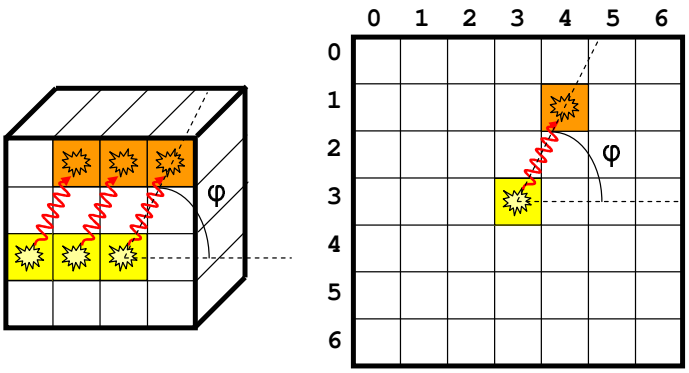

Figure 8.8: 7x7 scattering pattern represents all possible relative scattering geometries for the 4x4 pixel detector. Each pixel in the scattering pattern except pixel (3,3) which represents the scattering point, defines a direction for Compton scattering. The scattering angle φ is determined by the centers of the pixels. The finite pixel size introduces a finite distribution of the angle φ.

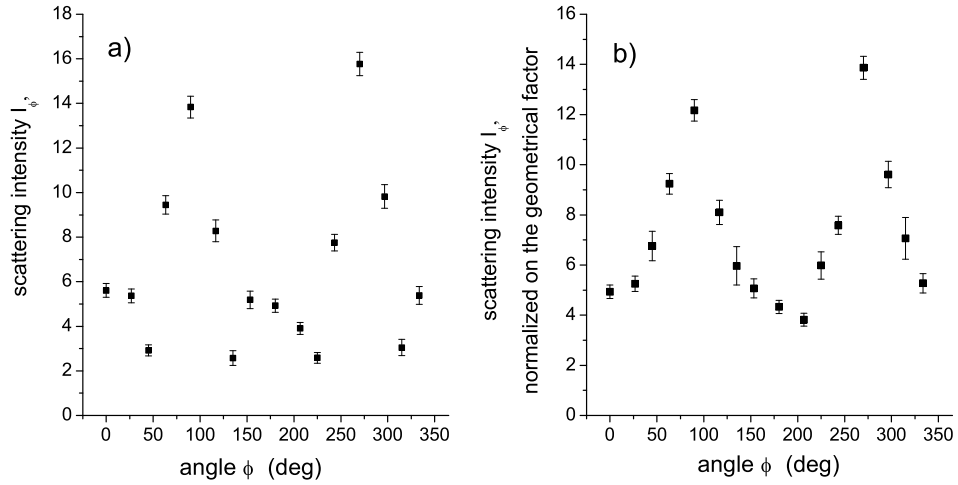

Figure 8.9: Measured intensity distribution for Compton scattering. a) Raw scattering intensity. b) Scattered intensity normalized to the solid angle of the pixel to which the scattering took place. Also the attenuation inside the Ge crystal has been considered.

("pixel 1") to another ("pixel 2") depends on the following factors:

1. efficiency of the pixel 1 as a Compton scatterer and of pixel 2 as a photon absorber;

2. solid angle of the pixel 2 with respect to the scattering point;

3. distance between the pixels and the energy dependent attenuation;

4. geometry (shape) of the pixels.

These factors have been taken into account in the numerical simulation program, used in order to calculate the detector response to polarized photon beams and to extract the degree of linear polarization from the measured data. Figure 8.9b shows the K-REC intensity distribution, normalized for the solid angle of the pixels and for photon absorption in-between the pixels.

8.3.1 Pixel efficiencies

The measured scattering intensity depends strongly on the detection efficiencies of the pixels. The determination of these efficiencies constitutes an important aspect for an accurate measurement of the Compton scattering angular distribution. Note that due to the extended geometry of the detector, the scattering intensity from a particular pixel depends also on the angle of the pixel with respect to the ion beam. The K-REC line has approximately the $\sin^2\theta$ angular distribution, where θ is the emission angle in the laboratory frame, see figure 4.3. For instance for the observation angle $\theta_0 = 60°$, the intensity difference between outermost pixels reaches 6%.

The pixel efficiencies can be deduced from the experimental data. The intensity of a particular line, measured using a single pixel triggering mode (select events where only one pixel triggered), is proportional to the efficiency of the pixel. Therefore the relative efficiencies of all 16 pixels can be measured. The energy condition was set to the K-REC line.

8.3.2 Internally normalized intensity distribution

For data evaluation , the 90° rotational symmetry of the 4x4 pixel detector was exploited. Here the fact was used that for the Compton scattering from a given pixel P1 into a pixel P2 (defining the scattering angle ϕ) always a further pixel P3 exists with an identical geometry (P1→P2)=(P1→P3) except that the Compton scattering direction differs by 90°, i.e. $\phi + 90°$. This internal intensity normalization $I_\phi / I_{\phi+90°}$ was used in order to cancel out geometrical effects like different solid angles of the pixels and different scattering distances, see figure 8.10a,b for comparison. Note that after the normalization the values of the scattering intensity are fitted with a corresponding theoretical normalized distribution based on Klein-Nishina formula.

Figure 8.11 shows a normalized scattering intensity distribution for the K-REC line at 400 MeV/u projectile energy and 90° observation angle. As already mentioned before, the scattering into neighboring pixels was not analyzed because of the high background arising from detector-specific effects like charge splitting between the neighboring pixels and the mirror signals. Because the scattering ge-

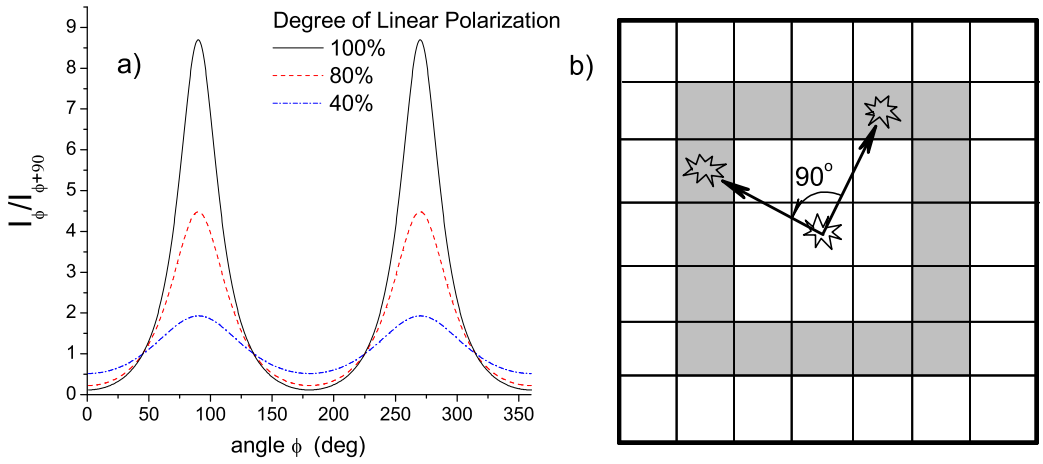

Figure 8.10: a) Theoretical normalized Compton scattering distribution for different degrees of linear polarization. b) An example of a pair scattering directions which is used for the normalization (I_ϕ and $I_{\phi+90^\circ}$). Scattering to the marked pixels contribute most to the statistics.

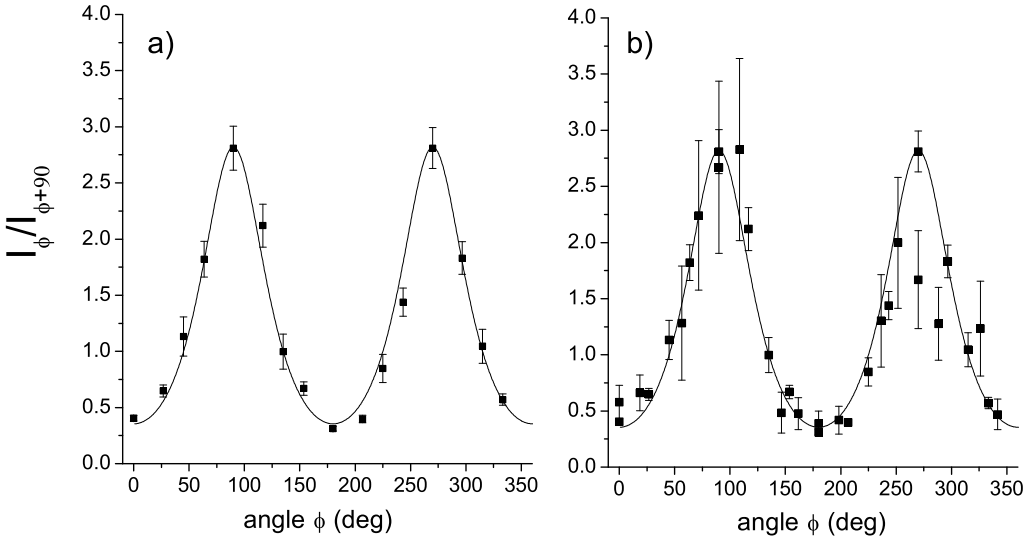

Figure 8.11: Normalized scattering distribution. a) Normalized intensity for scattering between two pixel having one pixel interval. b) Normalized intensity for the scattering between pixels having one and two pixels interval.

ometry inside the detector is not precisely determined, for instance the scattering angle θ is not known (compare figure 8.19), the Compton scattering events have no contrast to the background events of the described above nature. This is the reason why the Kinematic Event Selection does not work perfectly for neighboring pixels. In order to solve this problem the detector must have a 3D readout and a better spatial resolution (smaller pixel size). For neighboring pixels also the direction of the scattering is determined very roughly. The angle ϕ can be distributed over 180°.

The scattering between two pixels, having one pixel interval, contributes most to the statistics, see figure 8.10b and figure 8.11a for the corresponding normalized distribution. The statistics of the scattering between pixels having two pixels interval is more strongly suppressed by photoabsorption inside the Ge crystal, figure 8.11b.

8.4 Monte-Carlo simulation/fitting program

Simulation of the detector response for the polarized light constitutes an important step in data analysis. One should note that each point of the scattering distribution still has a different geometry of the scattering. This must be taken into account during the fitting of the experimental data.

The fitting program is based on Klein-Nishina formula. It takes into account the geometry of the detector, the discussed above effects of the finite pixel size and Compton- and photoattenuation. The scattering and the absorption centers are distributed over the pixel dimensions with a probability obtained by a Monte-Carlo simulation. The Compton angular differential cross section is therefore averaged-out over these distributions. The following physical effects were also taken into account in the simulation and fitting program:

1. multiple Compton scattering;

2. relativistic Compton scattering on bound electrons and *Compton Profile*;

3. Rayleigh scattering (coherent elastic scattering);

4. uncertainty in the detector depletion depth.

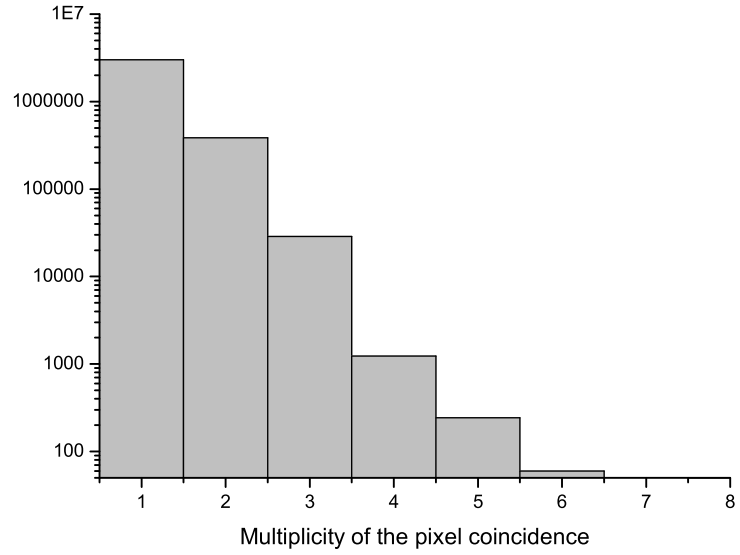

Figure 8.12: Multiplicity of the coincidences inside the detector: the number of pixels triggering at the same time.

To the detailed discussion of the above listed effects the next chapter is devoted.

8.5 Model description and errors estimation

8.5.1 Multiple scattering

In the chapter 3.2 the probability of multiple Compton scattering followed by a complete photoabsorption was discussed. Multiple Compton scattering events can be detected by the pixel detector. Figure 8.12 shows the distribution of the multiplicity of the coincident events, the number of pixels triggering simultaneously inside the detector. One can see that the probability of the next multiplicity decreases by almost one order of magnitude with respect to the previous one. It is also possible to analyze the multiple Compton scattering. By applying the Compton kinematic energy conditions one can track the photon inside the detector. But without a precise 3-dimensional geometrical information it is impossible to determine the sequence of the scatterings with 100% confidence. Due to the

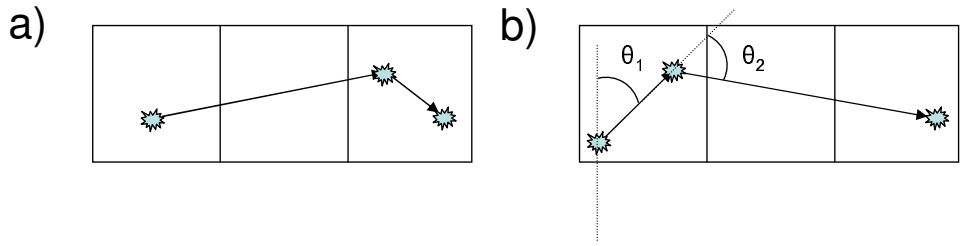

Figure 8.13: Multiple scattering inside one pixel. Angles θ_1 and θ_2 define the geometry of double Compton scattering.

low probability of the multiple scattering and relatively complicated analysis of these events, they where not evaluated. The double Compton scattering events, where the photon after the last interaction escaped the detector, contribute to the background of the coincidence spectrum. But as far as the energy of the photon after the first scattering is approximately the half of the initial energy or less, the next Compton scattering occurs close to the Thomson limit, the electron deposition is low and the escaped photons carries away the biggest part of the energy. This means that these events from the K-REC line contribute mostly to the low-energy background. *Therefore the effect on the deduced degree of linear polarization is negligible compared to other systematic effects.* In figure 8.7 one can see that the background in the middle part of the spectrum is quite high.

8.5.2 Multiple Compton scattering inside one pixel

Figure 8.13 shows the case of double scattering inside one pixel. The first case does not affect the scheme of the polarization detection if the last scattering is followed by a full photoabsorption. The first scattering direction and the energy of the scattered photon are determined in the same way to the single scattering case. The second case has potentially a problem, because the directions of the photons after the second scattering are changed, but these photons can have energies, close to the energies of the first scattered photons, and therefore it is impossible to separate them from the single scattered photons. They contribute to the background of the scattering intensity distribution and therefore can in-

crease the systematic error of the measured polarization. Nevertheless a numerical simulation of this process (double scattering inside one pixel followed by a photoabsorption in another pixel) shows that its probability is 10^4 times smaller than the probability of the single scattering. *Therefore the multiple scattering inside one pixel has a negligible effect on the measured polarization.*

Analysis of multiple scattering events

As a comment one can say that such multiple Compton scattering events can be used to analyze the polarization of the X-rays of higher energies, where the probability of the multiple scattering is significantly higher, see figure 3.6 for comparison. Also an utilization of the new generation of the segmented detectors with a fine segmentation will provide more possibilities in this respect. Therefore it is important to know the properties of such processes, e.g. the scattering angular distributions, although this result is not used in the present work.

Figures 8.14 and 8.15 show a simulated θ angular distribution of the first and the second scattered photons for the case of double Compton scattering. As far as the final absorption can take place only in the detector plane the sum of angles must be approximately constant $\theta_1 + \theta_2 \approx 90°$. One can see that the first scattering has a preferable forward direction whereas the second covers the rest of the needed angle. This becomes obvious if we consider that the total Compton cross section is larger for higher energies and that scattering on larger angles decreases the energy of the Compton photon. Unfortunately this case is not in favour of the polarization measurement. The other way around, with a small second scattering angle, would be much better, because it would not introduce a big error to the detection of the initial scattering direction, the one which depends on the polarization. In future polarization studies, in order to analyze properly such events, one needs to investigate how the photon polarization is affected by Compton scattering.

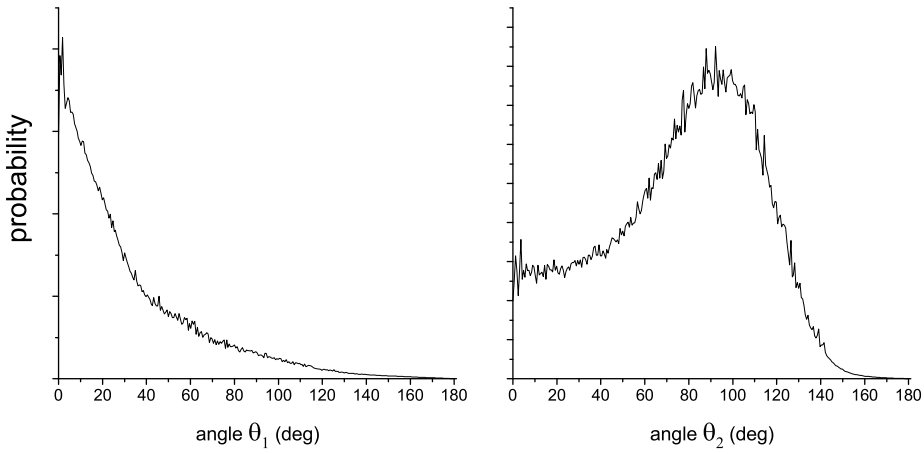

Figure 8.14: A simulated angular distribution of the first and the second Compton scattering inside one pixel for the case where the last photon is absorbed in another pixel, see figure 8.13b.

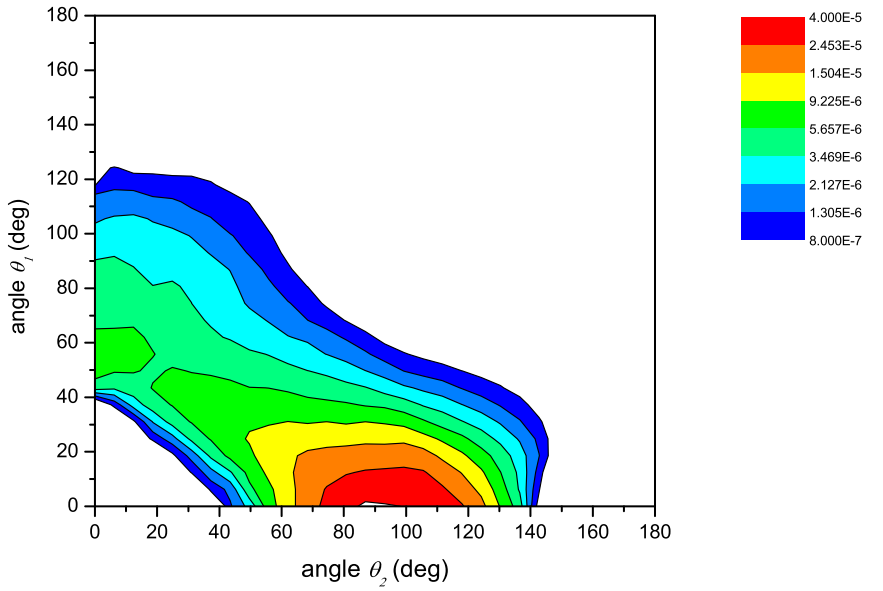

Figure 8.15: A simulated angular distribution of double Compton scattering occurred in one pixel. The scattered photon is absorbed in another pixel.

8.5.3 Relativistic scattering on bound electrons and Compton profile

In the Impulse Approximation [134], which was used for the theoretical description of the Compton scattering process and for the fitting procedure, the electron is considered to be free with a momentum distribution (Compton profile) corresponding to the electronic bound states of the material used, see chapter 6.3.1. This approximation is valid as long as the target electron binding energies are considerably smaller than the energies of the incoming photons.

A double differential cross section for Compton scattering which includes the electron motion with a momentum distribution $\rho(\vec{p})$, the Compton Profile $J(p_z) = \int\int dp_x dp_y \rho(\vec{p})$ and effects of relativistics in first approximation for the polarized photons is shown here [135, 136, 137]:

$$\frac{d^2\sigma}{d\omega' d\Omega} = \frac{r_0^2 m^2 \omega'}{2\omega|\vec{k} - \vec{k'}|\sqrt{m^2 + p_z^2}} \left(\frac{R'}{R} + \frac{R}{R'} - 2\sin^2\theta\cos^2\varphi \right) J(p_z) \tag{8.2}$$

where

$$R = \omega \left(\sqrt{m^2 + p_z^2} + (\omega - \omega'\cos\theta) p_z / |\vec{k} - \vec{k'}| \right) \tag{8.3}$$

$$R' = R - \omega\omega'(1 - \cos\theta) \tag{8.4}$$

$\vec{k} - \vec{k'}$ is a photon scattering vector, p_z is the projection of the momentum of the initial electron on $\vec{k} - \vec{k'}$. Here the Compton profile $J(p_z)$ gives rise to a broadening of the Compton line because of the electron motion before the collision. The term $\sqrt{m^2 + p_z^2}$ reflects relativistic effects at the scattering process. As far as the energy transfer is not much smaller than the electron rest mass energy it is important to consider relativistic effects in the calculations. A comparison of the Klein-Nishina-like expression $X_{Klein-Nishina} = \omega/\omega' + \omega'/\omega - 2\sin^2\theta\cos^2\phi$ with the more exact relativistic treatment $X_{relativistic} = R/R' + R'/R - 2\sin^2\theta\cos^2\phi$ was given in [137]. The difference between these treatments increases with increasing of the electron momentum and can not be neglected already when $p_z \gtrsim 5 \div 10$ *a.u.* The deviations are especially significant for scattering angles θ close to 90° [137].

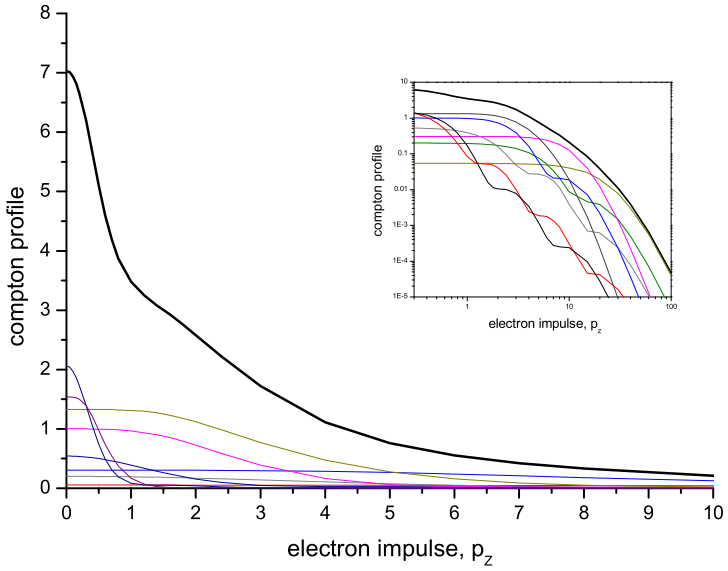

Figure 8.16: Compton Profile of Ge in atomic units. The thick curve represents the total Compton Profile. The thin curves represent Compton Profiles of electrons of different levels of Ge atom.

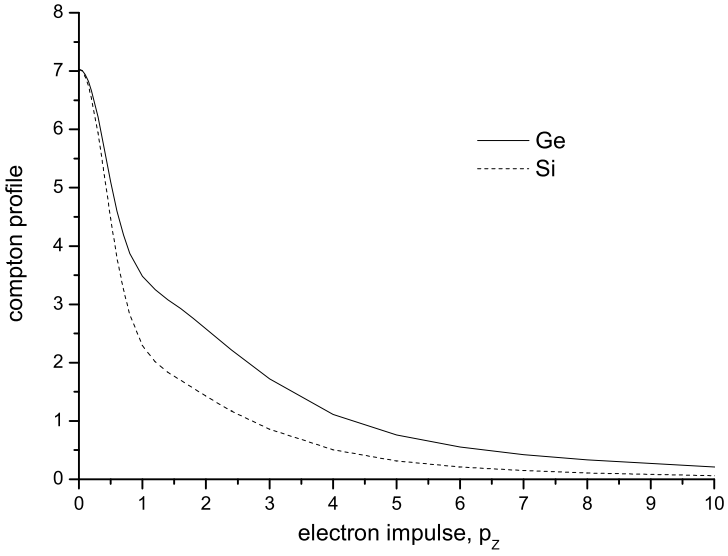

Figure 8.17: Comparison between Compton Profiles of Ge (Z=32) and Si (Z=14).

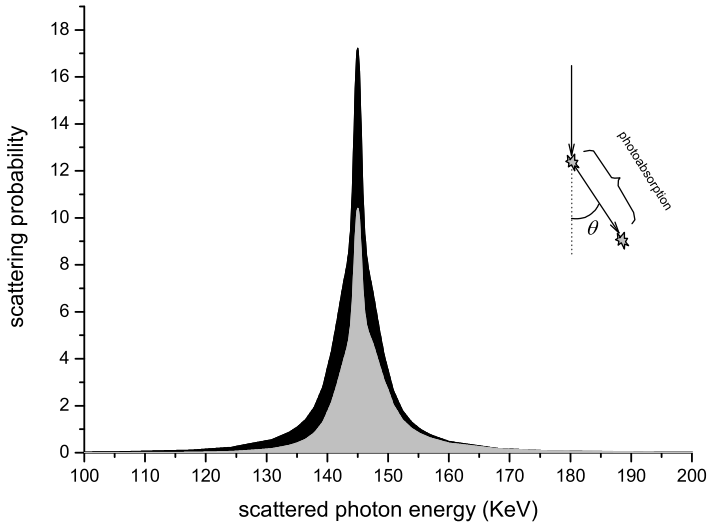

Figure 8.18: Scattered photon energy distribution. Black curve shows the energy distribution of the scattered photon directly after the scattering, grey curve - after a propagation to the detection point.

Figure 8.16 shows the Compton Profile of Ge. The total Compton Profile is a superposition of Compton Profiles of all bound electrons of Ge. The strongly bound electrons like 1s, 2s, 2p have larger momenta and contribute most to the wide shoulders of the total Compton momentum distribution. Weakly bound electrons 4s and 4p are responsible for the low momentum part of the Compton Profile and the FWHM is determined mostly by them. And 3s, 3p and 3d electrons determine the middle feature of the profile. Figure 8.17 shows a comparison between Compton Profiles of Ge (Z=32) and Si (Z=14). One could see that for Si the FWHM is smaller which constitutes one of the advantages of Si detectors.

A numerical simulation using the equation 8.2 was performed for the Ge Compton Profile. Figure 8.18 shows an energy distribution of the scattered photon where the initial photons have a fixed energy. This distribution can be understood also as an energy condition $E_{ph} \approx E_{ph0} + E_{bind}$, where E_{bind} is a binding energy of the electron which participated in the scattering. The maximum Ge electron binding energy $E_{K-shell} = 11.103$ KeV determines the wide shoulders of the Compton broadening.

The gray area shows the energy distribution of the scattered photon after the propagation to the detection point. The asymmetry in the shape is caused by the energy dependant attenuation (Compton and photoabsorption) inside Ge crystal. It also results in a slight energy shift of the detected scattered photon and therefore changes the deduced degree of the linear polarization. *This effect is correctly included in the fitting procedure and therefore the caused systematic uncertainty is negligible for this method.*

Considering the effects of the relativistic kinematics and of the Compton Profile together with the photoabsorption results in $\approx +1.3^\circ$ shift in the deduced degree of linear polarization.

8.5.4 Rayleigh scattering (coherent elastic scattering)

As it was already discussed in chapter 2.2.3, Rayleigh scattering is an elastic scattering process and no energy is deposited in the scattering center. Therefore it doesn't contribute to the coincident spectra. Nevertheless a possible scenario where the Compton events can be followed by Rayleigh scattering can introduce an error in determining the direction of Compton scattering. Due to the fact that Rayleigh scattering is strongly forwarded (see figure 2.8), the introduced uncertainty is small. *The numerical simulation for this case shows +0.5% shift in the deduced degree of linear polarization.*

Another scattering scenario which can introduce a systematic error is the Rayleigh scattering followed by a Compton scattering. The direction of the Rayleigh photon can differ from the initial photon direction. This introduces an uncertainty in the consequent Compton event geometry, i.e. an error in the Compton angle θ. For the incoming photon energies larger than 200 KeV the probability of the Rayleigh scattering into a broad angle band around 90° is estimated to be smaller than 0.1% relative to the Compton effect probability.

8.5.5 Uncertainty in the detector depletion depth

The active zone of the detector in Z dimension is defined by a *Depletion Depth* which depends on the applied bias high voltage. The detector normally operates at 2000 V which provides 13 mm $\div$ 15 mm depletion depth. As one can see

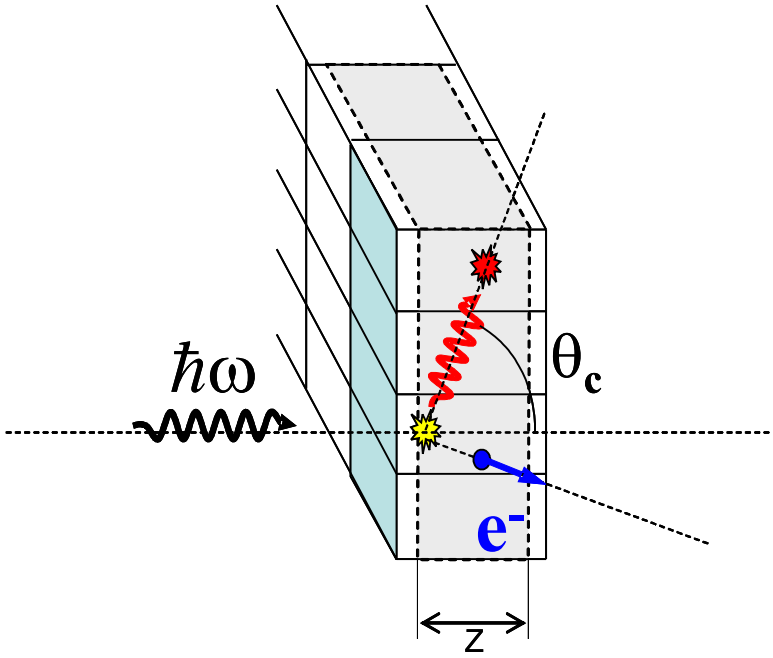

Figure 8.19: Compton scattering geometry depends on the Depletion Depth of the detector (Z dimension).

in figure 3.3, the differential cross section of the Compton scattering process has a bigger probability in the forward direction. But the detector geometry limits the minimum scattering angle. The minimum and therefore the mean scattering angle θ_c depends on the depletion depths of the detector. On the other hand, the modulation factor $M(\phi)$ strongly depends on θ_c, see formulae 2.7 and 3.1 for comparison. Due to this dependance, the uncertainty in the depletion depth introduces an uncertainty in the calculated degree of the linear polarization. *Assuming the depletion depth to be 14 mm ± 1 mm, the introduced error reaches* $\pm 2°$ *up to* $\pm 3°$ *depending on the photon energy.* This is the largest systematic effect which is not well under control and depends on a high voltage applied to the detector. A further improvement of the accuracy in this respect will require a detailed study of the photon and electron detection near the edge of the depletion zone or, as an alternative, a readout system which will provide a 3D information for each event.

8.5.6 Summary for the systematic effects

An influence of the effects discussed before on the deduced degree of linear polarization was studied in detailes. These effects are included in the fitting routine. The following list summarizes estimates for the various effects obtained by numerical simulations:

1. multiple Compton scattering has no effect on the measured polarization;
2. relativistic Compton scattering on bound electrons and Compton profile results in +1.3% shift of the degree of the polarization and the systematic error is negligible;
3. Rayleigh scattering is estimated to affect the polarization data by less than a +0.5% while assumed as a systematic error;
4. uncertainty in the detector depletion depth results in ±3 % systematic error.

Assuming an independent error propagation for the individual systematic uncertainties, the overall systematic error of ±2° up to ±3° depending on the photon energy is obtained.

Additional considerations for future polarimeters and Compton cameras

It is relevant to note that the Compton Profile is a general limitation for the angle resolution for Compton Cameras [138], the Compton Imaging devices based on Gamma/X-ray tracking detectors or detector arrays, see for instance [82, 139]. For this purpose it is then more preferable to use elements with a narrow Compton Profile like Si, at least as a scatterer in case when the scatterer and absorber are separate. One of the best choices for the Compton Camera for spectroscopy purposes in the energy range of 60 KeV ÷ 1 MeV would be two 2D position sensitive detectors placed one behind another. A Si detector must be used in front as a scatterer, providing a relatively big efficiency in the Compton Scattering with respect to the photoabsorption (see figure 3.5) and the narrow Compton Profile, and a Ge detector behind it as an absorber, providing a big efficiency in the photoabsorption. Both of these type of the detectors have the necessary energy

and time resolution for the Imaging, Polarimetry and Spectroscopy purposes. The detectors must have a segmentation of the order of typical absorption distance or less to have relatively good efficiency and not high complexity. For types of detectors listed above 1-2 mm pixel size would be appropriate.

Chapter 9

Results and discussion

As an example, figure 9.1 shows a typical angular distribution for Compton scattering of K-REC photons as measured by the Pixel Detector. The experimental values for the linear polarization are deduced from these distributions using the method which was described in chapter 8. The statistical error bars were obtained from a MINUIT-based fitting routine with two free parameters only. The first parameter is the degree of linear polarization and the second one is the angle of the polarization vector with respect to the reaction plane: the plane defined by the ion beam and the photon emission direction.

Results obtained for linear polarization of K-REC into bare uranium for different beam energies and observation angles are summarized in table 9.1. The statistical and systematic errors are shown separately. The latter arises mainly from the uncertainty in the *Depletion Depth* of the pixel detector used. Uncertainties introduced by multiple scattering, the Compton Profile and Rayleigh scattering are found to be negligible (see section 8.5). The overall error was obtained assuming no correlation between the statistical and systematic uncertainties. Typical values for the reduced χ^2 for the fitted scattering distributions were in the range between 1.4 to 2.6 with an exception for 132 MeV/u and 60° where χ^2 amounts to 3.6. The extracted angle of the polarization vector with respect to the reaction plane is found to be zero with an uncertainty between $\pm 3°$ and $\pm 6°$ depending on the measurement.

The experimental data, compared with the results of the exact relativistic calculation of J. Eichler et al. [18] and A. Surzhykov et al. [19], are summarized in

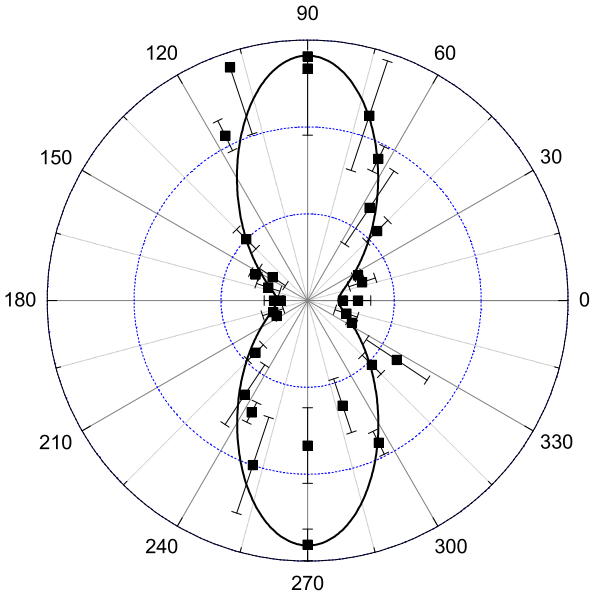

Figure 9.1: The measured angular distribution of the Compton scattering intensity inside the Pixel Detector. The fitted distribution is plotted for the 400 MeV/u projectile energy and 90° observation angle. A strong asymmetry of the angular distribution indicates a large degree of linear polarization. The measured polarization angle is $0 \pm 3°$ with respect to the reaction plane, the plane defined by the ion beam direction and the photon emission direction.

table 9.2. Good agreement between the theory and the experiment was obtained for all experimental points.

In figure 9.2, the experimental values for the linear polarization measured at 60° and 90° bare uranium ions at 400 MeV/u are plotted together with the theoretical results. The experiment supports the exact relativistic calculation which predicts a strong depolarization effect in the forward hemisphere, see section 4.4.1. Theoretical predictions for 100 and 800 MeV/u are shown for comparison. The calculation implies a strong dependance of the K-REC photon polarization on the beam energy, especially at forward angles.

Figure 9.3 shows the experimental results for the linear polarization measured at 60° observation angle for different projectile energies. A theoretical prediction is also shown for comparison. The decrease of the degree of polarization at higher projectile energies is explained by magnetic interactions which start to play an important role at relativistic energies.

Ion Beam Energy, MeV/u	Observation Angle	K-REC Energy, KeV	Degree of the linear Polarization	Statistical Error	Systematic Error	Overall Uncertainty
400	90°	246	**0.79**	±0.07	±0.03	**±0.08**
400	60°	382	**0.61**	±0.12	±0.02	**±0.12**
190	60°	270	**0.722**	±0.05	±0.02	**±0.05**
132	60°	236	**0.834**	±0.04	±0.03	**±0.05**
98	60°	214	**0.845**	±0.06	±0.03	**±0.07**

Table 9.1: Experimental results for the degree of the linear polarization of the K-REC radiation for bare uranium ions stored at the ESR at different projectile energies. Statistical and systematic errors were added quadratically to obtain the overall uncertainty.

Ion Beam Energy, MeV/u	Observation Angle	Degree of the linear Polarization	Theoretical values
400	90°	0.79 ± 0.08	0.835
400	60°	0.61 ± 0.12	0.692
190	60°	0.722 ± 0.05	0.803
132	60°	0.834 ± 0.05	0.838
98	60°	0.845 ± 0.07	0.859

Table 9.2: Experimental results for the degree of the K-REC polarization compared with the theoretical values of J. Eichler et al. [18] and A. Surzhykov et al. [19].

In order to illustrate this finding in more details the contributions of electric and magnetic multipoles to the K-REC polarization are shown in figure 9.4. Here, one can see that magnetic effects, i.e. the motional electro-magnetic field of the projectile couples with the magnetic moment of the electron, has a large effect on the photon polarization at all observation angles. Magnetic contributions are especially significant at

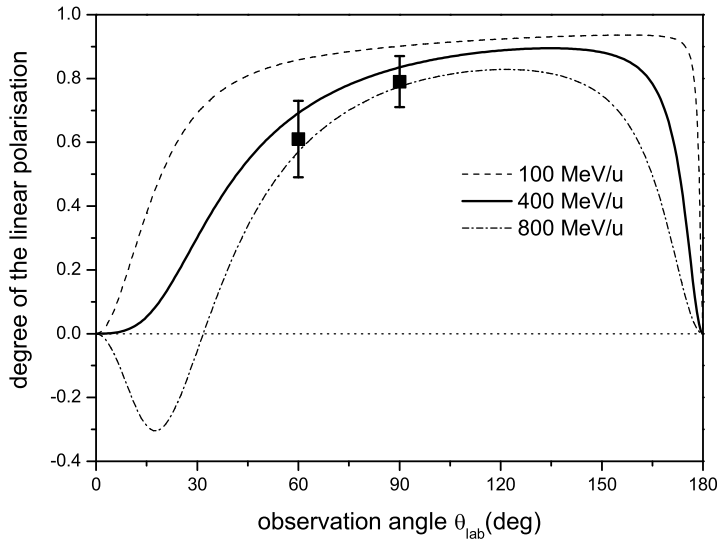

Figure 9.2: Experimental results for the linear polarization of the K-REC for 400 MeV/u bare uranium ions. Theoretical curves of the exact relativistic calculations for the polarization angular dependencies are displayed for the bare uranium beam energies of 100 MeV, 400 MeV and 800 MeV [19].

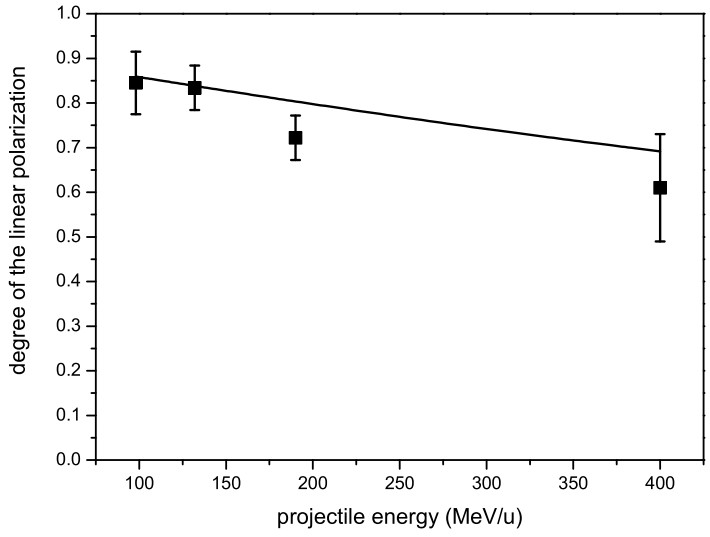

Figure 9.3: Experimental results for the linear polarization of the K-REC for 98, 132, 190 and 400 MeV/u bare uranium ions. The observation angle is 60°. The theoretical curve from exact relativistic calculations for the polarization energy dependance is displayed as well [19].

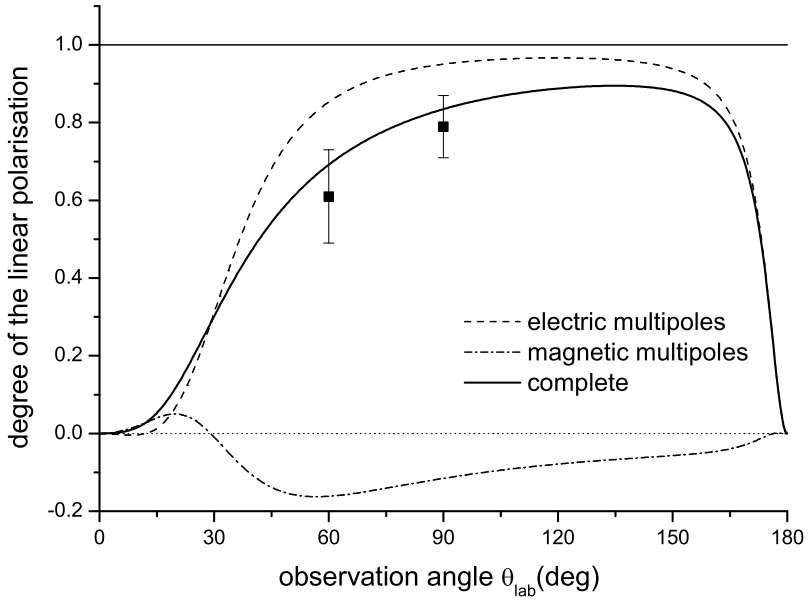

Figure 9.4: Experimental results compared with the complete relativistic calculation of A. Surzhykov at al. [19] for bare uranium at 400 MeV/u. Results where only electric or magnetic multipoles are taken into account are shown separately. The straight line at 1.0 (complete polarization) denotes the result of the nonrelativistic calculation.

angles between 60° and 150°. At forward angles electric multipole contributions lead to depolarization whereas magnetic multipoles increase the degree of polarization. In particular the cross-over effect, occurring at higher projectile energies, is originated by the electric multipoles. Note that magnetic effects such as spin-orbital interaction occurring in presence of a heavy nucleus are taken into account by the Dirac electron wavefunction and are included in the electric multipole contributions. The measured values show the importance of considering both the strong field effects (spin-orbital coupling) and magnetic interactions (coupling of the electron spin with the motional field of the ion). For the case of the linear polarization of the K-REC photons, these effects show up in a particular clean way.

For completeness, one may compare the K-REC angular distribution (section 5.2, figure 5.3) with the angular dependent photon polarization displayed in

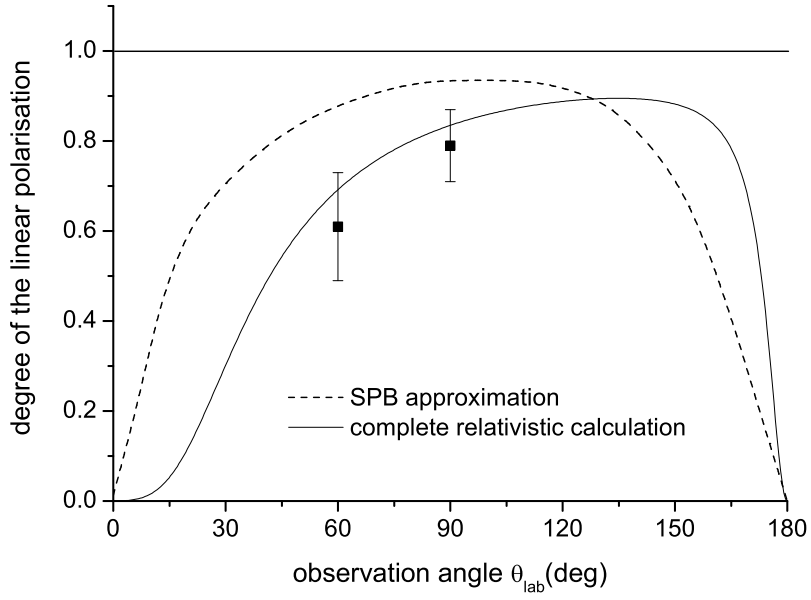

Figure 9.5: Experimental results compared with the complete relativistic calculation [19] for bare uranium at 400 MeV/u. The extended strong potential Born (SPB) approximation calculation is plotted for comparison [140]. A straight line at 1.0 denotes the result of the nonrelativistic calculation.

figure 9.4. This is in contrast to the angular differential K-REC studies where a cancellation effect between higher multipoles and the Lorentz transformation occurs (except close to 0°). There a complete relativistic treatment introduces only a small deviation from the pure $\sin^2\theta$ distribution for the laboratory frame. In contrast, there is no cancellation effect for the polarization of the K-REC photons. The degree of the K-REC polarization deviates significantly from the non-relativistic result which predicts a 100% polarization for all observation angles. Therefore polarization studies give a direct measure of relativistic effects in radiative recombination.

In figure 9.5, the experimental data are in addition compared with a strong potential Born approximation (SPB) [140]. In contrast to a usual Born approximation the SPB includes a distortion of the wave functions as introduced by the Coulomb potential [141]. As seen in the figure 9.5, this approximation is obvi-

ously in disagreement with the experimental finding. This disagreement arises from the importance of the spin-orbital interaction and other strong field effects which are not completely considered by the SPB approximation. Nevertheless, this theory qualitatively describes the behavior of the linear polarization including the cross-over effect [140, 142].

The result for the angle of the polarization ellipse deduced from the Compton scattering distribution (see figure 9.1) $\chi_0 = 0.^\circ \pm 3^\circ$ proves the theoretical prediction that for K-REC the linear polarization is aligned in the plane defined by the ion beam direction and the direction of the emitted photons, assuming an unpolarized ion beam (see figure 9.6) [19, 21].

As shown, the method developed here leads to a good polarization angular resolution. Using it we achieve an angular sensitivity of $\pm 3^\circ$ with the pixel detector used in this work. However, one should keep in mind that this detector has a rough segmentation matrix with 7x7 mm pixel size and therefore a broadening of up to $\pm 15^\circ$ in every scattering direction. Applying this method to a new generation of segmented detectors with millimeter or submillimeter position resolution should allow for an angular resolutions of the order of $\pm 0.5^\circ$. Such resolutions should be sufficient to access experimentally effects of the ion beam spin polarization (see chapter 4.4.1 and figure 4.8). Figure 9.7 shows a theoretical prediction for the polarization angle of K-REC photons for spin-polarized H-like $^{209}_{83}$Bi ion beam. One can already see that at an observation angle $\theta = 30^\circ$ the degree of the ion beam spin polarization can be measured with an accuracy of 10 %, having a $\pm 0.5^\circ$ precision for the K-REC polarization angle.

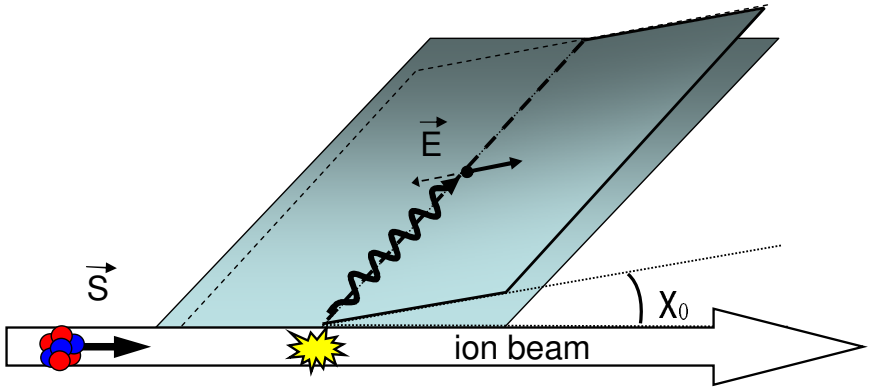

Figure 9.6: Rotation of the K-REC polarization vector $\vec{E}$ for a longitudinally spin-polarized ion beam.

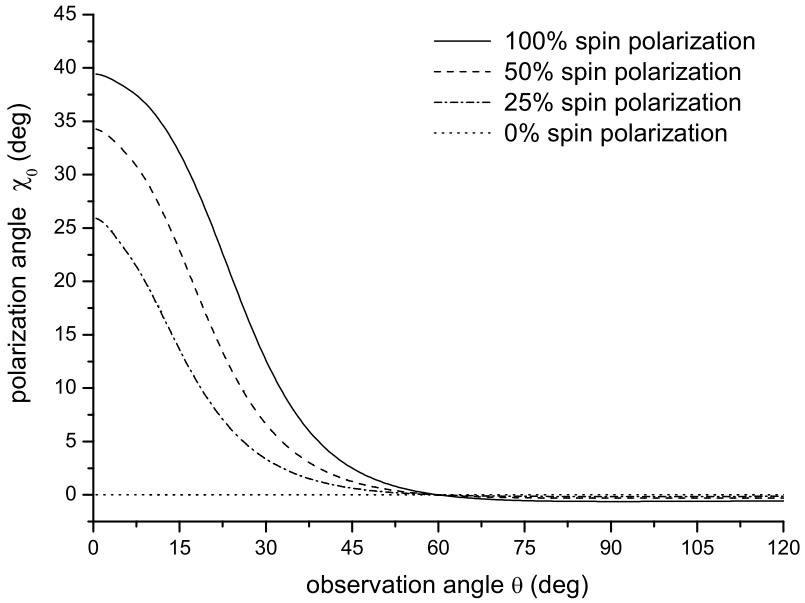

Figure 9.7: Rotation angle of the K-REC polarization ellipse χ_0 for the longitudinally spin polarized H-like $^{209}_{83}$Bi ion beam with a nuclear spin I=$\frac{9}{2}$. The projectile energy is 400 MeV/u. Different degrees of the ion beam spin polarization are considered [21].

Chapter 10

Outlook

As it was described in this work the new segmented Pixel Detector has found an important application in the advanced experimental studies of the Radiative Electron Capture into heavy ions in the relativistic regime. These investigations open many new perspectives for the studies of REC and more general for the investigations of polarization phenomena in relativistic ion-atom and ion-electron collisions.

10.1 REC polarization studies

The non-destructive diagnostics of the beam spin polarization was a subject of discussions for a long period of time. In recent years several experiments with polarized ion beams were proposed. For instance a study of a parity nonconservation phenomena in few-electron systems [143] or spin-dependent effects in electron capture processes [144]. However, a reliable method of controlling and measuring the ion beam spin polarization, required for such experiments has not been developed up to now. Nevertheless the recent theoretical investigations of the polarization of REC into spin-polarized ions cast new light on this topic [21]. As it was already discussed in the chapter 4, the effect of the ion spin polarization in the REC process leads to a non-zero non-orthogonal component of the REC polarization P_2, see figure 10.1. In terms of the polarization ellipse this means that the ellipse has a non-zero angle with respect to a plane defined by the ion beam and photon beam directions. The measurement of this angle can be ac-

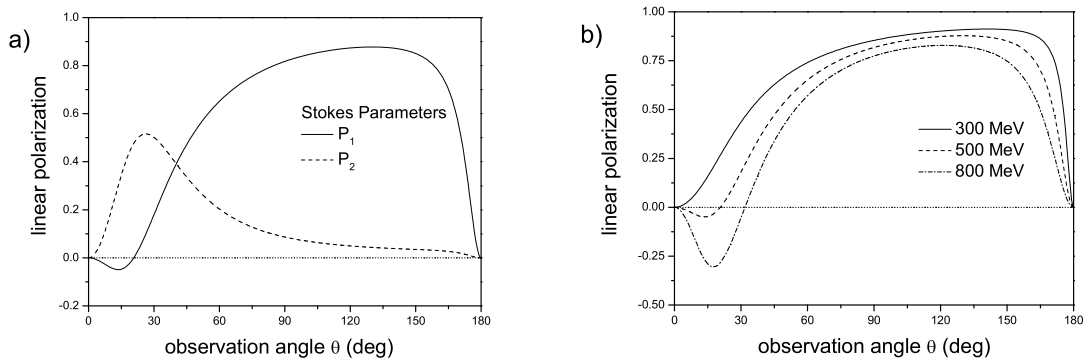

Figure 10.1: **a)** The Stokes parameters P_1 and P_2 of recombination/REC photons for capture into the K–shell of the bare uranium ions at an energy of 500 MeV/u [21]. The Stokes parameter P_2 is shown for the capture of completely polarized electrons. **b)** Projectile energy dependence of the linear photon polarization of recombination/REC photons for capture into the K–shell of the bare uranium ions at energies of 300 MeV, 500 MeV and 800 MeV. The negative value of the P_1 Stokes parameter illustrates the *cross over* phenomenon: changing of the REC polarization plane to a perpendicular to the reaction plane for high projectile energies [19].

complished with the established technique using the existing Pixel or 2D stripe detectors.

A possible experimental approach to polarize ion beams in storage rings has been discussed in [145]. It is proposed to use a selective laser excitation of the hyperfine sublevels of the H-like $^{151}_{63}Eu$ ion with a nuclear spin $I = \frac{5}{2}$ leading to group-state hyperfine levels with $F = 2$ and $F^{'} = 3$. Due to the strong hyperfine interaction in these ions (hyperfine splitting is $\Delta E = 1.513eV$) the nuclei will be polarized after about 10^{-15} s. It is also shown that these investigations can be accomplished with the current GSI ESR installation.

In the New Experimental Storage Ring NESR, which is a part of the GSI future project [146], the maximum projectile energy of the stored heavy ions will reach 800 Mev/u. At such high projectile energies the theoretically predicted *cross over* effect of the REC polarization should occur, see figure 10.1. In its time reversal, it corresponds to the *cross over* predicted and observed in photoionization [108, 109, 110, 111]. Up to now this effect was not observed for REC into highly charged heavy ions, moreover the experimental accuracy is expected to be much

higher than the one obtained in the photoionization studies.

10.2 The 2D stripe detector

The current experimental studies of the REC polarization were performed with the Pixel Detector, which can be considered as a prototype for more elaborated planar germanium detectors with finer segmentation. As it was discussed in chapter 3.2.1, for general polarimetry purposes the optimum detector segmentation should be of the order of 1 mm.

Recently a prototype germanium diode (70 mm x 41 mm, 11 mm thick) with a boron implanted contact and an amorphous Ge contact was developed at IKP FZ-Jülich (D. Protic, Th. Krings et al.), see figure 10.2. A 128 strip structure on an area of 32 mm x 56 mm with a pitch of 250 μm on the front contact (implanted) and 48 strip structure with a pitch of 1167 μm on the rear contact (amorphous Ge) are realized with the help of plasma etching. The detector is mounted in a cryostat which will enable any orientation of the detector with respect to a photon source. Since August 2004 this 2D μ-strip detector is available for experiments at GSI.

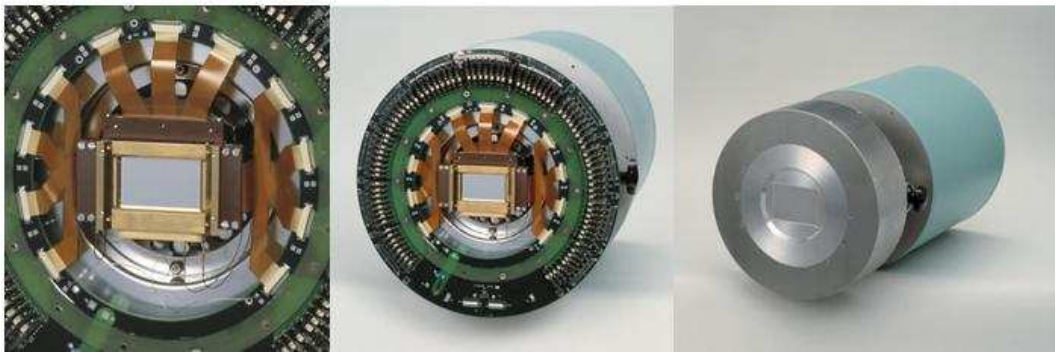

Figure 10.2: The 2D μ-STRIP detector system developed at IKP FZ-Jülich for future Lamb Shift and photon polarization studies at the ESR storage ring.

The efficiency of this detector as a polarimeter is expected to be at least 10 times larger compared to the old Pixel Detector. Besides this, the angular

resolution of the linear polarization will be significantly increased due to the much finer segmentation. The angular resolution will play in particular important role in the ion beam polarization studies. For this purpose the detector housing has a symmetrical design, allowing its complete rotation along the central axis.

A polarization sensitivity calibration experiment on a synchrotron radiation source for the old Pixel and the new 2D stripe detectors is scheduled for the spring 2005 at the ESRF synchrotron facility in Grenoble.

A possible X-ray imaging application of this detector as a *Compton Camera* is now under discussion. For this purpose a 3D readout of the X-ray events is required. This can be accomplished via a signal pulse shape analysis, based on a DSP readout system, which is currently under development in the Krakow University, Poland.

Besides the polarimetry applications this detector will be used for the future Lamb shift experiment in combination with the FOCAL spectrometer [26], providing a high position resolution required for the accurate spectroscopy.

Chapter 11

Summary

In this work a first study of the photon polarization for the process of radiative recombination has been performed. This was done at the ESR storage ring at GSI for uranium ions colliding with N_2 at various collision energies. For this measurement a high purity Ge *Pixel Detector* with a 4x4 segmentation matrix was applied [1]. Figure 11.1 shows a principle scheme of the performed experiment. The investigation was performed at the Gas-jet target of the ESR. The detector was placed at 60° and 90° observation angles. The sensitivity of the *Compton scattering* effect to the linear polarization of the X-Ray radiation was employed for the polarization measurement.

Detailed investigations of the scattering and geometrical effects inside the detector were performed in order to develop a method to interpret the experimental data and extract the degree of the linear polarization in the hard X-Ray regime with a high precision. A special emphasis was given to the geometry of the detector and it's influence on the measured pixel-to-pixel Compton scattering intensities. In the figure 11.1 one can see a typical angular distribution for the Compton scattering, normalized to the pixel solid angles and efficiencies. Besides the geometrical factors, effects like *relativistic Compton scattering off bound electrons* (*Compton profile*), *Rayleigh scattering*, uncertainty in the *Depletion Depth* and *multiple* Compton scatterings were analyzed in details. This allowed for a proper fitting of the experimental data and an extraction of the degree of the linear polarization with a high accuracy. The developed method enabled to achieve

[1] provided by D. Protic, FZ Jülich

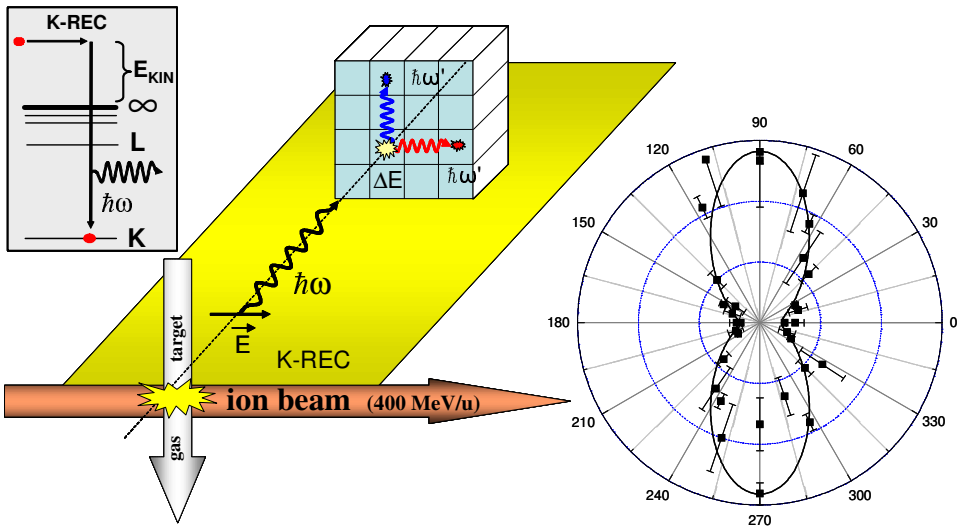

Figure 11.1: Principle scheme of the first polarization study of the REC performed at the GSI ESR storage ring with the Pixel Detector: analysis of the Compton scattering intensities in different directions inside the detector. The polar plot shows the typical Compton scattering intensity angular distribution inside the Pixel Detector - the way to extract the degree of the linear polarization.

a precision of the order of 10% with the Pixel Detector which is dominated by the statistical uncertainties.

The obtained results show a good agreement with the theoretical values derived from the exact relativistic calculations. For the case of the linear polarization of the K-REC photons, the measured data confirm the theoretical prediction that strong depolarization effects occur for high projectile charges in the forward hemisphere. The latter is in disagreement with the nonrelativistic theory which predicts a 100 % polarization regardless of the emission angle.

Chapter 12

Zusammenfassung

Experimente zum radiativen Elektroneneinfang (REC, Radiative Electron Capture), der Zeitumkehrung der Photoionisation, wie er in Stößen hochgeladener, relativistischer Schwerionen mit leichten Gasatomen auftritt, ermöglicht einen einzigartigen Zugang zum Studium der Photonen-Materie-Wechselwirkung im Bereich extrem starker Coulombfeldern. So ist die REC-Strahlung im relativistischen Bereich zum einen geprägt durch das Auftreten von höheren elektrischen und magnetischen Multipolordnungen und zum anderen durch starke Retardierungseffekte. In Folge dessen wurde der REC-Prozeß in den vergangen Jahren sehr detailliert untersucht, wobei sich die experimentelle und theoretische Forschung auf die Emissionscharakteristik der REC-Photonen konzentrierte, wie z.B. auf Untersuchungen von Winkelverteilungen und Linienprofilen. Mittlerweile kann der REC-Prozeß als ein - selbst für die schwersten Ionen - wohlverstandener Effekt angesehen werden. Allerdings entzog sich den Experimenten bislang eine zur Beschreibung der Photonenmission wesentlich Größe, nämlich die Polarisation der Strahlung.

Die lineare Polarisation der REC-Strahlung, wie sie in Stößen zwischen leichten Atomen und den schwersten, hochgeladenen Ionen vorhergesagt wird, war der Gegenstand der vorliegende Arbeit, in der es erstmals gelang, die diese für den konkreten Fall des Einfangs in die K-Schale von nackten Uranionen nachzuweisen und im Detail zu untersuchen. Die hierzu notwendigen experimentellen Untersuchungen erfolgten am Speicherring ESR der GSI-Darmstadt für das Stoßsytem $U^{92+} \rightarrow N_2$ und für Projektilenergien, die im Bereich zwischen 98 und 400 MeV/u

lagen. Besonders hervorzuheben ist der Einsatz eines segmentierten Germaniumdetektors, der speziell für den Nachweis linear polarisierter Strahlung im Energiebereich oberhalb 100 keV entwickelte wurde. Die lineare Polarisation der Strahlung wurde hierbei durch eine Analyse der Comptonstreuung innerhalb des Detektors gewonnen. Die durch eine präzise Analyse der Comptonstreuverteilungen gewonnenen Daten zeigen eine ausgeprägte lineare Polarisierung der REC-Strahlung in der Streuebene, die zudem eine starke Abhängigkeit als Funktion der Stoßenergie und des Beobachtungwinkels aufweist. Der detaillierte Vergleich mit nicht-relativistischen und relativistischen Vorhersagen ermöglichte darüberhinaus den Nachweis für das Auftreten starker relativistischer Effekte, die sich allerdings depolarisierend auswirken.

Das Experiment wurde am internen Target des ESR-Speicherrings durchgeführt, wobei der Photonennachweis mittels mehrerer Ge(i)-Detektoren erfolgte, die die Ionen-Target-Wechselwirkungszone unter Beobachtungswinkeln zwischen nahe Null und 150 Grad einsahen. Alle Photonendetektoren wurden in Koinizidenz mit einem Teilchendetektor betrieben, um so die volle Charakteristik des REC-Prozesses zu erfassen, also den Einfang eines Targetelektrons in die nackten Uranionen (U^{92+}) unter Emission eines Photons. Für den Polarisationsnachweis entscheidend war der Einsatz eines Germanium-Pixel-Detektors, der abwechselnd unter den Winkeln von 60 und 90 Grad betrieben wurde. Dieser Detektor verfügt über eine 4x4 Pixelmatrix (Pixelgröße:7x7 mm), wobei die elektronische Information jedes Pixels (Energiesignale und schnelle Zeitsignale) separat registriert und aufgezeichnet wurde. Hierdurch war es möglich Ereignisse, die koinzident in zwei Pixeln erfolgten, zu detektieren und zu analysieren. Dies ist die eigentliche Voraussetzung für den Nachweis der linearen Polarisation bei hohen Photonenenergien, bei dem die Abhängigkeit des differenziellen Wirkungsquerschnitts für Comptonstreuung von der linearen Polarisation der einfallenden Photonen ausgenutzt wird (siehe Klein-Nishina Formel Eq. 2.7). Der Nachweis der Comptonstreuung erfolgt hierbei durch die Detektion des Compton-Rückstoßelektrons (ΔE) und des gestreuten Comptonphotons ($\hbar\omega'$), die jeweils separat, aber koinzident in zwei unterschiedlichen Segmenten des Detektors nachgewiesen werden. Hier sei betont, dass für Germanium bereits ab Photonenenergien von ca. 160 keV die Absorption der Strahlung durch den Compton-Effekt über die Pho-

toabsorption dominiert und somit das Ausnutzen des Compton-Effekts prinzipiell eine sehr effektive Technik ist. Der Auswertung der Daten kam wesentlich zugute, dass der Germanium-Detektor über eine im Vergleich zu Szintillations- oder Gaszählern gute Energieauflösung von ca. 1.8 keV bei 122 keV verfügt. Somit kann durch Bilden der Summenenergie $\hbar\omega = \hbar\omega' + \Delta E$ für koinzidente Ereignisse die Energie des einfallenden Photons ($\hbar\omega$) rekonstruieren werden und als zwingende Bedingung dafür herangezogen werden, dass es sich bei dem Ereignis im Detektor um ein Compton-Event gehandelt hat.

Für den Fall linearer Polarisation ist eine wesentliche Aussage der Klein-Nishina-Formel, dass die maximale Intensität für die Compton gestreuten Photonen senkrecht zur Polarisationsebene zu erwarten ist. Tatsächlich zeigen bereits die während des Experiments aufgenommenen Rohdaten für den Fall der untersuchten REC-Strahlung, die durch den Einfang in die K-Schale des Projektils entsteht, dass es sich hierbei um eine stark polarisierte Strahlung handelt, wobei eine erhöhte Intensität für Comptonstreuung senkrecht zur Stoßebene (für den REC-Prozeß definiert durch die Ionenstrahlachse und den Impuls des REC-Photons) festgestellt wurde (vgl. Fig. 7.3).

Zur genauen qualitative Analyse der Meßdaten wurden alle möglichen Pixelkombination der (4x4) Detektorgeometrie ausgewertet, wobei jedoch koinzidente Ereignisse benachbarter Segmente ausgeschlossen wurden, um den hier vorhanden Einfluß elektronischer Übersprecher zu eliminieren. Zudem erfolgte die Analyse der Daten unter Berücksichtigung verschiedenster Effekte, die einen Einfluß auf die Nachweiseffizienzen für die Compton gestreuten Photonen haben könnten. An prominenter Stelle ist hier die Korrektur zu nennen, die durch die Detektordicke von 1,5 cm und der Pixelgröße von 7x7 cm^2 hervorgerufen wird. Zu betonen ist hier, dass für die Auswertung nur relative Effizienzen eine Rolle spielen und so der Einfluß systematischer Fehler, hervorgerufen durch Effizienzkorrekturen, stark reduziert werden konnte (für eine so gewonnene, vollständige Compton-Streuverteilung sei auf Abbildung 9.1 verwiesen, in der die Intensitätsverteilung für Compton-Streuung dargestellt ist). Es sei auch hervorgehoben, dass der Nachweis der Polarisation durch Messungen von vollständigen Compton-Intensitätverteilung im Detektor erfolgte, was das hier diskutierte Experiment wesentlich von konventionellen Polarisationsexperi-

menten für harte Röntgen und γ-Strahlung unterscheidet. Üblichweise wird in diesen Experimenten die Comptonstreuung ausschließlich in der Reaktionsebene und senkrecht dazu nachgewiesen wird. Generell weisen die in der vorliegenden Arbeit gewonnen Compton-Streuverteilungen für den K-REC-Prozeß ein ausgeprägtes Maxium senkrecht zur Reaktionsebene auf und bestätigen somit den bereits aus den Rohdaten abgeleiteten Befund, dass die Polarisationsebene der K-REC Strahlung in der Reaktionsebene des Stosses liegt. In der Tat kann dieser Befund für alle Energien und Beobachtungswinkel bestätigt werden, die in dem hier diskutierten Experiment verwendet wurden. Hier sei zudem darauf hingewiesen, dass es durch die Erfassung der vollständigen Compton-Streuverteilung möglich war, die Orientierung der Polarisationsebene in Bezug auf die Stoßebene mit mit hoher Präzission zu erfassen. So konnte z.B. bei der Stossenergie von 400 MeV/u und dem Winkel von 90 Grad, die Orientierung der Comptonstreuverteilung in Bezug auf die Stoßebene zu ϕ=90$\pm$3 Grad bestimmt werden. Dieser Befund könnte für die Planung zukünftiger Experimente zum Nachweis polarisierter Ionenstrahlen entscheidend sein, da eine Abweichung von der ϕ = 90 Grad Symmetrie nur durch das Vorhandensein polarisierter Teilchen erklärt werden kann. Dieser Effekt, der in neuesten theoretischen Behandlungen im Detail untersucht wurde, stellt gleichsam einen neuen Zugang zur Bestimmung des Polarisationsgrads der Projektile dar. Hierdurch wird die Stärke der hier angewandten Technik verdeutlicht, die auf dem Einsatz eines ortsempfindlichen Geramnium-Pixel-Detektors beruht.

Die Bestimmung des genauen Polarisationsgrades für die K-REC-Strahlung erfolgte durch eine χ^2-Anpassung der Klein-Nishina-Formel an die experimentellen Daten. Die hieraus resultierenden Daten zeigen für alle Strahlenergien und Beobachtungsgwinkel eine starke Polarisation von etwa 80%, wobei die experimentelle Unsicherheit im 10% Bereich liegt. Letztere ist im wesentlichen auf die statistische Genauigkeit zurückzuführen. Die Daten wurden zudem eingehend mit theoretischen Vorhersagen verglichen. Die Theorie stützt sich auf eine vollständige relativistische Beschreibung des REC-Prozesses unter Verwendung exakter Wellenfunktionen für das Kontinuum und den 1s Zustand in wasserstoffartigem Uran. Typischer weise mußten bei den Rechnungen sowohl elektrische wie auch magnetische Multipolterme bis hin zu L=20 verwendet werden, um

Konvergenz zu erreichen. Der Vergleich zeigt eine hervorragende Übereinstimmung zwischen Experiment und Theorie. Zudem verdeutlicht der Vergleich mit der ebenfalls diskutierten Vorhersage der nicht-relativistischen Dipolnäherung die Bedeutung relativistischer Effekte (vor allem das Auftreten höherer elektrischer und magnetischer Multipole), die für die Emission der REC-Strahlung bei hohen, relativistischen Energien und hohem Z charakteristisch sind. Offensichtlich wirken sich diese Effekte stark depolarisierend aus. Dass in der Tat eine Zunahme der depolarisierenden Effekte mit einer Zunahme der Strahlenergie verbunden ist, wird auch durch die Daten dokumentiert, die für den Beobachtungswinkel von 60 Grad als Funktion des Projektilenergie untersucht wurden.

Die in der vorliegenden Arbeit gewonnenen Resultate für die Polarisation der REC-Strahlung ebenso wie die neuartige Experimenttechnik, die hierbei zum Einsatz kam, lassen für die nahe Zukunft eine Serie von weiteren Polarisations-Experimenten erwarten. Hierbei könnte der REC-Strahlung und deren Polarisation als Mittel zur Diagnostik und zum Nachweis des Polarisationsgrades gespeicherter Ionenstrahlen eine Schlüsselrolle zukommen. Als Detektorsysteme werden hierzu zwei-dimensionale Germanium- und Silizium-Streifen-Detektoren zum Einsatz kommen bzw. Kombinationen aus zweidimensionalen Silizium- und Germanium-Detektoren, sogenannte Compton-Teleskope. Diese Compton-Polarimeter, die gegenwärtig für neue Experimentvorhaben am ESR-Speicherring entwickelt werden, verfügen über eine wesentlich verbesserte Ortsauflösung (z.B. 1x1 mm^2) und somit über eine wesentlich gesteigerte Nachweiseffizienz für die Comptonstreuung (ein bis zwei Größenordnungen). Hierdurch sollte es möglich sein, den für Polarisationexerperimente zugänglichen Energiebereich wesentlich auszudehnen, sodass selbst die charakteristische Strahlung der Schwerionen (ca. 50 bis 100 keV) für solche Experimente zugänglich wird.

Bibliography

[1] B. Franzke, *"The heavy ion storage and cooler ring project ESR at GSI"*, NIM B24/25, 1987, 18.

[2] H. Poth, *"Electron cooling: Theory, experiment, application "*, Physics Reports 196, 1990, 135.

[3] F. Bosch. AIP Conference Proceedings 295, 1993, 3.

[4] P. Mokler and T. Stöhlker. Advances in Atomic and Molcular Physics 37, 1996, 297.

[5] M. Steck, P. Beller, K. Beckert, B. Franzke, and F. Nolden, *"Electron cooling experiments at the ESR"*, NIM A 532, 2004, 357-365.

[6] M. Jung, F. Bosch, K. Beckert, H. Eickhoff, H. Folger, B. Franzke, A. Gruber, P. Kienle, O. Klepper, W. Koenig, C. Kozhuharov, R. Mann, R. Moshammer, F. Nolden, U. Schaaf, G. Soff, P. Spadtke, M. Steck, T. Stohlker, and K. Summere, *"First observation of bound-state beta$^-$ decay"*, Phys. Rev. Lett. 69, 1992, 2164–2167.

[7] A. Gumberidze, *"Experimental Studies of the Ground State QED Corrections in H- and He-like Uranium"*, PhD thesis, Frankfurt University, 2003,

[8] A. Gumberidze, T. Stöhlker, D. Banas, K. Beckert, P. Beller, H. F. Beyer, F. Bosch, X. Cai, S. Hagmann, C. Kozhuharov, D. Liesen, F. Nolden, X. Ma, P. H. Mokler, A. Orsic-Muthig, M. Steck, D. Sierpowski, S. Tashenov, A. Warczak, and Y. Zou, *"Electron-Electron Interaction in Strong Electromagnetic Fields: The Two-Electron Contribution*

to the Ground-State Energy in He-like Uranium", Phys. Rev. Lett. 92, 2004, 203004.

[9] P. J. Mohr, G. Plunien, and G. Soff, *"QED corrections in heavy atoms"*, Physics Reports 293, 1998, 227-372.

[10] P. Mokler, T. Stöhlker, C. Kozhuharov, R. Moshammer, P. Rymuza, F. Bosh, and T. Kandler, *"Structure of Very Heavy Few-Electron Ions - New Results from the Heavy Ion Storage Ring, ESR"*, Physica Scripta, T51, 1994, 28-38.

[11] A. Ichihara, T. Shirai, and J. Eichler, *"Radiative electron capture and the photoelectric effect at high energies"*, Phys. Rev. A 54, 1996, 4954–4959.

[12] J. Eichler, A. Ichihara, and T. Shirai, *"Photon angular distributions from radiative electron capture in relativistic atomic collisions"*, Phys. Rev.A 51, 1995, 3027.

[13] T. Stöhlker, C. Kozhuharov, P. H. Mokler, A. Warczak, F. Bosch, H. Geissel, R. Moshammer, C. Scheidenberger, J. Eichler, A. Ichihara, T. Shirai, Z. Stachura, and P. Rymuza, *"Radiative electron capture studied in relativistic heavy-ion - atom collisions"*, Phys. Rev. A 51, 1995, 2098.

[14] J. Eichler, *"Angular distribution of de-excitation X-rays from radiative electron capture in relativistic atomic collisions "*, Nuclear Physics A, 572, 1994, 147-152.

[15] T. Stöhlker, T. Ludziejewski, F. Bosch, R. W. Dunford, C. Kozhuharov, P. H. Mokler, H. F. Beyer, O. Brinzanescu, B. Franzke, J. Eichler, A. Griegal, S. Hagmann, A. Ichihara, A. Krämer, J. Lekki, D. Liesen, F. Nolden, H. Reich, P. Rymuza, Z. Stachura, M. Steck, P. Swiat, and A. Warczak, *"Angular Distribution Studies for the Time-Reversed Photoionization Process in Hydrogenlike Uranium: The Identification of Spin-Flip Transitions"*, Phys. Rev. Lett 82, 1999, 3232.

[16] T. Stöhlker, X. Ma, T. Ludziejewski, H. Beyer, F. Bosch, O. Brinzanescu, R. Dunford, J. Eichler, S. Hagmann, A. Ichihara, C. Kozhuarov, A. Krämer,

D. Liesen, P. Mokler, Z. Stachura, P. Swiat, and A. Warczak. Phys. Rev. Lett. 86, 2001, 983.

[17] T. Stöhlker, F. Bosch, A. Gallus, C. Kozhuharov, G. Menzel, P. H. Mokler, H. T. Prinz, J. Eichler, A. Ichihara, T. Shirai, R. W. Dunford, T. Ludziejewski, P. Rymuza, Z. Stachura, P. Swiat, and A. Warczak, *"Strong Alignment Observed for the Time-Reversed Photoionization Process Studied in Relativistic Collisions with Bare Uranium Ions"*, Phys. Rev. Lett. 79, 1997, 3270–3273.

[18] J. Eichler and A. Ichihara, *"Polarization of photons emitted in radiative electron capture by bare high-Z ions"*, Phys. Rev. A 65, 2002, 052716.

[19] A. Surzhykov, S. Fritzsche, T. Stöhlker, and S. Tachenov, *"Polarization studies on the radiative recombination of highly charged bare ions"*, Phys. Rev. A 68, 2003.

[20] A. Surzhykov, S. Fritzsche, and T. Stöhlker, *"Photon polarization in the radiative recombination of high-Z, hydrogen-like ions"*, Phys. Lett. A 289, 2001, 213.

[21] A. Surzhykov, S. Fritzsche, T. Stöhlker, and S. Tashenov, *"Time-reversed photoeffect in atomic collisions: An efficient tool for the diagnostics of spin polarized ion beams"*, Phys. Rev. Lett., 2004, submitted.

[22] F. Sauter. Ann. Phys. 11, 1931, 454-458.

[23] F. Sauter and H. Wuester. Z. Phys. 141, 1955, 83-86.

[24] T. Stöhlker, D. Banas, A. Gumberidze, C. Kozhuharov, T. Krings, W. Lewoczko, X. Ma, D. Protic, D. Siepowski, S. Tachenov, and A. Warczak, *"Applications of position sensitive germanium detectors for X-ray spectroscopy of highly charged heavy ions"*, NIM B 205, 2003, 210-214.

[25] F. Metzger and M. Deutsch, *"A Study of the Polarization-Direction Correlation of Succesive Gamma-Ray Quanta"*, Phys. Rev. 78, 1950, 551-558.

[26] H. Beyer, T. Stöhlker, D. Banas, D. Liesen, D. Protic, K. Beckert, P. Beller, J. Bojowald, F. Bosch, E. Ffrster, B. Franzke, A. Gumberidze, S. Hagmann, J. Hoszowska, P. Indelicato, O. Klepper, H.-J. Kluge, S. Kfnig, C. Kozhuharov, X. Ma, B. Manil, I. Mohos, A. Orsic-Muthig, F. Nolden, U. Popp, A. Simionovici, D. Sierpowski, U. Spillmann, Z. Stachura, M. Steck, S. Tachenov, M. Trassinelli, A. Warczak, O. Wehrhan, and E. Ziegler, *"FOCAL: X-ray optics for accurate spectroscopy"*, Spectrochimica Acta Part B 59, 2004.

[27] J. Hubbell, *"Photon Mass Attenuation and Energy Absorption Coefficients from 1 keV to 20 MeV"*, Int. J. Appl. RadiatIsotopes, 33, 1982, 1269-1290.

[28] J. Hubbell, W. Veigele, E. Briggs, R. Brown, D. Cromer, and R. Howerton, *"Atomic Form Factors, Incoherent Scattering Functions, and Photon Scattering Cross Sections"*, J. Phys. Chem. Ref. Data 4, 1975, 471-538.

[29] J. Hubbell and Overbo, *"Relativistic Atomic Form Factors and Photon Coherent Scattering Cross Sections"*, J. Phys. Chem. Ref. Data 8, 1979, 69-105.

[30] J. Scofield, *"Theoretical Photoionization Cross Sections from 1 to 1500 keV"*, Lawrence Livermore National Laboratory Rep. UCRL-51326, 1973.

[31] J. Jackson, *"Classical Electrodynamics, 2nd ed."*, Wiley, New York, 1975, 682.

[32] I. Aitchison, *"Relativistic Quantum Mechanics"*, Macmillan, London, 1972, 162.

[33] R. Feynman, *"Theory of Fundamental Processes"*, Benjamin, New York, 1961, 125-130.

[34] M. Scadron, *"Advancen Quantum Theory and its application Trough Feynman Diagrams"*, Springer, New York, 1979, 218.

[35] J. Jauch and F. Rohrlich, *"The Theory of Photons and Electrons"*, Springler, New York, 1976, 234.

[36] L. Kissel, *"RTAB: the Rayleigh scattering database"*, Radiation Physics and Chemistry, 59, 2000, 185-200.

[37] W. Leo, *"Techniques for Nuclear and Particle Physics Experiments"*, Springer-Verlag, 1987, 57.

[38] R. Novick, *"Stellar and Solar X-Ray Polarimetry"*, Space Sci. Rev. vol.18, 1975, 389-408.

[39] P. Kaaret et al, *"Status of the Stellar X-Ray Polarimeter for the Spectrum-X-Gamma Mission"*, SPIE vol.2010, 1993, 221.

[40] P. Kaaret et al, *"The Stellar X-Ray Polarimeter: a focal plane polarimeter for the Spectrum X-Gamma mission"*, Optical Engineering vol.29, 1990, 773-780.

[41] J. Black, P. Deines-Jones, S. Ready, and R. Street, *"X-ray polarimetry with an active-matrix pixel proportional counter"*, NIM A 513, 2003, 639-643.

[42] R. Bellazzini, L. Baldini, A. Brez, E. Costa, L. Latronico, N. Omodei, P. Soffitta, and G. Spandre, *"A photoelectric polarimeter based on Micropattern Gas Detector for X-ray astronomy"*, NIM A 510, 2003, 176-184.

[43] B. Wojtsekhowski, D. Tedeschi, and B. Vlahovic, *"A pair polarimeter for linearly polarized high-energy photons"*, NIM A 515, 2003, 605-613.

[44] A. Ferguson, *"Polarization sensitive detectors"*, NIM 162, 1979, 565-586.

[45] A. Ljubicic and B. Logan, *"A Polarimeter constructed with two Si(Li) detectors"*, NIM 96, 1971, 441-445.

[46] K. Hardy, A. Lumpkin, V. Lee, G. Owen, and R. Shnidman, *"Development of a Compton Polarimeter with Solid State Detectors"*, NIM 42, 1971, 482-484.

[47] P. Butler, P. Carr, L. Gadeken, A. James, P. Nolan, J. Sharpey-Schafer, P. Twin, and D. Viggars, *"Construction and use a three Ge(Li) Compton polarimeter"*, NIM 108, 1973, 497-502.

[48] K. Ashibe, M. Adachi, and H. Taketani, *"A three Ge(Li) Compton polarimeter for nuclear-reaction gamma-rays"*, NIM 130, 1975, 221-225.

[49] P. Smith, L. Ekstroem, F. Kearns, P. Twin, and N. Ward, *"Gamma-ray spectroscopy of ^{61}Zn and a planar germanium polarimeter system"*, J. Phys. G: Nucl. Phys. 8, 1982, 281-293.

[50] A. von der Werth, F. Becker, J. Eberth, S. Freund, U. Hermkens, T. Mylaeus, S. Skoda, H. Thomas, and W. Teichert, *"Two Compton polarimeter constructions for modern standard γ − spectroscopy"*, NIM A 357, 1995, 458-466.

[51] S. Gunji, H. Sakurai, M. Noma, E. Takase, T. Saito, and H. Msawa, *"A New Design of Hard X-Ray Polarimeter"*, IEEE Transaction on Nuclear Science, vol 41 No 4, August 1994, 1309-1312.

[52] H. Tomita, S. Sano, H. Sakurai, M. Noma, S. Gunji, and E. Takase, *"Basic Performance of Utilized Compton Scattering Type Polarimeter"*, IEEE Transaction on Nuclear Science,vol 43 No 3, June 1996, 1527-1532.

[53] C. Broude, O. Hausser, H. Malm, J. Sharpey-Schafer, and T. Alexander, *"A Ge(Li) two crystal Compton spectrometer"*, NIM 69, 1969, 29-34.

[54] S. Ohya, H. Miura, K. Nishimura, and N. Mutsuro, *"A Compton Polarimeter constructed with a large Si(Li) scatterer and two Ge analysers"*, NIM A276, 1989, 223-227.

[55] E. Costa, M. Cinti, M. Feroci, G. Matt, and M. Rapisarda, *"Design of a scattering polarimeter for hard X-ray astronomy"*, NIM A 336, 1995, 161-172.

[56] P. Soffitta, L. Baldini, R. Bellazzini, A. Brez, E. Costa, G. D. Persio, L. Latronico, N. Omodei, L. Pacciani, and G. Spandre, *"Techniques and detectors for polarimetry in X-ray astronomy"*, NIM A 510, 2003, 170-175.

[57] B. Logan, R. Jones, and A. Ljubicic, *"A figure of merit for gamma-ray polarimeters"*, NIM A 108, 1973, 603-604.

[58] B. Logan, R. Jones, and A. Ljubicic, *"A generalized figure of merit for gamma-ray polarimeters"*, NIM A 117, 1974, 273-275.

[59] B. Schlitt, U. Maier, H. Friedrichs, S. Albers, I. Bauske, P. von Brentano, R. Heil, R.-D. Herzberg, U. Kneissl, J. Margraf, H. Pitz, C. Wesselborg, and A. Zikges, *"A sectored Ge-Compton polarimeter for parity assignment in photon scattering experiments"*, NIM A337, 1994, 416-426.

[60] R. Sareen, W. Urban, A. Barnett, and B. Varley, *"High-resolution integrated germanium Compton polarimeter for the $\gamma - ray$ energy range 80 KeV - 1 MeV"*, Rev. Sci. Instrum. 66 (6), June 1995, 3653-3661.

[61] L. Garcia-Raffi, J. Tain, J. Bea, A. Gadea, L. Palafox, J. Rico, and B. Rubio, *"Non-orthogonal gamma-ray Compton polarimeters"*, NIM A 359, 1995, 628-631.

[62] F. Tokanai, H. Sakurai, S. Gunji, S. Motegi, H. Toyokawa, M. Suzuki, K. Hirota, S. Kishimoto, and K. Hayashida, *"Hard X-ray polarization measured with a Compton polarimeter at synchrotron radiation facility"*, NIM A 530, 3, 2004, 446-452.

[63] G. Ewan, G. Andersson, G. Bartholomew, and A. Litherland, *"Gamma-Ray Polarization Measurements with a single Ge(li) detector"*, Physics Letters Vol.29B, No.6, June 1969, 352-354.

[64] B. Logan, *"Detection of the plane of polarization of linearly polarized photons with a rectangular geometry Si(Li) detectors"*, NIM 95, 1971, 301-305.

[65] A. Filevich, M. Behar, and G. G. Bermudez, *"Gamma-gamma polarized directional correlations set-up using a planar Ge(Li) detector as the polarimeter"*, NIM 141, 1977, 521-524.

[66] P. Twin, *"Experimental measurements of the relative peak efficiencies of various Compton polarimeters"*, NIM 103, 1972, 613-616.

[67] R. Bass, S. Brinkmann, C. Charzewski, and H. Hanle, *"Symmetrical Two-Crystal Compton Polarimeter for Gamma Rays"*, NIM 104, 1972, 33-43.

[68] R. Bass, J. Idzko, H. Pelz, K. Stelzer, T. Weber, and R. Weniger, *"Symmetrical Four-Crystal Compton Polarimeter for Gamma Rays: Design and Application"*, NIM 163, 1979, 377-387.

[69] T. Khan, H. Milchberg, N. Singhal, and M. Johns, *"A high resolution $\gamma-ray$ polarimeter for the 100 to 800 KeV energy range"*, NIM 169, 1980, 527-532.

[70] T. Matsuzaki, H. Taketani, M. Ishii, and M. Ohshima, *"A Compton Polarimeter with a pair of high-purity Ge diodes"*, NIM 188, 1981, 63-68.

[71] M. Ishii, M. Ohshima, T. Matsuzaki, and H. Taketani, *"A Compton Polarimeter composed of four planar diodes of high-purity germanium"*, NIM 196, 1982, 117-119.

[72] R. Kroeger, W. Johnson, J. Kurfess, and B. Philips, *"Gamma ray polarimetry using a position sensitive germanium detector"*, NIM A 436, 1999, 165.

[73] C. Hutter, M. Babilon, W. Bayer, D. Galaviz, T. Hartmann, P. Mohr, S. Mueller, W. Rochow, D. Savran, K. Sonnabend, K. Vogt, S. Volz, and A. Zilges, *"Polarization sensitivity of a segmented HPGe detector up to 10 MeV"*, NIM A 489, 2002, 247-256.

[74] T. Aoki, J. Ruan(Gen), A. Yoshimura, and Y. Matsuyama, *"Ge(Li) summing spectrometer of special type"*, NIM 128, 1975, 53-60.

[75] E. Eube, J. Eberth, U. Eberth, H. Eichner, and V. Zobel, *"A "Five-in-one" Ge(Li) spectrometer as Compton polarimeter"*, NIM 130, 1975, 73-77.

[76] J. Simpson, P. Butler, and L. Ekstroem, *"Application of a sectored Ge(Li) detector as a Compton polarimeter"*, NIM 204, 1983, 463-469.

[77] D. Protic, T. Stöhlker, and H. B. et al, *"A Microstrip Germanium Detector for Position-Sensitive X-Ray Spectroscopy"*, IEEE Trans. Nucl. Sci. 48 (4), 2001, 1048.

[78] Z. He, W. Li, G. Knoll, D. Wehe, J. Berry, and C. Stahle, *"3-D position sensitive CdZnTe gamma-ray spectrometers"*, NIM A 422, 1999, 173-178.

[79] K. Vetter, M. Burks, and L. Mihailescu, *"Gamma-ray imaging with position-sensitive HPGe detectors"*, NIM A 525, 2004, 322–327.

[80] R. Kroeger, W. Johnson, R. Kinzer, J. Kurfess, S. Inderhees, B. Philips, and B. Graham, *"Gamma-Ray Instrument for Polarimetry, Spectroscopy and Imaging (GIPSI)"*, SPIE Vol 2806, 1996, 52.

[81] P. Jones, L. Wei, F. Beck, P. Butler, T. Byrski, G. Duchene, G. de France, F. Hannachi, G. Jones, and B. Kharraja, *"Calibration of the new composite "clover" detector as a Compton polarimeter for the EUROGAM array"*, NIM A 362, 1995, 556-560.

[82] Y. Du, Z. He, G. Knoll, D. Wehe, and W. Li, *"Evaluation of a Compton scattering camera using 3-D position sensitive CdZnTe detectors"*, NIM A 457, 2001, 203-211.

[83] C. Yang, *"Possible Experimental Determination of Whether the Neutral Meson is Scalar or Pseudoscalar"*, Phys. Rev. 77, 1950, 722–723.

[84] T. Berlin and L. Madansky, *"On the Detection of gamma-Ray Polarization by Pair Production"*, Phys. Rev. 78, 1950, 623.

[85] G. Wick, *"Detection of Gamma-Ray Polarization by Pair Production"*, Phys. Rev. 81, 1951, 467–468.

[86] H. Olsen and L. Maximon, *"Photon and Electron Polarization in High-Energy Bremsstrahlung and Pair Production with Screening"*, Phys. Rev. 114, 1959, 887–904.

[87] H. Sasaki, K. Takamatsu, S. Iwata, H. Ito, Y. Wakuta, and G. Horikoshi, *"Production of high-energy polarized gamma-rays from an electron synchrotron with amorphous radiator"*, NIM 62, 1968, 45-50.

[88] M. Kobayashi and K. Kondo, *"New method for measurement of γ-ray polarization by detection of angular correlation in pair production"*, NIM 104, 1972, 101-107.

[89] H. Schopper, *"Measurement of circular polarization of γ-rays"*, NIM 3, 1958, 158-176.

[90] H. Tolhoek, *"Electron Polarization, Theory and Experiment"*, Review of Modern Physics, 28 No.3, 1956, 277-298.

[91] E. Lipson and J. Vanderleeden, *"A Monte Carlo calculation of the analyzing efficiency of gamma-ray circular polarimeters"*, NIM 104, 1972, 525-530.

[92] A. Arychev, A. Potylitsyn, and M. Strihanov, *"Determination of circular polarization of γ-quanta with energy $> 10\ MeV$ using Compton polarimeter"*, SPIN01 Conference proceedengs, 2001,

[93] T. Stöhlker, H. Geissel, H. Irnich, T. Kandler, C. Kozhuharov, P. Mokler, G. Muenzenberg, F. Nickel, C. Scheidenberger, T. Suzuki, M. Kucharski, A. Warczak, P. Rymuza, Z. Stachura, A. Kriessbach, D. Dauvergne, R. Dunford, J. Eichler, A. Ichihara, and T. Shirai, *"L-Subshell Resolved Photon Angular Distribution of Radiative Electron Capture into He-like Uranium"*, Phys. Rev. Lett. 73, 1994, 3520.

[94] F. Coester, *"Principle of Detailed Balance"*, Phys. Rev. 84, 1951, 1259.

[95] M. Stobbe. Ann. Phys. (Leipzig) 7, 1930, 661.

[96] H. Bethe and E. Salpeter, *"Quantum Mechanics of One- and Two-Electron Atoms"*, Academic, New York, 1957.

[97] E. Spindler, H.-D. Betz, and F.Bell, *"Influence of Retardation on the Angular Distribution of Radiative Electron Capture"*, Phys. Rev. Lett. 42, 1979, 832.

[98] E. Spindler, *"Ph.D. Thesis"*, Muenchen, 1979.

[99] J. Eichler, A. Ichihara, and T. Shirai, *"Alignment caused by photoionization and in radiative electron capture into excited states of hydrogenic high-Z ions"*, Phys. Rev A 58, 1998, 2128.

[100] J. Eichler. Phys Rep. 193, 1990, 165.

[101] A. Ichihara, T. Shirai, and J. Eichler, *"Radiative electron capture in relativistic atomic collisions"*, Phys. Rev. A 49, 1994, 1875.

[102] U. Fano, K. McVoy, and J. Albers, *"Sauter Theory of the Photoelectric Effect"*, Phys. Rev. 116, 1959, 1147.

[103] R. Pratt, A. Ron, and H. Tseng, *"Atomic Photoelectric Effect Above 10 keV"*, Revs. Mod. Phys. 45, 1973, 273.

[104] V. V. Balashov, A. N. Grum-Grzhimailo, and N. M. Kabachnik, *"Polarization and Correlation Phenomena in Atomic Collisions"*, Kluwer Academic Plenum Publishers, New York, 2000.

[105] K. Blum, *"Density Matrix Theory and Applications"*, Plenum Press, New York, 1981.

[106] J. Eichler and W. Meyerhof, *"Relativistic Atomic Collisions"*, (Academic Press, San Diego, 1995.

[107] A. Surzhykov, P. Koval, and S. Fritzsche, *"Algebraic tools for dealing with the atomic shell model. I. Wavefunctions and integrals for hydrogen–like ions"*, Computer Physics Communications, 2004, accepted for publication.

[108] R. Pratt, R. Levee, R. Pexton, and W. Aron. Phys. Rev. 134, 1964, 916.

[109] U. Fano, K. McVoy, and J. Albers, *"Interference of Orbutal and Spin Currents in Bremsstralung and Photoelectric Effect"*, Phys. Rev. 116, 1959, 1159.

[110] W. H. McMaster and F. L. Hereford, *"Angular Distribution of Photoelectrons Produced by 0.4-0.8-MeV Polarized Photons"*, Phys. Rev. 95 N3, 1954, 723-726.

[111] B. Logan, *"A crossover phenomenon in the photoelectric effect"*, J. Phys. A: Gen. Phys. 4, 1971, 346-351.

[112] A. Belkacem, N. Claytor, T. Dinneen, B. Feinberg, and H. Gould. Phys. Rev. A 58, 1998, 2184.

[113] C. Vane, H. Krause, S. Datz, P. Grafström, H. Knuden, C. Scheidenberger, and R. Schuch, *"Radiative electron capture at ultrarelativistic energies: 33-TeV Pb^{82+} ions"*, Phys. Rev. A 62, 2000, 010701.

[114] W. Meyerhof, R. Anholt, J. Eichler, H. Gould, C. Munger, J. Alonso, P. Thieberger, and H. E. Wegner, *"Atomic collisions with relativistic heavy ions. III. Electron capture"*, Phys. Rev. A 32, 1985, 3291.

[115] J. Eichler, *"Eikonal theory of charge exchange between arbitrary hydrogenic states of target and projectile"*, Phys. Rev. A 23, 1981, 498.

[116] D. Dewangan and J. Eichler. Phys. Rep. 247, 1994, 59.

[117] J. Eichler, *"Relativistic eikonal theory of electron capture"*, Phys. Rev A 32, 1985, 112.

[118] A. Ichihara, T. Shirai, and J. Eichler. Atomic Data and Nuclear Data Tables 55, 1993, 63.

[119] E. Spindler, H.-D. Betz, and F. Bell, *"Influence of Retardation on the Angular Distribution of Radiative Electron Capture"*, Phys, Rev. Lett. 42, 1979, 832.

[120] M. Steck, K. Beckert, H. Eickhoff, B.Franzke, O. Klepper, R. Moshammer, F. Nolden, P. Spädtke, and T. Winkler, *"Proc. 4th Europ. Part. Accel. Conf. London"*, eds. V. Suller and Ch. Petit-Jean-Genaz (World Scientific, Singapore, 1994), 1994, 1197.

[121] K. Blasche and B. Franzke, *"Status report on SIS-ESR, Proc. 6^{th} Europ. Part. Acc. Conf. (EPAC), London"*, World Scientific, Singapore, 1994, 133.

[122] F. Bosch and B. Schlitt. Phys. Bl. 53, 1997, 27.

[123] B.Franzke, *"Information about ESR Paramteres"*, GSI-ESR/TN-86-01 (Internal Report), 1986,

[124] M. Steck. private communication.

[125] U. Schaaf, *"Schottky-Diagnose und BTF-Messungen an gekuühlten Strahlen im Schwerionen-Speicherring ESR"*, Dissertation Universität Frankfurt, GSI 91-22, Darmstadt, 1991,

[126] O. Klepper and C. Kozhuharov. Nucl. Instr. in Physics Research B, 2003, in print.

[127] H. Reich, W. Bourgeois, B. Franzke, A. Kritzer, and V. Varentsov. Nuclear Physics A 626, 1997, 473c.

[128] A. Krämer, *"PHD Thesis Universität Frankfurt"*, 2000.

[129] T. Stöhlker, O. Brinzanescu, A. Krämer, T. Ludziejewski, X. Ma, and A. Warczak, *"X-Ray and Inner Shell Processes; 18th International Conference"*, AIP Conference Proc. 506, (Chicago, Illinois, 1999), 2000, 389.

[130] T. Stöhlker, T.Ludziejewski, H. Reich, F. Bosch, R. Dunford, J. Eichler, B. Franzke, C. Kozhuharov, G. Menzel, P. Mokler, F. Nolden, P. Rymuza, Z. Stachura, M. Steck, P. Swiat, and A. Warczak, *"Charge-exchange cross sections and beam lifetimes for stored and decelerated bare uranium ions"*, Phys. Rev. A 58, 1998, 2043.

[131] E. Clementi and C. Roetti. At. Data Nucl. Data Tables 14, 1974, 177.

[132] M. Kleber and D. Jakubassa. Nucl. Phys. A 252, 1975, 152.

[133] F. Biggs, L. Mendelsohn, and J. Mann. Atomic Data and Nuclear Data Tables 16, 1975, 201.

[134] P. Eisenberger and P. Platzman, *"Compton Scattering of X Rays from Bound Electrons"*, Phys. Rev. A 2, No2, 1970, 415-423.

[135] R. Ribberfors and K.-F. Berggen, *"Incoherent-x-rayscattering functions and cross sections $(d\sigma/d\Omega')_{incoh}$ by means of a pocket calculator"*, Phys. Rev. A 26, No6, 1982, 3325-3333.

[136] R. Ribberfors, *"Relationship of the relativistic Compton cross section to the momentum distribution of bound electron states"*, Phys. Rev. B 12, No6, 1975, 2067-2074.

[137] R. Ribberfors, *"Relationship of the relativistic Compton cross section to the momentum distribution of bound electron states. II. Effects of anisotropy and polarization"*, Phys. Rev. B 12, No8, 1975, 3136-3141.

[138] V. Schönfelder, A. Hirner, and K. Schneider, *"A telescope for soft gamma ray astronomy"*, NIM 107, 1973, 385-394.

[139] J. LeBlanc, N. Clinthorne, C.-H. Hua, E.Nygard, W. Rogers, D. Wehe, P. Weilhammer, and S. Wilderman, *"C-SPRINT: A Prototype Compton Camera System For Low Energy Gamma Ray Imaging"*, IEEE trans. nucl. science. Vol.45, No3, 1998, 943-949.

[140] Ken-ichi Hino and T. Watanabe, *"Theory of the radiative electron capture incorporating of the internal conversion process"*, Phys. Rev. A 39 N 7, 1989, 3373-3387.

[141] J. H. Macek and R. Shakeshaft, *"Second Born approximation with the Coulomb Green's function: Electron capture from a hydrogenlike ion by a bare ion"*, Phys. Rev. A 22, 1980, 1441–1446.

[142] Ken-ichi Hino and T. Watanabe, *"Angular-distribution and linear-polarization correlation of photons induced by the relativistic radiative electron-capture process"*, Phys. Rev. A 36 N 12, 1987, 5862-5865.

[143] L. Labzowsky, A. Nefiodov, G. Plunien, G. Soff, R. Marrus, and D. Liesen, *"Parity-violation effect in heliumlike gadolinium and europium"*, Phys. Rev. A 63, 2001, 054105.

[144] A. Klasnikov, A. Artemyev, T. Beier, J. Eichler, V. Shabaev, and V. Yerokhin, *"Spin-flip process in radiative recombibation of an electron with H- and Li-like uranium"*, Phys. Rev. A 66, 2002, 042711.

[145] A. Prozorov, L. Labzowsky, D. Liesen, and F. Bosh, *"Schemes for radiative polarization of ion beams in storage rings"*, Phys. Lett. B 574, 2003, 180-185.

[146] T. Stöhlker, H. Backe, H. Beyer, F. Bosch, A. Brauning-Demian, S. Hagmann, D. Ionescu, K. Jungmann, H.-J. Kluge, C. Kozhuharov, T. Kuhl,

D. Liesen, R. Mann, P. Mokler, and W. Quint, *"Status and perspectives of atomic physics research at GSI: The new GSI accelerator project"*, NIM B 205, 2003, 156-161.

Thanks

The only person to whom I can dedicate this work is my mother Margarita Ivanovna Blagoveschenskaya. The fact that I became a scientist is in an important aspect her merit. Thanks for believing in me.

My very special thanks I would like to express to my supervisor Prof. Dr. Thomas Stöhlker who introduced me into the field of experimental atomic physics and guided my work during my PhD years. His very broad experience, help and suggestions were highly important for me and absolutely crucial in currying out this work.

I would like to thank Prof. Dr. Heinz-Jürgen Kluge and to Prof. Dr. Horst Schmidt-Böcking who kindly accepted me in the Atomic Physics group of GSI and as a PhD student in Frankfurt University and gave me a unique opportunity to do this work and to collect a lot experience while staying in such an international research center like GSI.

I would like to acknowledge the debt I owe to my colleagues at GSI Atomic Physics department: Dr. D. Banaś, Dr. T. Beier, Prof. H.F. Beyer. Prof. F. Bosch, Dr. C. Brandau, Dr. A. Baüning-Demian, Dr. A. Gumberidze who closely followed my work and continuously helped me; Prof. S. Hagmann whose unflagging optimism always inspirits me; Prof. C. Kozhuharov whose long discussions about a broad variety of subjects improved my knowledge of physics, history, languages and many other human related fields; Prof. D. Liesen, Dr. X. Ma, Prof. P.H. Mokler, A. Oršić-Muthig, R. Reuschl, J. Rzadkiewicz, U. Spillman, S. Trotsenko; colleagues from Kassel University: Dr. habil. S. Frietzsche and Dr. A. Surzhykov whose usual prompt response, help and discussions were very important for me; and the collaborators from Poland: D. Sierpowski, Prof. M. Pajek, Dr. Z. Stachura and Prof. A. Warczak. I have learned so much from working with you. Thank you for your collaboration, helpful comments and suggestions, constructive criticism and interest in my work.

I appreciate deeply Prof. Anatoly Andreev for being my teacher and a first physics supervisor.

For truly happy time spent together during these years I am very grateful to Kasia and Zbyszek Tyminscy, Gosia Sudoł and Alex Gumberidze. Together with you I really discovered a new definition of friendship. Thank you for being my friends.

I direct my special thanks to Katia and Andrey Surzhykov with whom besides being close collaborators we became also close friends and whose hospitality always fascinates me.

My dear friends: Gonzalo Rodriguez, Dominik Sierpowski, Georgios Tsiledakis, Kasia Psonka and Darek Antonczyk, Alberto Cribeiro and Paola, Alejandro Castillo, you are very important part of my life which I can not imagine apart of yours. Anton Andronic, Chilo Garabatos, Milan Matos, Mateusz Ploskon, Rady, Gabor, Hayk, Sergey, Jurek, Markus, Przemek, Tomek, Kelly, Natalia, Diego, Isaac and Estela Jimenez, I will never forget all of you, folks. I am happy that life gave me a chance to meet you.

Mikhail Boldasov and Maria Rudakova, Evgeny Kravcunov and Alexey Verschagin, Katia Afanasova and Nadia Chamina, Aleksey Saveliev, Andrey Gavrikov, Roman Rogov and Viktor Dergach, you always were my friends and you will always be, thank you for this and sorry for escaping from you for a so long time, although this time was very important for me.

I would also like to thank all those teachers in Vologda and Moscow who have shared their classrooms and ideas with me over the years, especially Aleksander Cherednik, David Kandelaki, Mikhail Kanin, Vladimir Suhomlin and Andrey Gerasimov.

My PhD years coincided perfectly with my conservatory study and I would like to express my sincere gratitude to my classical guitar teacher Prof. Michael Teuchert who guided my steps in wonderful world of music.

And last but not least my grateful thanks to my parents and my family: Lev, Olga, Katia, Sasha, Mitya, Yulia.

I truly wish to continue but also fear to extend this list over too many pages. And I apologies if I have accidentally omitted somebody to whom acknowledgement is due.

Sincerely yours,
Stanislav Tashenov